Applications of Graphene in Vanadium Redox Flow Batteries

by

Elizabeth Esther Miller

A thesis

presented to the University of Waterloo

in fulfillment of the

thesis requirement for the degree of

Master of Applied Science

in

Chemical Engineering

Waterloo, Ontario, Canada, 2023

Author's Declaration

This thesis consists of material all of which I authored or co-authored: see Statement of Contributions included in the thesis. This is a true copy of the thesis, including any required final revisions, as accepted by my examiners.

I understand that my thesis may be made electronically available to the public.

Statement of Contributions

This thesis contains material adapted from co-authored work [1], the entirety of which may be found in the Appendix. This research was accomplished as part of a collaboration with the Ted Roberts group at the University of Calgary, facilitated by the Alberta Innovates program. The graphene used was synthesized by researchers at the University of Calgary (Maedeh Pahlevaninezhad, Ashutosh Singh, and Lixin Xi), shipped to the University of Waterloo for dispersion and deposition onto the membranes by the author of this report in addition to the co-op student Lauren Sarah Prophet. Coated membranes were returned to the researchers in Calgary for testing in a flow cell while additional imaging of deposited coatings onto a variety of substrates was done via atomic force microscopy (AFM) at the University of Waterloo, primarily conducted by Lauren Sarah Prophet and analysed in Chapter 2 by the author of this report. The group met frequently to discuss and analyze the electrochemical results which resulted in iteratively coating/testing a variety of membrane coating variations. All of the electrochemical testing and data analysis in Chapter 3 has been conducted by the author of this report while some of the monolayer coatings (namely those for GO and some graphene tests) were produced by co-op students Lauren Sarah Prophet and Mira Mackintosh.

Abstract

Vanadium redox flow batteries (VRFBs) exhibit great promise as easily scalable, long-lasting, modular systems for grid-scale energy storage. However, vanadium crossover and poor reaction kinetics increase their operating costs by requiring frequent system regeneration and reducing energy efficiency, respectively. In this thesis, Nafion membranes were modified with single to few-layer nitrogen/sulfur-doped graphene (NS-graphene) by developing a large area Langmuir film deposition method with the aim of reducing vanadium crossover and potentially improving reaction kinetics. Using this approach, the ability to reduce vanadium permeability through Nafion 117 and Nafion 115 membranes by 75% and 53%, respectively, was demonstrated while maintaining a high enough proton conductivity that the overall selectivity of the membranes was increased by 243% and 65% when compared to the results for bare Nafion. To determine the impact of the intrinsic electrocatalytic activity of graphene on redox flow battery performance, a comparison of NS-graphene, graphene oxide (GO), and reduced graphene oxide (RGO) was carried out using both monolayer electrodes and drop-cast films. Through this work, it was confirmed that the previously established approach developed by Punckt et al. [2] to account for porosity could not be extended to quasi-reversible systems such as that of the VRFB. An alternative data analysis scheme based on Dunn's Method is proposed, showing mildly promising results, with more work needed in the area to develop strong conclusions.

Acknowledgements

I would first like to thank my supervisor, Dr. Pope, for all of his patience and insight throughout this whole process. I am also very grateful to have had such a fun and helpful group of labmates over the last two years. I am especially grateful to those who answered my many questions or helped me conduct imaging or related tasks, including Lauren Prophet, Mira Mackintosh, Thomas Storwick, Dr. Gillian Hawes, and Dr. Luzhu Xu, among others. Thank you also to all of our collaborators in Dr. Ted Roberts' group at the University of Calgary, as well as the Natural Sciences and Engineering Research Council (NSERC) and Alberta Innovates for providing the funding for this research.

Dedication

Dedicated to my high school chemistry teacher, Mrs. Rubinder Sadyora, whose compassion at a difficult time for me was one of the key reasons that I have been able to follow the path that led to where I am.

Table of Contents

Author's Declaration ii
Statement of Contributions iii
Abstract iv
Acknowledgements v
Dedication vi
List of Figures ix
List of Tables xi
Nomenclature xii
Introduction 1
1.1 Background 3
1.1.1 Flow Batteries 3
1.1.2 Determining Material Effects on Cell Performance 9
1.1.3 Monolayer Deposition 16
1.2 Literature Review 18
1.2.1 Composite Membranes 18
1.2.2 Graphene and Graphene Nanocomposites 20
1.3 Overview 22
Chapter 2 Graphene Monolayers to Reduce Vanadium Crossover 23
2.1 Methodology 23
2.1.1 Materials 23
2.1.2 Nanomaterial Preparation 24
2.1.3 Coating Procedure 24
2.1.4 Membrane Characterization 31
2.1.5 VRFB Charge−Discharge 35
2.2 Results 37
2.3 Conclusions and Future Work 44
Chapter 3 Catalytic Behaviour of Nanomaterials within the Vanadium System 46
3.1 Methodology 46

3.1.1 Materials....46
3.1.2 Nanomaterial Preparation....46
3.1.3 Electrode Preparation....47
3.1.4 Electrolyte Preparation....48
3.1.5 Electrochemical Testing....49
3.2 Results....50
3.2.1 Monolayer Deposition....50
3.2.2 Porosity Analysis....53
3.3 Conclusions and Future Work....70
References....72
Appendix....80

List of Figures

Figure 1. Diagram of a classical redox flow battery (RFB). [4] 5
Figure 2. Illustrations of two notable features of redox flow batteries 5
Figure 3. Schematic diagram of a VRFB. 7
Figure 4. Typical CV curve for a Nernstian reaction with fast kinetics.. 10
Figure 5. Theoretical CVs for a non-diffusion system at scan rates of (a) 0.01 V/s and (b) 0.01-0.1 V/s. [10] 11
Figure 6. E_{pp} as a function of a porosity factor, P, for monolayer (ML) and drop-cast samples in a ferricyanide system. [1] 15
Figure 7. Schematic illustration of the LB (left) and LS (right) methods of Langmuir film deposition. [14] 18
Figure 8. Example setup to secure a Nafion membrane to a glass substrate prior to modified-LB deposition 26
Figure 9. Examples of membranes which had been coated while secured to the glass substrate using only paperclips (left) or magnets and washers which were in direct contact with the membrane (right). 27
Figure 10. Typical setup for modified-LB deposition prior to the addition of water into the LB trough. 28
Figure 11. Schematic illustration of the deposition process from the top (a−f) and side (g, h). 30
Figure 12. (Left) G-DMF ink for deposition prepared at an initial concentration of 0.42 mg/mL. (Right) Nafion membrane (approximately 7.5 cm x 8 cm) coated with a single monolayer of graphene 31
Figure 13. Schematic illustration of the VRFB setup used for flow cell tests. 36
Figure 14. AFM images of (a) top surface of uncoated Nafion 117, (b) top surface of graphene-coated Nafion 117, and (c) top surface of graphene-coated mica. 38
Figure 15. Secondary electron SEM images (a and b) of the top surface of graphene-coated Nafion 117 a) before cycling and b) after cycling; AFM images (c and d) of the top surface of graphene-coated Nafion 117 c) before cycling and d) after cycling. 39
Figure 16. Comparison of the properties of Nafion and graphene-coated Nafion membranes: (a) water uptake and swelling ratio; (b) area resistance and proton conductivity; (c) VO^{2+} permeability and selectivity; and (d) IEC. 41
Figure 17. Static water contact angle on a) Nafion 117 and b) graphene-coated Nafion 117. 42
Figure 18. Comparison of VRFB performance using bare and graphene-coated Nafion 115 and 117 membranes: (a) self-discharge curves at 50% SOC and charge−discharge efficiencies at a range of current densities, including (b) CE, (c) VE, and (d) EE. 43
Figure 19. AFM images of (a) NS-graphene on mica and (b) GO on silicon. 51
Figure 20. Secondary electron SEM images of modified-LB-deposited (a,b) NS-Graphene, (c,d) GO, and (e,f) RGO on silicon wafer substrates. 52
Figure 21. CV results at 200 mV/s for GC0 coated with RGO in a ferricyanide system. 54

Figure 22. Peak current as a function of the root scan rate for RGO-coated GC0 in a ferricyanide system.....56
Figure 23. CV results at 20 mV/s for RGO coated on (a) GC0 and (b) GC2 in a vanadium system.....57
Figure 24. CV results for polished GC0 in a vanadium system. 58
Figure 25. Graphs showing the peak-to-peak separation observed at a scan rate of 10 mV/s as a function of the porosity factor, P, defined by Punckt et.al.....59
Figure 26. CV results for faster scan rates with modified conditions in sulfuric acid.. 61
Figure 27. Diffusion length as a function of scan rate for (a) ferricyanide and (b) vanadium systems. 62
Figure 28. CV results at 20 mV/s for monolayer tests on (a) GC0 and (b) GC2. 64
Figure 29. Graphs showing the peak-to-peak separation observed at 10 mV/s as a function of a modified form of the porosity factor, P, originally defined by Punckt et al. and now calculated based on principals described in Dunn's Method......67
Figure 30. Graph of peak-to-peak separation as a function of the constant k_2 at different scan rates for the graphene-vanadium system.....68
Figure 31. Graphs showing the peak-to-peak separation at 10 mV/s as a function of the newly-defined surface area factor, S_D.. 70

List of Tables

Table 1. Summary of peak-to-peak separation at each scan rate for various RGO samples in the ferricyanide system using GC0 as a substrate. The colours in each column illustrate the relative peak separations, with red indicating the largest separation at a given scan rate and green indicating the smallest separation at a given scan rate. 55
Table 2. Diffusion length as a function of scan rate for ferricyanide and vanadium systems. 63
Table 3. Summary of peak-to-peak separation at each scan rate for the different monolayer samples using GC0 as a substrate. The colours in each column illustrate the relative peak separations, with red indicating the largest separation at a given scan rate and green indicating the smallest separation at a given scan rate.....64
Table 4. Summary of peak-to-peak separation at each scan rate for the different monolayer samples using GC2 as a substrate. The colours in each column illustrate the relative peak separations, with red indicating the largest separation at a given scan rate and green indicating the smallest separation at a given scan rate.....65

Nomenclature

Abbreviation	Meaning
%	Percent
$(NH_4)_2SO_4$	Ammonium Sulfate
°	Degrees
°C	Degrees Celsius
A	Electrode Surface Area or Cross-Sectional Area of the Membrane
AFM	Atomic Force Microscopy
Ag/AgCl	Silver/Silver Chloride
at%	Atomic Percent
C	Electrolyte Concentration
C_A	VO^{2+} Concentration in Source Reservoir
C_B	VO^{2+} Concentration in Receiving Reservoir
CE	Coulombic Efficiency
$CH_3(CH_2)_3OH$	Butanol
cm	Centimetres
CNF	Carbon Nanofibres
CNT	Carbon Nanotubes
CV	Cyclic Voltammetry
CVD	Chemical Vapour Deposition
D	Electrolyte Diffusion Coefficient
D_p	Diffusion Coefficient
DCE	1,2-Dichloroethane
DI	Deionized
diff.(ν)	Diffusion-Limited Contribution at Scan Rate ν
DMF	N,N-Dimethylformamide
E^0	Standard Potential
EDX	Energy-Dispersive X-ray Spectroscopy
EE	Energy Efficiency
EEG	Electrochemically Exfoliated Graphene
EIS	Electrochemical Impedance Scpectroscopy
EMF	Electromotive Force
E_{pp}	Peak-to-Peak Separation

F	Faraday's Constant
g	Grams
GC	Glassy Carbon
G-DMF	Graphene-DMF Dispersion
GN115	Graphene-Coated Nafion 115
GN117	Graphene-Coated Nafion 117
GO	Graphene Oxide
h	Hours
H^+	Proton
H_2SO_4	Sulfuric Acid
Hz	Hertz
ICP-OES	Inductively Coupled Plasma Optical Emission Spectroscopy
IEC	Ion Exchange Capacity
I_{forw}	Peak Current for Forward Reaction
i_p	Peak Current
k_1	Capacitive Contribution Constant
k_2	Diffusion-Controlled Contribution Constant
keV	Kilo-Electron Volts
kHz	KiloHertz
KOH	Potassium Hydroxide
L	Membrane Thickness
l	Diffusion Length
LB	Langmuir-Blodgett
LS	Langmuir-Schaefer
M	Molar
mA	Milliamperes
mg	Milligrams
$MgSO_4$	Magnesium Sulfate
MHz	Megahertz
min	Minutes
mL	Millilitres
mm	Millimetres
mN	MilliNewton
mV	Millivolts
MΩ	Megaohms

n	Number of Electrons Transferred
NaCl	Sodium Chloride
NaOH	Sodium Hydroxide
nm	Nanometres
NP-graphene	Nitrogen/Phosphorus-Doped Graphene
NS-2N-A	Specific NS-Graphene Sample Label
NS-3N-A	Specific NS-Graphene Sample Label
NS-Graphene	Nitrogen/Sulfur-Doped Graphene
P	Porosity Factor or Permeability
PEM	Polymer Electrolyte Membrane
PTFE	Poly(tetrafluoroethylene)
Q_c	Charge Capacity
Q_d	Discharge Capacity
R	Ideal Gas Constant or Membrane Resistance
r_1	Cell Resistance in Presence of the Membrane
r_2	Cell Resistance in Absence of the Membrane
RFB	Redox Flow Battery
RGO	Reduced Graphene Oxide
RPM	Revolutions Per Minute
S	Effective Membrane Area
s	Seconds
S_D	Surface Area Factor Defined Based on Dunn's Method Principles
SEM	Scanning Electron Microscopy
SiO_2	Silicon Oxide
SOC	State of Charge
T	Temperature
t	Experiment Duration
TEM	Transmission Electron Microscopy
TiO_2	Titanium Dioxide
V	Volts
V_B	Volume of $MgSO_4$
$V_{c,avg}$	Average Cell Voltage During Charging
$V_{d,avg}$	Average Cell Voltage During Discharging
VE	Voltage Efficiency

vol.%	Volume Percent
$VOSO_4$	Vanadium Oxysulfate
$VOSO_4 \cdot xH_2O$	Vanadium(IV) Sulfate Oxide Hydrate
VRFB	Vanadium Redox Flow Battery
XPS	X-ray Photoelectron Spectroscopy
α	Constant used in determining P, seen in Equation 6 and Equation 7
µL	Microlitres
µm	Micrometres
ν	Scan Rate
ν_{max}	Maximum Scan Rate
ν_{min}	Minimum Scan Rate
σ	Proton Conductivity
τ	Transition Time
Ω	Ohms

Introduction

In any risk assessment, the two main aspects to consider are the level of the danger itself and the probability of it coming to pass. In the case of climate change, these factors may be described as disastrous and imminent, respectively. Thus, as it is the duty of engineers to uphold public safety above all else, the mitigation of climate change has long been one of the most researched areas in the field, with each discipline providing a unique insight and approach to solving this problem. Among the industries most relevant to the issue is that of renewable energy since fossil fuels accounted for over 137,000 terawatt-hours of energy consumption across the globe as recently as 2022 [3]. The significant reduction of this dependence is one of the keys to mitigating the effects of climate change before an event horizon is reached [4].

While the source of the renewable energy is of course one of the most important factors to be considered in this research, there are several other decisions to be made beyond the energy sources themselves. One of these is the energy storage technology which is to be used alongside the energy production schemes. Energy storage is highly important to this area for several reasons, including the fact that some of the most widely known renewable energy sources, wind and solar, are subject to constantly fluctuating performance based on peak hours and seasons. As such, it is crucial that energy storage infrastructure be available to store the excess energy produced during these peak times so that it may be used during the periods of lower energy production.

This field has seen outstanding developments over the past few decades, with the commercialization of lithium-ion batteries and the new innovations in fuel cell technology, but further progress is required. Every type of energy storage technology that exists possesses a set of advantages and disadvantages which tailor them to different applications. Whether it is scalability, charge-discharge speed, energy density or any number of other parameters, no single energy storage mechanism sits securely in the top spot since advances are always being made. Since exploring every currently known energy storage mechanism would require a scope tantamount to declaring that a universal solvent can be found through the process of elimination, this report instead focuses entirely on the case of the vanadium redox flow battery (VRFB).

The VRFB is a liquid-based electrochemical storage system in which two electrolytes (the anolyte and catholyte; one for each half-cell to undergo paired reduction and oxidation reactions) are cycled from reservoirs to a contact point in the centre stack of the battery, where they are effectively separated only by an ion-exchange membrane. A closer look at this system and its unique configuration will be discussed in later parts of this report, but it should be noted here that existing literature has already demonstrated marked improvement in VRFB performance through the modification of the ion-exchange membrane. Based on this, the modification of this membrane is the focus of the **first objective** of this research report, which aims to address the known issue of vanadium crossover between half-cells through the application of a graphene monolayer to the ion-exchange membrane. This work brought further questions regarding the influence of the graphene on other aspects of the cell

performance, leading to the **second objective** of this report, which is to determine the potential intrinsic catalytic effects of various graphene nanocomposites including nitrogen/sulfur-doped graphene (NS-graphene), graphene oxide (GO), and reduced graphene oxide (RGO).

1.1 Background

1.1.1 Flow Batteries

While redox flow batteries exist in several different forms, the simplest definition for these systems is as follows: batteries in which the redox couples are contained within liquid electrolytes which are continuously circulated throughout the system by pumps. A more detailed breakdown can be seen in Figure 1, which also illustrates the central stack of the battery, consisting of conducting electrodes as well as an ion-exchange membrane. As with any energy storage system, this configuration comes with several unique advantages and disadvantages which make it of particular interest for industrial and other large-scale energy storage operations. One of the most notable advantages provided by redox flow batteries is that of theoretically infinite scalability as illustrated in Figure 2. Since the system operates based on liquid electrolytes which are cycled with pumps, this means that the capacity of a redox flow battery can be increased simply by increasing the volume of the electrolyte reservoirs in use. Additionally, this setup allows for vastly improved cyclability when compared to other common energy storage alternatives. The reason for this again lies in the fact that the redox species are contained within liquids and will therefore not undergo the

same physical transformations (such as repeated size fluctuation) which often lead to material breakdown and reduced lifespan of other types of batteries. It is worth noting that this does not necessarily apply to all known flow battery configurations, as there exist some hybrid varieties which make use of at least one insoluble component within the system. In this case, the potential for physical degradation of the solid component would still exist. Regardless, these hybrid flow batteries still share one of the other notable advantages of flow batteries which is their modular nature. This is due to the reservoir-stack-reservoir configuration which provides a great deal of flexibility for the actual arrangement of the battery so long as the electrolytes may still be pumped to the central stack. This could be of particular use in settings wherein the floorplan cannot be significantly modified, and a large battery unit would not necessarily be an efficient use of space without some adjustments. Additionally, this configuration allows for the independent design of the reservoir and stack components such that the energy and power capacity are decoupled. [5]

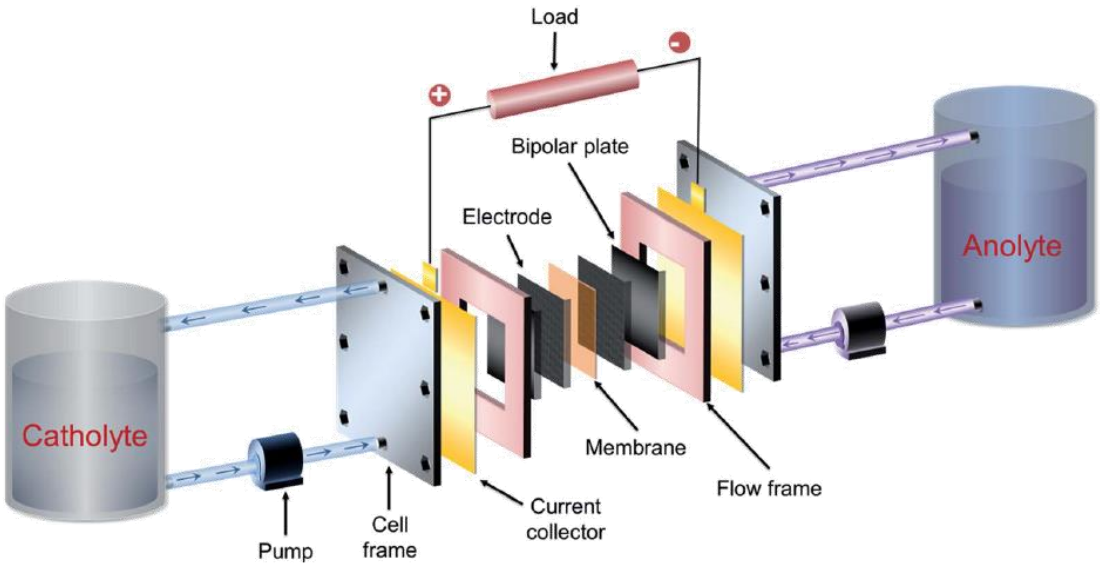

Figure 1. Diagram of a classical redox flow battery (RFB). Reproduced with permission from [5].

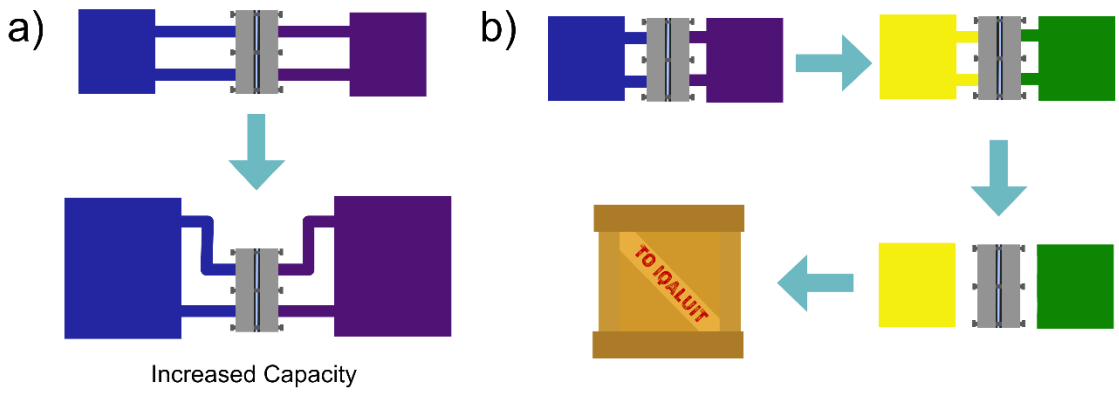

Figure 2. Illustrations of two notable features of redox flow batteries. a) Simple scalability through changing reservoir volume. b) Easy disconnection and transportation of charged electrolytes.

Of course, despite their numerous advantages, redox flow batteries remain plagued by their own unique disadvantages. The most notable of these disadvantages is ion crossover. This occurs when one of the active species within the electrolytes migrates across the ion-exchange membrane to the other side of the cell. This simple movement can result in a number of problems for these batteries, including reduced efficiency/self-discharge, system imbalance, and electrolyte contamination. The latter is arguably the most serious of the consequences, as electrolyte contamination within a cell that has two highly distinct half-cells (such as in iron-chromium flow batteries) could become especially disadvantageous [6]. It is for this reason that the system of primary interest in this report, VRFBs, is being explored. The general design of a VRFB can be seen in Figure 3, with the following half-cell reactions:

$$VO^{2+} + H_2O \leftrightarrow VO_2^{+} + 2H^{+} + e^{-} \qquad E^0 = 1.0 \text{ V vs SHE}$$

$$V^{3+} + e^{-} \leftrightarrow V^{2+} \qquad E^0 = -0.26 \text{ V vs SHE}$$

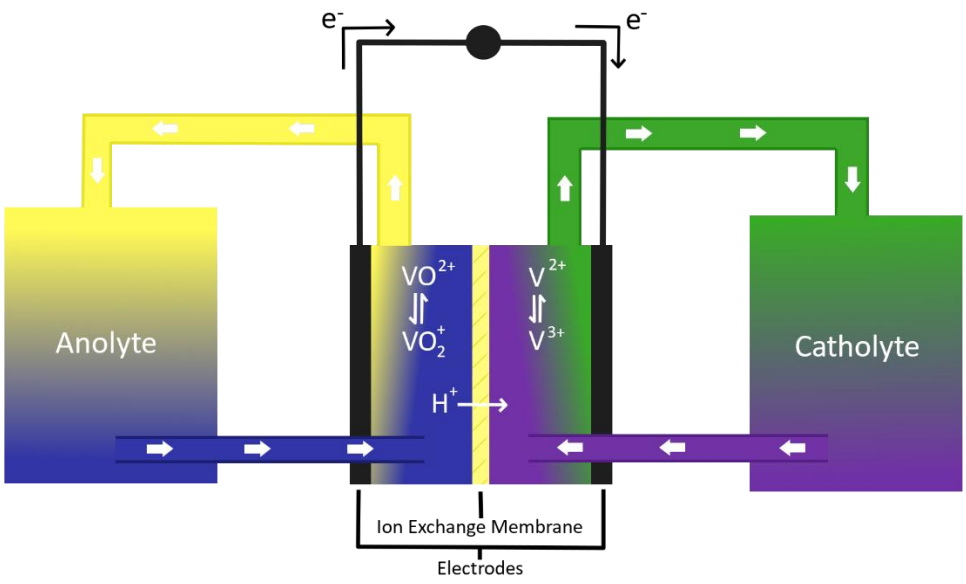

Figure 3. Schematic diagram of a VRFB.

The mechanism of each half-cell reaction has not been definitively established, although many have been proposed (most based on the importance of oxygen-containing functional groups on the electrode surface), and this lack of clarity brings into question which side of the cell is of greater interest for researchers. In practice, most research has focused on the VO^{2+}/VO_2^{+} side, with some interest in the V^{2+}/V^{3+} side specifically aiming to limit H_2 evolution to prevent charge imbalance. [5] The corresponding cell electromotive force (EMF) for the overall VRFB system under standard conditions is 1.26 V, calculated according to Equation 1. However, a notable difference exists between this value and the actual measured open-circuit potential of a VRFB. While some of the problems which arise from ion crossover in RFBs are mitigated by the fact that the active redox species in VRFBs are

limited solely to different oxidation states of vanadium (V^{2+}, V^{3+}, V^{4+}, and V^{5+}) and any cations which manage to cross from one half-cell to the other will not cause contamination of the whole system but will instead simply react to form one of the other vanadium species, this does not completely eliminate the issue. VRFBs still suffer from a loss of efficiency due to self-discharge as well as electrolyte imbalances when a significant amount of crossover occurs in addition to various overpotentials including IR drop within the electrolyte and kinetic overpotential.

Clear performance metrics which reflect the influence of the various resistances and potential losses include the voltage efficiency (VE), coulombic efficiency (CE), and energy efficiency (EE), which may be determined using Equations 2-4: [7] [8]

$$E_{cell}^{0} = E_{cat}^{0} - E_{an}^{0} \quad (1)$$

$$CE = \frac{Q_d}{Q_c} \times 100\ \% \quad (2)$$

$$VE = \frac{V_{d,avg}}{V_{c,avg}} \times 100\% \quad (3)$$

$$EE = CE\ \times VE \quad (4)$$

where Q_c and Q_d are the charge and discharge capacities (in mAh), respectively, and $V_{c,avg}$ and $V_{d,avg}$ are the average cell voltage during charge and discharge, respectively. Individual overpotentials of interest may be calculated directly for a system; however, this often requires extensive testing and iterative calculation. This is the case for kinetic overpotential, which can be calculated with data obtained either through Tafel plots or the iterative solving

of the Butler-Volmer equation [9]. For this reason, simpler methods of evaluating relative kinetic performance between similar cells are explored in this research project.

A great deal of research has already been conducted to mitigate the efficiency losses and address the problem of ion crossover within VRFBs. The main focal point for this research lies with the ion-exchange membrane. One of the most common materials in use for VRFBs is a commercial polymer called Nafion, which is a highly effective cation exchange membrane as a result of its hydrophilic sulfonic acid groups which exist within a hydrophobic fluorocarbon matrix [10]. Nafion is useful as a membrane for these cells due to its high ionic conductivity and relatively high mechanical and chemical stability. However, since it is a cation exchange membrane initially intended for use in polymer electrolyte membrane (PEM) fuel cell applications, it is prone to undesirable crossover of the positively charged vanadium ions.

1.1.2 Determining Material Effects on Cell Performance

Cyclic voltammetry (CV) is one of many commonly used electrochemical techniques which can provide a great deal of information about a system with minimal effort. In the case of CV, specifically, the current response of a system is measured as its potential is swept back and forth across a specified range at a constant rate. The characteristics of the resulting curve can then be used to draw meaningful conclusions about the behaviour of the system if analyzed correctly. A typical CV curve for a common highly reversible redox couple with fast kinetics can be seen in Figure 4, below.

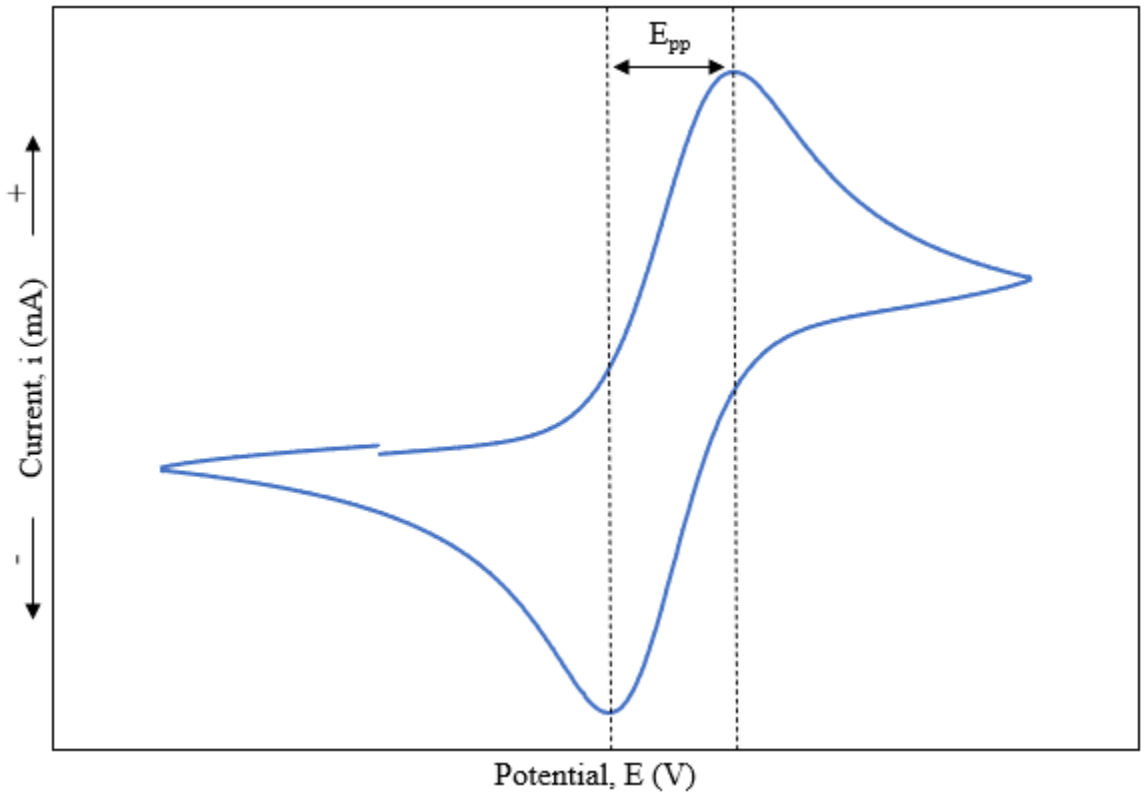

Figure 4. Typical CV curve for a Nernstian reaction with fast kinetics. Example taken from a scan at 50 mV/s in a ferricyanide system with a polished glassy carbon working electrode.

A distinct anodic peak appears during the forward part of the scan while a distinct cathodic peak appears during the reverse scan. In a CV for an unstirred solution, the peak position indicates the point at which the reaction becomes diffusion-limited, but a great deal more nuance is associated with the graph as a whole. CVs produced for different types of systems will be visually distinct in a number of ways, from the overall curve shape and symmetry to the ways in which key points shift or remain stationary as the scan parameters are varied. Changes to peak current and peak-to-peak separation provide a great deal of

information about a system. For example, a system could be identified as fully reversible if it meets all of the following criteria: the ratio of the anodic and cathodic peak currents (i_{pa}/i_{pc}) is equal to one, no shift occurs in the position of the peak currents along the x-axis with changing scan rates (i.e., no change in the peak-to-peak separation with changing scan rates), and the relationship between the peak current and the root of the scan rate is linear. In a system that is entirely surface reaction-limited (no diffusion limitations whatsoever) and fully reversible, no peak separation occurs at all, as illustrated in Figure 5. [11]

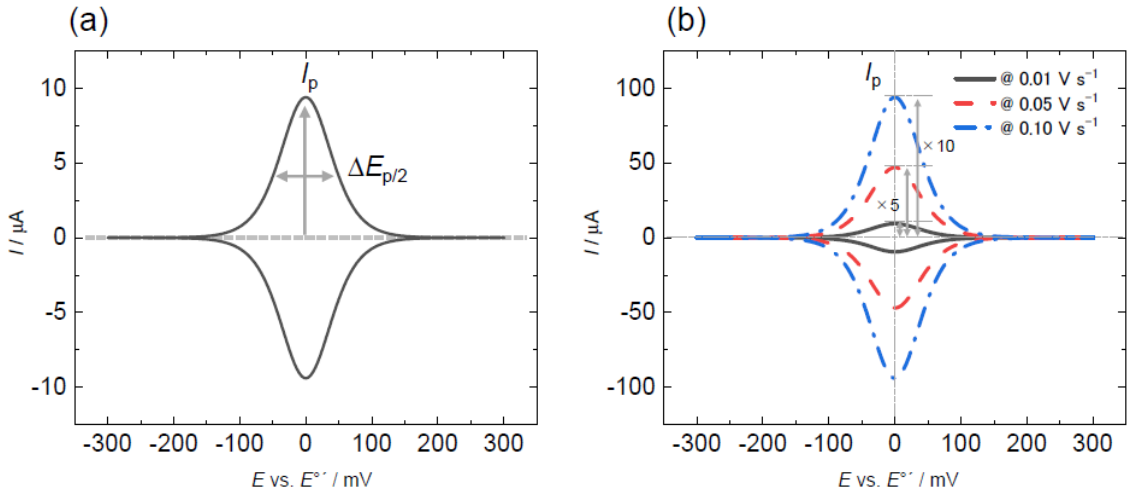

Figure 5. Theoretical CVs for a non-diffusion system at scan rates of (a) 0.01 V/s and (b) 0.01-0.1 V/s. Reproduced with permission from [11].

The peak-to-peak separation (E_{pp}) is taken as a general indicator of the apparent kinetics of an electrochemical system. For a fully reversible system with a diffusion-limited reaction, E_{pp} should be 56.5/n mV, with n representing the number of electrons being transferred in the reaction, independent of scan rate. Deviations from this specific set of

conditions (fully reversible, diffusion-limited), such as in the case of quasi-reversible reactions, can be used to glean information about the reaction kinetics of the system being studied. Some techniques for this are discussed later in this section, but it is first useful to understand more about the other parameter affecting the shape of a CV curve, the peak current, to have a greater picture of the system as a whole. A number of factors influence the scaling of the relationship between the peak current and the root scan rate of a given system. Several of these are illustrated in the Randles-Sevcik Equation (Equation 5), which assumes an electroneutral supporting electrolyte and diffusion-limitations for the active species [12].

$$i_p = 0.4463nFAC\sqrt{(\frac{nFDv}{RT})} \quad (5)$$

Here the variables i_p, n, F, A, C, D, v, R, and T represent the peak current, number of electrons being transferred in the redox reaction, Faraday's constant, electrode surface area, electrolyte concentration, electrolyte diffusion coefficient, scan rate, ideal gas constant, and temperature, respectively. It is important to note that these equations are derived for a flat electrode approximated as an infinite slab and the surface area corresponds to the geometric surface area. A lack of linearity in the relationship between the peak current and the root scan rate may suggest a few different avenues for deviation from the ideal reversible system, which can be understood through further analysis of the CV data. The two primary avenues which may describe this behaviour include electrochemical quasi-reversibility or electron transfer through species adsorbed on the surface of the electrode. [13]

For the case of Nernstian systems to which this linear relationship applies, it has been explored as a way of quantifying relative material porosity, an often-overlooked parameter in research, based on the change in the thickness of the diffusion layer with changing scan rates. This method, developed in a work by Punckt et al. [2], defines a variable α as the peak current of the forward reaction from a CV divided by the square root of the scan rate (Equation 6). From the Randles-Sevcik equation, this value should remain constant so long as the electrolyte composition, the reaction taking place, the temperature of the system, and the electrode surface area remain constant. Based on this knowledge, as well as the known change in diffusion layer thickness with the scan rate, a relative porosity factor, *P*, can be defined as the ratio of the α value at the highest scan rate to that at the lowest scan rate, as shown in Equation 7.

$$\alpha = I_{forw}/\sqrt{\nu} \tag{6}$$

$$P = \frac{\alpha(\nu_{max})}{\alpha(\nu_{min})} \tag{7}$$

In the case of a rough or porous material, the assumptions of the Randles-Sevcik equation are broken by the semi-infinite diffusion from the top of the porous film where the geometric surface area may only apply if the diffusion length is shorter than the roughness. In addition, for porous electrode materials, an electrochemical reaction will also likely occur within the internal porosity of the electrode film. When the diffusion layer thickness is greater than the largest pore radius, the internal porosity of the electrode will contribute to additional surface reactions at early stages while the following response will be more like

that of a non-porous/flat material. On the other hand, for a diffusion layer with a thickness below this pore size radius, the response is expected to proceed as in the semi-infinite diffusion case but with the additional surface area beyond the geometric surface area. By this logic, a completely flat electrode will maintain a P-value of exactly one, while porous electrodes would have values higher than this.

For quasi-reversible reactions, the peak-to-peak separation increases with the scan speed and can be linked directly to the reaction kinetics via various approaches such as the Matsuda number which is calculated for different E_{pp} by numerically solving the relevant equations describing CV for diffusion-limited, quasi-reversible systems. On the other hand, when the system is not diffusion-limited (e.g., in a porous electrode when the diffusion length is larger than the pore-size) and fully reversible, E_{pp} is zero, as shown in Figure 5. This means that the response to a porous electrode is the superposition of these two responses: the non-diffusion limited response of the internal porosity and surface roughness where i_p varies linearly with scan-rate and E_{pp} is zero, combined with the semi-infinite diffusion response where E_{pp} should change as a function of scan-rate for quasi-reversible kinetics and the current response should vary linearly with the square-root of the scan rate.

To take these complications into account, by plotting E_{pp} as a function of P, one can extrapolate to $P = 1$ where we can extract the E_{pp} for the non-porous system. This value can then be used to estimate a kinetic constant by the Matsuda approach. This procedure allows for the comparison of electrocatalytic performance of different materials that might possess different levels of porosity. An example of such a plot from the original work with porous,

drop-cast reduced graphene oxide (RGO) films and a ferricyanide system can be seen in Figure 6. The extrapolated value was confirmed by measuring the electrochemical response of relatively flat, non-porous monolayers of the same RGO deposited using a Langmuir-Blodgett deposition approach.

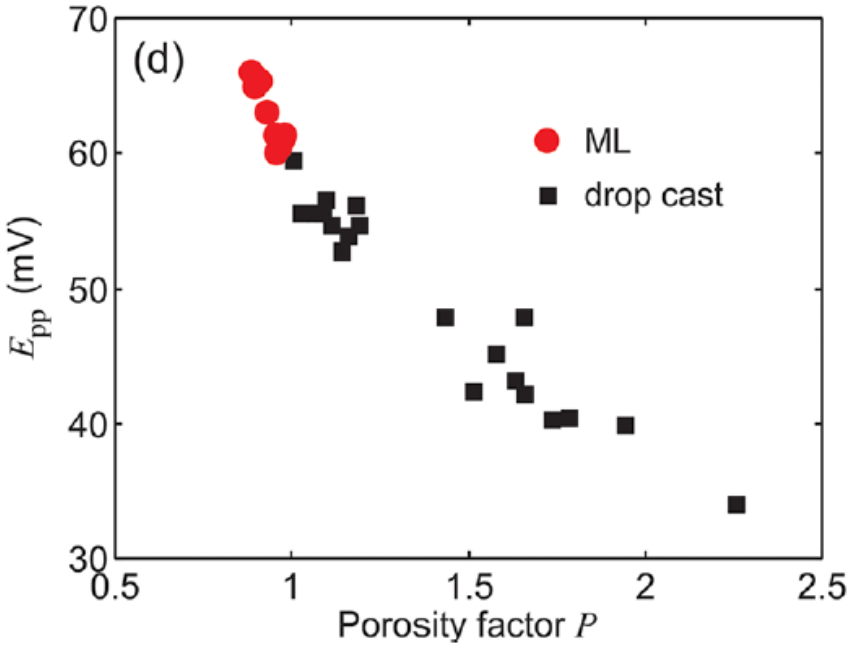

Figure 6. E_{pp} as a function of a porosity factor, P, for monolayer (ML) and drop-cast samples in a ferricyanide system. Reproduced with permission from [2].

Dunn's method is another way of visualizing the relative porosity of the active material on the working electrode, based on the current contribution of the diffusion-limited response. This method makes use of the relationship shown in Equation 8:

$$i(v) = k_1 v + k_2 v^{\frac{1}{2}} \quad (8)$$

The second term on the right-hand side of this equation stems from the relationship between the current and scan rate which is used in the Randles-Sevcik equation [14]. In that equation, however, a purely diffusion-controlled response is assumed whereas in Equation 8, an additional term is introduced to represent the current contribution from surface adsorbed reactions or those within pores smaller than the diffusion length (often referred to as the capacitive contribution in work applying this method to capacitive systems) to the overall current. These surface-adsorption and diffusion-limited components each scale with the scan rate, but in different ways, with the surface-adsorption contribution being proportional to the scan rate directly while the diffusion-limited contribution is proportional to the root of the scan rate. The k_1 and k_2 variables are constants which can be determined at a constant potential.

1.1.3 Monolayer Deposition

For a study aiming to extract intrinsic kinetic behaviour based on an entirely non-porous coating of a material to be practically meaningful, it must be possibly to fabricate such a coating in the first place. Otherwise, it would suffice to compare the performance at likely arbitrarily assigned "minimum porosity" points. Fortunately, a number of different methods exist to achieve monolayer coatings which may be used as non-porous reference points. While some of these methods, such as chemical vapour deposition (CVD) double as nanomaterial synthesis pathways, these are often highly energy intensive and difficult to

scale up. They also may not be similar to the material used in the redox flow battery. In this work, an alternative is explored through the deposition of Langmuir films directly onto various substrates.

In the original definition of such films by Agnes Pockels in the 19th century, they were described as a layer of self-assembled molecules on the surface of water. It was not until further research, conducted in the early 20th century that these films were successfully transferred to different substrates, vastly expanding their potential applications. Two main categories exist for the deposition of these Langmuir films, including both vertical and horizontal deposition. In vertical deposition, otherwise known as Langmuir-Blodgett (LB) deposition, the Langmuir film is formed on the liquid interface and the substrate is raised up from the liquid in a vertical orientation. Alternatively, in the Langmuir-Schaefer (LS) method, an example of horizontal deposition, a substrate held in a horizontal orientation under the surface of the water is carefully raised from underneath a Langmuir film on a liquid interface, with the deposition being complete once the remaining small layer of water between the film and the substrate has evaporated. [15] Basic diagrams to illustrate these two methods can be seen in Figure 7. This work employs a variation of the horizontal deposition technique in which the substrate is placed below the surface of the liquid prior to film formation. This is followed by compression to a specified surface pressure (defined as the difference between the surface tension with the film and that of pure water [16]) and the liquid itself is carefully removed from between the Langmuir film and the substrate so that the film is gradually lowered directly onto the substrate. Any remaining liquid which may

exist between the substrate and the film on a microscopic scale is evaporated over the course of the subsequent drying process.

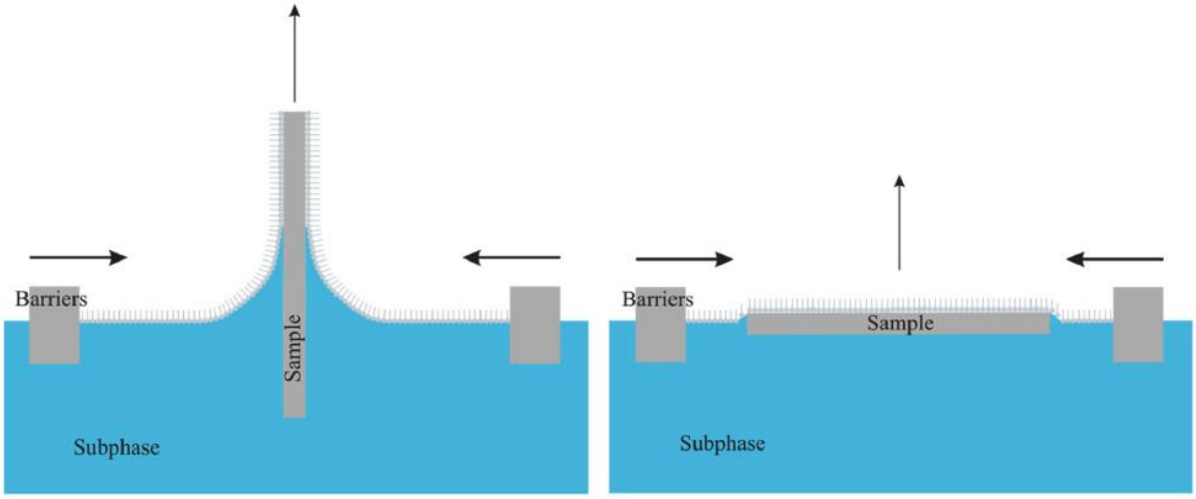

Figure 7. Schematic illustration of the LB (left) and LS (right) methods of Langmuir film deposition. Reproduced with permission from [15].

1.2 Literature Review

The highly promising nature of RFBs has led to an interesting research environment as different groups have attempted to overcome the main disadvantages of these systems or enhance the battery performance by other means.

1.2.1 Composite Membranes

Some of the strategies which have been explored to overcome the noted challenges faced by RFB membranes include the addition of filler materials to the polymer prior to casting, or the use of alternative membrane materials. This is the case in the research

conducted by Lou et al. [17] who incorporated GO directly into Nafion and recast it as a functional membrane with a thickness of 41μm. Similarly, Fang et al. [18] incorporated sulfonated graphene nanoplates into a recast Nafion membrane with the particular aim of enhancing the proton conductivity. Since Nafion is commercially available in several different thicknesses, that serves as an additional parameter to be considered when attempting to obtain the optimal VRFB configuration. While some of the freshly-cast composite membranes studied in literature have shown promising results, it would be a significant financial advantage if the same or greater improvements could be achieved using the commercially available membranes, as this would be much more scalable than the alternative. This pathway has been explored in a few different ways, with one potential technique including the sol-gel method in which the commercial membranes are pre-treated and then immersed in a solution prepared with components which will react with the treated membrane to form a composite material. An example of this technique includes the work of Xi et al. [19] to form a Nafion SiO_2 hybrid membrane which demonstrated improvements in CE and EE over current densities from 10-80 mA/cm^2 with the hybrid membrane exhibiting a maximum EE of 79.9% at 20 mA/cm^2 compared to 73.8% for the Nafion. A second example is that of Teng et al. [20] in the development of a Nafion/organic silica modified TiO_2 composite membrane which also achieved a notable improvement in CE when comparing the average value of 94.8% at 30 mA/cm^2 to the 90.8% from plain Nafion 117.

1.2.2 Graphene and Graphene Nanocomposites

A common material of interest explored to improve the performance of Nafion or other feasible ion-exchange membranes is graphene. Despite its somewhat recent discovery, this nanomaterial has garnered a massive amount of attention across numerous industries, with energy storage being no exception. The nanomaterial can be defined as a single atomic layer of sp^2 hybridized carbon atoms, with numerous possible synthesis pathways. Each of the two major categories of synthesis procedures, top-down (starting from a graphite material and breaking it down/exfoliating it into graphene) and bottom-up (synthesizing the layers from scratch), have their fair share of advantages and disadvantages which must be reconciled with the desired applications of the materials they produce. In most cases, the option with the most commercial appeal remains the top-down pathway as it provides significantly more promise for the level of scalability which is required for such applications. Still, the large-scale synthesis of graphene remains an issue and alternatives have also been proposed through the use of different carbon nanocomposites within the graphene family, including GO, and RGO, which are often able to exhibit many of the desirable qualities of graphene while being significantly easier to produce and containing defect/functional sites which sometimes prove beneficial depending on the system at hand. Among the works in this area is the research of Nia et al. [21] who applied RGO produced through an electrochemical reduction process to the carbon felt electrode of a VRFB and were able to achieve a 12% increase in the efficiency of the cell at 60 mA/cm^2 current density. Similar studies have also been conducted with other carbon nanomaterials, such as carbon nanofibers (CNFs) or

carbon nanotubes (CNTs), a composite of which is the primary material of interest in the work of Park et al. [22]. Applying this material to the carbon felt electrodes of a VRFB, an energy efficiency improvement of up to 64% was observed at 40 mA/cm^2, attributed to the enhanced surface defect sites and faster electron transfer rates provided by the nanocomposite material. This work examines several different materials within this category including GO, RGO, and heteroatom-doped graphene produced through electrochemical exfoliation.

While limiting vanadium crossover remains the primary goal of this work, it is equally important to maintain consideration for proton permeability through these membranes as well, since this mechanism is required in order for the cell to function. While protons are significantly smaller in size than any of the vanadium species of interest, the possibility exists for interactions between these atoms and the graphene lattice being introduced to the system which may limit the permeability in ways distinct from the molecular sieve phenomenon which contributes to reduced vanadium crossover. To evaluate this, Miao et al. [23] conducted a first-principles analysis of both hydrogen permeability and proton (H^+) permeability through a single sheet of graphene. In the case of pristine graphene, the analysis did indicate that protons could readily pass through the graphene lattice significantly more easily than the uncharged hydrogen atoms, each having different mechanisms by which they pass through the graphene. When examining a scenario which included graphene containing defects, both the hydrogen and proton permeabilities were improved over areas extending beyond the defect sites themselves.

1.3 Overview

The following sections will address the primary objectives of this thesis in two distinct chapters, each focussed on one of the following objectives:

- Address the known issue of vanadium crossover between half-cells through the application of a graphene monolayer to the Nafion ion-exchange membrane
- Determine the potential intrinsic catalytic effects of various graphene nanocomposites including NS-graphene, GO, and RGO

In Chapter 2, graphene monolayers are deposited onto Nafion membranes via a modified Langmuir-Blodgett deposition method and the resulting membranes are tested within a VRFB. Troubleshooting of the deposition process is discussed in detail and images are provided to illustrate the success of these coatings. A summary of the flow cell tests carried out by collaborators at the University of Calgary is provided. In Chapter 3, further tests are conducted using a 3-electrode setup in an attempt to determine the potential intrinsic catalytic effects of NS-graphene, RGO, and GO within the positive VRFB electrolyte. Monolayer and drop-cast samples are prepared for each of the materials of interest and the CV results from these tests are examined based on the methodology described by Punckt et al. (as discussed in Section 1.1.2) as well as a newly proposed analysis scheme based on Dunn's method. There is also a direct comparison of the results from monolayer samples, illustrating the marked performance improvement afforded by the RGO compared to all other samples.

Chapter 2 Graphene Monolayers to Reduce Vanadium Crossover

The following chapter, adapted from published work [1], describes the development of a composite membrane comprised of Nafion with a monolayer of electrochemically exfoliated graphene for the purpose of reducing vanadium crossover in VRFBs and improving overall performance.

2.1 Methodology

2.1.1 Materials

Graphite exfoliation was conducted in a two-electrode system using stainless steel as the counter electrode and a flexible graphite foil (GraphiteStore, INTRS-GSSM316) as the working electrode. Potassium hydroxide (KOH, MilliporeSigma) and ammonium sulfate ($(NH_4)_2SO_4$, MilliporeSigma) were used as the exfoliation electrolyte for each step. N,N-dimethylformamide (DMF, MilliporeSigma), 1,2-dichloroethane (DCE, MilliporeSigma), and ethanol (reagent alcohol grade, MilliporeSigma) were used to disperse the graphene and spread the dispersion onto the air−water interface. An aqueous solution containing 1.6 M vanadium oxysulfate ($VOSO_4$, 99.5% purity, NOAH Technologies) dissolved in 3 M sulfuric acid (H_2SO_4 MilliporeSigma), prepared in deionized (DI) water (>18.2 MΩ·cm), was used as the VRFB electrolyte in all experiments. Magnesium sulfate ($MgSO_4$, MilliporeSigma) was used for vanadium permeability experiments. Carbon paper (Sigracet 39AA, 280 μm thickness, pore size 43 μm, Ion Power) was used as an electrode material, while the bare

membrane materials were Nafion 117 and 115 membranes (thickness of 180 and 127 μm, respectively, Ion Power).

2.1.2 Nanomaterial Preparation

According to the technical data sheet for the NS-graphene, the material composition was shown via X-ray photoelectron spectroscopy (XPS) to be 93.2 at% carbon, 0.5 at% nitrogen, and 6.3 at% oxygen (the amount of sulfur was found to be 0.2-0.4 at% and was therefore not indicated in the overall composition table). Following the graphene synthesis process, approximately 20 mg of the obtained graphene film was dispersed in 15 mL of DMF in a 20 mL capacity scintillation vial. [16] The mixture was probe-ultrasonicated (60% amplitude, Model 150VT Ultrasonic Homogenizer, BioLogics, Inc.; Sonics Vibra-Cell VCX-500 Ultrasonic Processor, Sonics & Materials, Inc.) for 2 h under stirring and in an ice bath to prevent overheating. The mixture was then transferred into a centrifuge tube and spun (AccuSpinTM 3, Fisher Scientific, Waltham, MA) at 3600 RPM for 30 min. The resulting dispersion, referred to generally as G-DMF, was highly stable and used in addition to DCE to produce the deposition ink for the membrane coating procedure.

2.1.3 Coating Procedure

The membranes and additional substrates used in this study were coated with monolayers of the nanomaterials through a novel procedure based on both the LB deposition technique as well as the LS horizontal precipitation technique. This configuration results in the graphene acting as a selective barrier to ions which exceed the size of the average lattice

spacing, preventing the passage of the large vanadium ions across the Nafion, while still allowing for the necessary passage of protons for the completion of the circuit.

Immediately prior to deposition onto the air−water interface, an appropriate volume of the G-DMF dispersion (from 250 to 500 μL depending on the spreading behavior of the graphene sample) was added to DCE corresponding to a 3:1 DCE:DMF volumetric ratio. The DMF was found to be a good solvent for stably dispersing the graphene while the DCE facilitated solvent spreading and its water immiscibility prevented the mixture of the ink with the bulk of the water, allowing it to spread across only the surface. [16] At least 24 h prior to coating, the Nafion membranes were soaked in MilliQ water to ensure they were fully swollen with water. The membranes were then secured to a glass substrate, which had been cleaned with DCE and rinsed with MilliQ water, by placing the membrane corners between the glass plate and 2 cm squares of glass with N52 neodymium magnets (McMaster-Carr) below the glass plate and metal washers on top of the glass squares (see Figure 8). The magnets and washers were cleaned with ethanol prior to use.

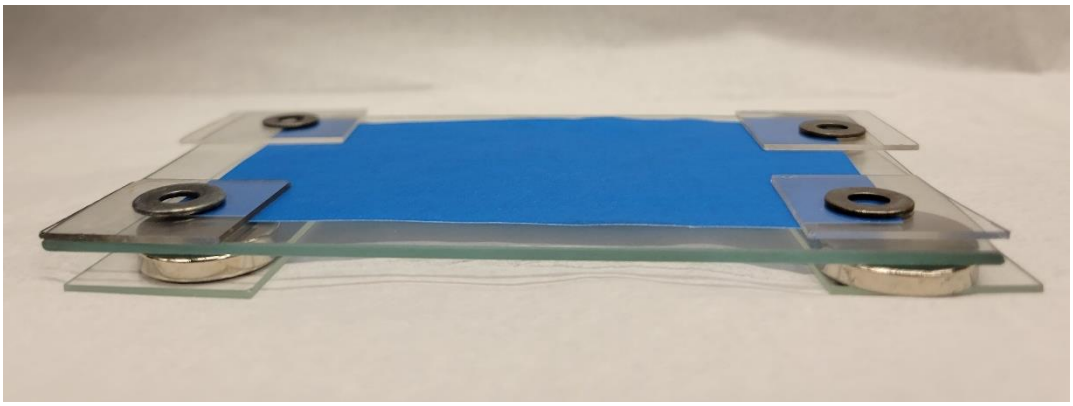

Figure 8. Example setup to secure a Nafion membrane to a glass substrate prior to modified-LB deposition. In this photo, a blue piece of paper is used in place of a Nafion membrane for easier visualization. Reproduced with permission from [1].

Several configurations were tested prior to the final version shown above. Initially, the membrane was held to the main glass substrate directly with paperclips. This resulted in a number of problems including the assembly floating to the surface of the water, the paperclips eventually leaving rust or other residue on the membrane, and the membrane becoming difficult to remove from the glass substrate following drying. Some images of membranes coated using this configuration can be seen in Figure 9. With the switch over to magnets, the first of these problems was resolved easily, as the magnets weighed down the assembly. To mitigate the final two issues, caused by the direct contact of the membrane and

the metal being used to secure it, small glass squares cut from standard microscope slides were found to be ideal as a final barrier between the membrane and the metal washers.

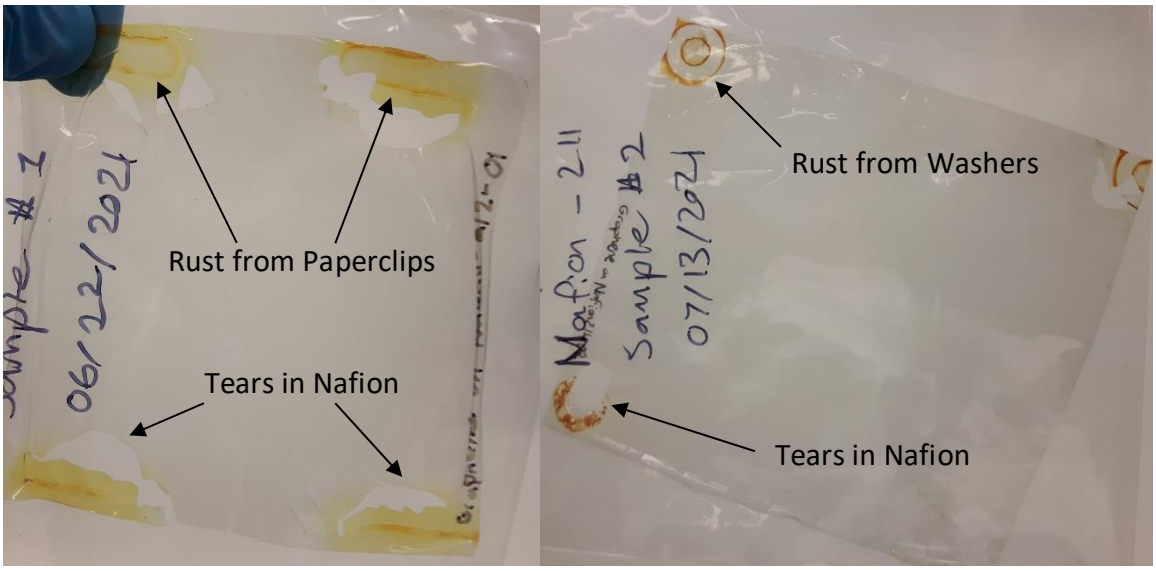

Figure 9. Examples of membranes which had been coated while secured to the glass substrate using only paperclips (left) or magnets and washers which were in direct contact with the membrane (right).

The secured membrane was placed face-up in an 8 cm wide Teflon deposition trough, the design of which was based on a commercial unit (Langmuir Trough G1, Kibron). Sections of the trough were divided using Teflon barriers, as depicted in Figure 10, with the membrane setup in the center of the trough. MilliQ water was added until just before the point of spillover such that the membrane setup was completely covered, and a significant meniscus was observed. For characterization purposes, additional substrates such as mica and silicon wafers (SPI Supplies; University Wafer, Inc.) were often included in the trough as

well. The surface of the water was cleaned using a vacuum aspirator until the compressed surface pressure change was found to be negligible to ensure that no surface debris remained.

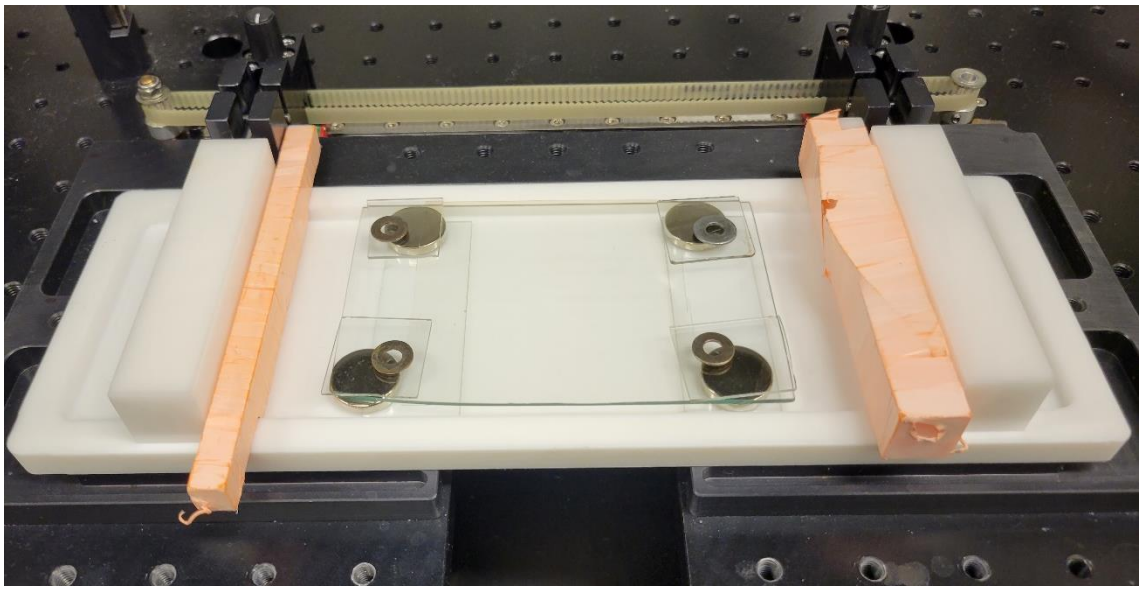

Figure 10. Typical setup for modified-LB deposition prior to the addition of water into the LB trough. Reproduced with permission from [1].

The coating process is illustrated in Figure 11. The graphene/DMF/ DCE ink was transferred into a glass syringe with an inner diameter of 14.6 mm connected to poly(tetrafluoroethylene) (PTFE) tube attachment with an inner diameter of 0.33 mm. The end of the PTFE tube was lowered toward the surface of the water to a height at which the ink droplets would hit the surface immediately after falling from the tube, and the ink was deposited onto the surface of the water at a rate of 0.1 mL/min. The dripping was continued until enough surface area was covered with a semitransparent film of graphene such that the solvent from the previous droplet did not have enough time to fully dissipate before the next

droplet falls (usually this corresponds to an uncoated circular area with a diameter of approximately 3 cm). The film was subsequently compressed to a surface pressure of approximately 20 mN/m by moving the Teflon barriers on either side of the film inwards at a rate of 5 mm/min, as measured with a paper Wilhelmy plate setup. Following compression, the coated area of the trough was reduced from approximately 144 cm^2 to approximately 104 cm^2, and the excess water was carefully removed from the trough using a vacuum aspirator which was placed to the left of the leftmost Teflon barrier so that the layer of graphene was lowered onto the surface of the substrate(s). The coated materials were allowed to dry under nitrogen overnight before being transferred into an oven to be further dried overnight at a temperature of 75 °C. The dried membranes could then be removed from the glass substrate. Images of the deposition ink, as well as an example of a coated membrane, are shown in Figure 12. Previous work also explored the application of these principles to achieve a continuous roll-to-roll coating of the Langmuir films, which is an integral step for the future scaleup of the deposition process for industrial applications [24].

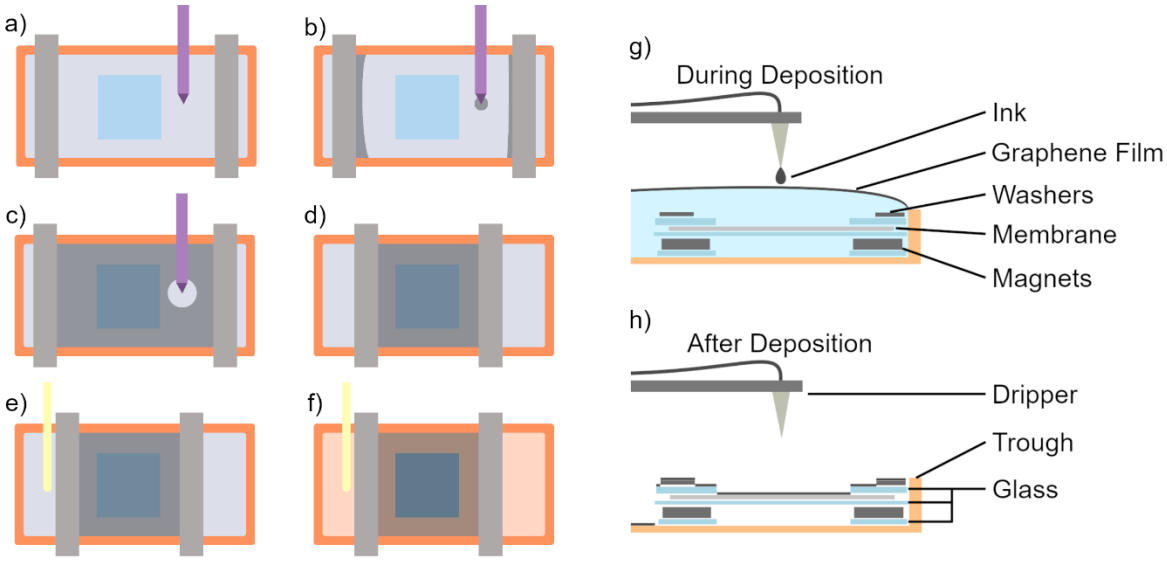

Figure 11. Schematic illustration of the deposition process from the top (a–f) and side (g, h). (a) The glass-supported Nafion membrane is placed in the center of the trough with barriers on opposite ends and water is added (the membrane is represented by the small blue square in the center). (b) The graphene ink is dripped onto the surface such that a film begins to form at either end of the trough. (c) Ink drops are added until the solvent from the previous droplet does not have enough time to fully dissipate before the next droplet falls. (d) The film is compressed by moving the Teflon barriers toward the center of the trough. (e) Vacuum (pictured to the left of the leftmost barrier) is used to remove the water from the outside of one of the barriers where there is no graphene film. (f) Water level drops below the level of the membrane and the graphene film is lowered onto its surface, completing the coating process. (g) Side view of the setup during deposition. (h) Side view of the setup after deposition. Reproduced with permission from [1].

Figure 12. (Left) G-DMF ink for deposition prepared at an initial concentration of 0.42 mg/mL. (Right) Nafion membrane (approximately 7.5 cm x 8 cm) coated with a single monolayer of graphene. Reproduced with permission from [1].

2.1.4 Membrane Characterization

2.1.4.1 Water Uptake and Swelling Ratio

The membrane samples (7.6 cm by 7.6 cm as required for the battery) were soaked in DI water at room temperature for 24 h. Residual water on the membrane surface was removed using adsorbent paper, and the mass and dimensions (length, width, and thickness) of the hydrated membrane samples were measured. The membrane samples were then dried in a vacuum oven at 100 °C for 24 h, and the mass and dimensions of the dry membrane were determined. The water uptake and swelling ratio of the membranes were determined from the percentage difference in mass and volume, respectively, of the hydrated and dry

membranes.[25-27] The measurements were repeated for three membrane samples in each case.

2.1.4.2 Ion Exchange Capacity

The ion exchange capacity (IEC) of the membrane was obtained by titration [25-27]. Dry membrane samples were immersed in 50 mL of 3.0 M NaCl solution for 24 h at room temperature to exchange protons with sodium ions. The solution was then titrated with 0.1 M NaOH to determine the proton concentration. The IEC was calculated by dividing the amount of NaOH required to neutralize the solution by the dry mass of the membrane. The IEC of three samples was determined in each case.

2.1.4.3 Area Specific Resistance and Proton Conductivity

To evaluate the area specific resistance of the membrane (r), the membrane samples were soaked in a solution of 1.6 M $VOSO_4$ and 3.0 M H_2SO_4 for 24 h. The membrane was placed in a 5 cm^2 RFB cell filled with 3.0 M H_2SO_4 electrolyte. The cell resistance was determined in the presence (r_1) and absence ($_{r2}$) of the membrane by electrochemical impedance spectroscopy (EIS). The effective membrane area (S) of the cell was 5 cm^2. The area specific resistance of the membrane (Ω cm^2) was calculated using Equation 9: [28]

$$r = (r_1 - r_2) \times S \quad (9)$$

The proton conductivity of the membrane samples was determined by EIS in the RFB setup. Impedance was measured in the range of 1 Hz to 100 kHz. The membrane samples were soaked in DI water for 24 h at room temperature before the experiment to ensure the

samples were fully hydrated. The proton conductivity (σ) was calculated according to Equation 10: [26, 29]

$$\sigma = \frac{L}{R \times A} \tag{10}$$

where L, R, and A are the thickness, resistance, and cross-sectional area of the membrane, respectively.

2.1.4.4 Vanadium Permeability

Although all vanadium species present in the VRFB (V^{2+}, V^{3+}, VO^{2+}, and VO_2^+) may pass through the membrane, most studies of membrane crossover have only measured the membrane permeability for VO^{2+} ions [26, 29-33]. In this study, a similar approach is followed since the effect of the modification of the membrane on the permeability of other vanadium species is expected to be similar to that for VO^{2+}. The VO^{2+} permeability through the membranes was evaluated using the cell designed for VRFB charge−discharge testing (as described below). Membrane samples (effective area of 5 cm^2) were sandwiched in the cell between the carbon paper electrodes. One tank was filled with 50 mL of 1.6 M $VOSO_4$ in 3 M H_2SO_4 solution (the source reservoir), and the other was filled with 50 mL of 1.6 M $MgSO_4$ in 3 M H_2SO_4 solution (the receiving reservoir) to balance ionic strength and reduce osmotic pressure effects. These solutions were circulated through the cell on each side of the membrane using a dual-head peristaltic pump. Samples on the $MgSO_4$ side were periodically withdrawn at timed intervals and the vanadium ion concentration was determined using inductively coupled plasma optical emission spectroscopy (ICP-OES, Varian 725). The VO^{2+}

permeability (*P*) of the membrane was calculated from the rate increase in concentration in the $MgSO_4$ solution (Equation 11)

$$P = \frac{V_B L}{S(C_A - C_B(t))}\left(\frac{dC_B(t)}{dt}\right) \quad (11)$$

where V_B is the volume of the $MgSO_4$ solution, L is the membrane thickness, S is the effective membrane area, C_A is the VO^{2+} concentration in the source reservoir, t is the duration of the experiment, and $C_B(t)$ is the measured VO^{2+} concentration of the receiving reservoir at time t. [25]

2.1.4.5 Surface Characterization

Scanning electron microscopy (SEM, Quanta FEG-250, Thermo Fisher Scientific) studies of the membrane before and after coating were used to evaluate the morphology and composition of the top surface and cross section of the membrane. AFM (Nanoscope Multi-Mode AFM, Veeco, Digital Instruments MMAFM-2) of the graphene coating was used to evaluate the coverage and morphology of the coated surface. AFM was conducted after the graphene coating was applied using the method described in Section 2.1.3 on substrates including 1 cm × 1 cm squares of freshly cleaved mica, p-doped silicon cleaned with ethanol, and samples of the swollen Nafion 117. The silicon and mica samples were dried overnight under nitrogen at room temperature, and the Nafion samples were dried overnight in an oven at 75 °C. Samples were imaged using AFM under ambient temperature and humidity. The silicon and mica samples were imaged using contact mode with a silicon nitride tip (Bruker, nonconducting silicon nitride, cantilever 600 nm), and a scan rate of 1 Hz was used with 512

samples/line. The Nafion samples were imaged using tapping mode to minimize potential damage from lateral forces on the softer polymeric substrates, using an antimony-doped Si tip (Bruker, 0.01−0.025 Ω- cm, 127 μm length, 35 μm width, k: 42 N/m). These images were also taken at a scan rate of 1 Hz and 512 samples/line. A constant drive frequency of 359.13 kHz was used. High-resolution transmission electron microscopy (TEM) images of the graphene were collected using an FEI Tecnai G220 equipped with an X-Max energy-dispersive X-ray spectroscopy (EDX) detector with an acceleration voltage of 200 keV. In addition, Raman spectroscopy (α 300R WITec GmbH, Germany) was conducted on samples of the graphene-coated membrane and bare membrane to confirm the presence of graphene coated on the membrane surface.

2.1.5 VRFB Charge−Discharge

To study the VRFB charge−discharge, a single flow cell (5 cm^2 effective area, supplied by Fuel Cell Technology, Inc.) with a serpentine flow field was used. Graphite plate current feeders with bare, thermally treated (1 h at 500 °C in air) carbon paper (Sigracet 39AA) electrodes, and bare or graphene-coated Nafion membranes were used in the cell. The membrane was soaked in DI water for 24 h before use [6, 34, 35]. Figure 13 shows a schematic of the VRFB flow cell testing system used in this study. In all experiments, the negative and positive electrolyte tanks each contained 20 mL of 1.6 M vanadium electrolyte in 3 M H_2SO_4. The electrolytes were prepared using $VOSO_4$, and an initial charging procedure described in previous studies was followed [6, 36]. The electrolyte solutions were circulated through the cell at a flow rate of 20 mL/min using a dual-head peristaltic pump

(Masterflex, Cole Parmer). Humidified nitrogen was continuously bubbled through the electrolyte solution 30 min before and during the charge−discharge experiment to remove dissolved oxygen. Charge−discharge experiments were performed at constant current densities ranging from 10 to 100 mA/cm^2, using cut-off voltages of 1.65 V for charge, and 0.8 V for discharge. A potentiostat (BioLogic VSP/VMP3B-20) operating in galvanostatic mode was used for the charge−discharge experiments. The VRFB efficiencies were determined based on Equations 2-4, as defined in Section 1.1.1.[6, 7]

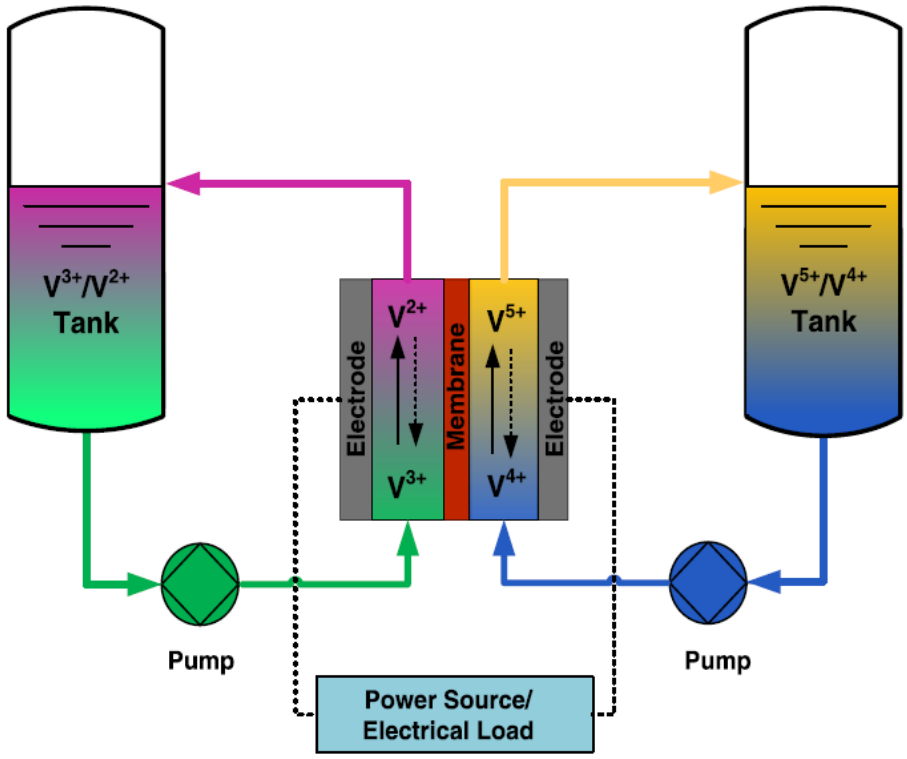

Figure 13. Schematic illustration of the VRFB setup used for flow cell tests. Reproduced with permission from [1].

2.2 Results

AFM was used to confirm the successful coating of sample substrates that had been immersed in the trough in addition to the Nafion (Figure 14). These images show a dense, thin layer of graphene, with an average estimated coverage of 93%. The coating, referred to as a monolayer, is indeed confirmed to be consistently only one or two sheets of graphene in depth, corresponding to an estimated average coating thickness of less than 5 nm. The strength of the bond between the graphene and the Nafion was seen both visually and through additional imaging. After coating, a semi-transparent grey layer was evident on the membrane, and this layer remained stable on the membrane through handling and throughout the electrochemical testing. AFM images of the graphene on Nafion were obtained before and after electrochemical testing to show that the material was not disrupted over the course of testing. Some of these images can be seen in Figure 15, below. A notable feature of the graphene coating on the Nafion is its topology when compared to the graphene deposited onto a smooth surface such as mica. Since the Nafion is known to swell when wet and contract when dry, and the graphene is deposited on the Nafion while it is wet, the deposition surface experiences significant changes. From the AFM images of the graphene on the dried Nafion, it can be seen that this resulted in wrinkling of the graphene layer as opposed to some other failure mechanism such as the coating breaking apart and sheets overlapping as the

Nafion contracts. This result is significant in that it demonstrates the strength of both the graphene layer itself and the bonds between this layer and the Nafion substrate.

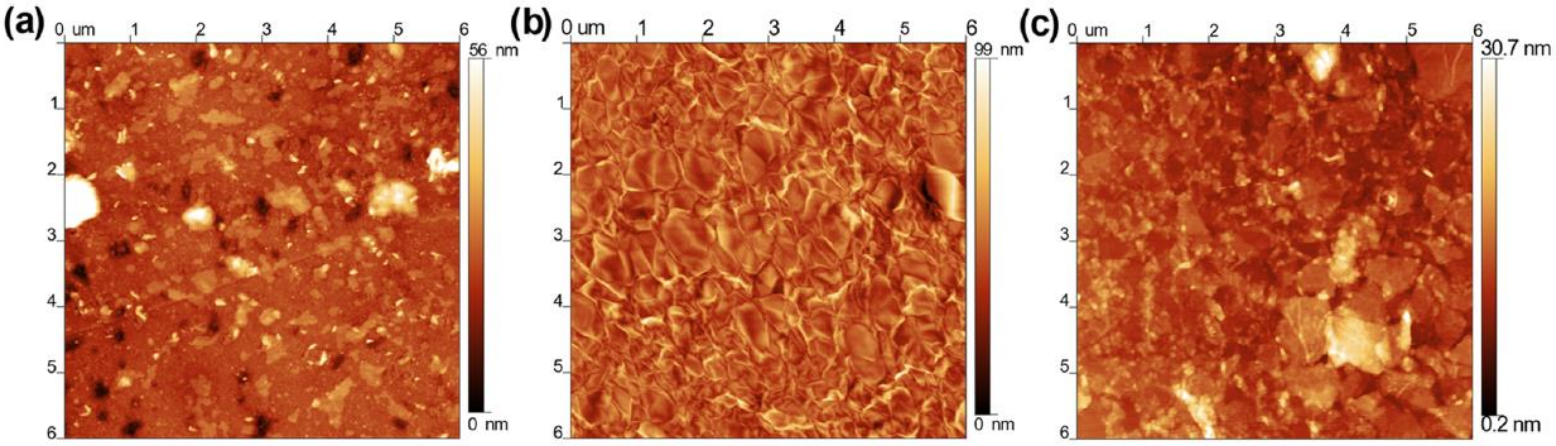

Figure 14. AFM images of (a) top surface of uncoated Nafion 117, (b) top surface of graphene-coated Nafion 117, and (c) top surface of graphene-coated mica. Reproduced with permission from [1].

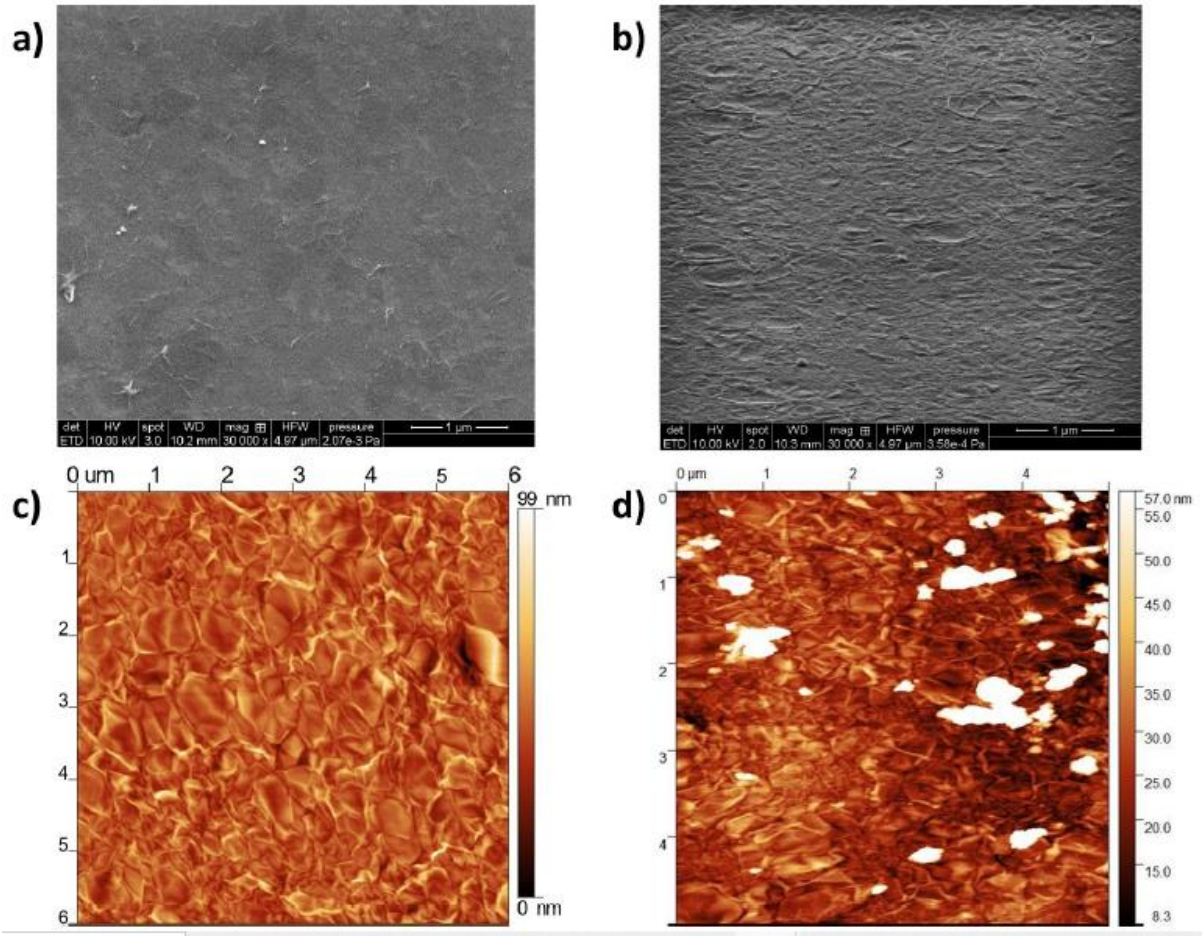

Figure 15. Secondary electron SEM images (a and b) of the top surface of graphene-coated Nafion 117 a) before cycling and b) after cycling; AFM images (c and d) of the top surface of graphene-coated Nafion 117 c) before cycling and d) after cycling. Reproduced with permission from [1].

The VO^{2+} permeability and ion selectivity of graphene-coated and bare Nafion membranes are compared in Figure 16c, with the water uptake and area-specific resistance shown in Figure 16a and Figure 16b, respectively. The selectivity is the ratio of proton

conductivity to VO^{2+} permeability, with a higher selectivity being a qualitative indicator of a better membrane for VRFB applications [37]. The VO^{2+} permeability of the graphene-coated Nafion 117 and Nafion 115 membranes are 75% and 53% lower than those for the bare Nafion, respectively. Studies of pristine single-layer graphene coated onto Nafion have demonstrated that graphene is only permeable to H^+ ions, and no other species will pass through the graphene structure [38]. As the graphene basal planes block the transport of VO^{2+}, these ions are forced to pass through the gaps between the graphene platelets. The lower water uptake and blocking effect of the graphene nanoflakes slightly decrease the proton conductivity of the graphene-coated membranes. However, as the reduction in the VO^{2+} permeability is much greater than the reduction in proton conductivity [25, 37], the graphene-coated membranes show higher selectivity than the bare Nafion membranes: 243% higher in the case of graphene-coated Nafion 117 and 65% higher in the case of graphene-coated Nafion 115. The higher selectivity indicates that the graphene coating improves the membrane properties for VRFBs, and a higher battery performance may be expected. The microstructure of the graphene has fewer channels for VO^{2+} transport than the bare Nafion membrane due to the graphene flakes covering the membrane surface. The two-dimensional graphene flakes serve as barriers to prevent VO^{2+} migrating through the membrane structure. To be transported through the Nafion matrix, VO^{2+} ions are constrained to the gaps between flakes, increasing the transport resistance. The VO^{2+} permeability also decreases with membrane thickness due to the longer transport pathway [25, 26, 29, 30, 32, 39]; hence, the VO^{2+} permeability of Nafion 117 is lower than that of Nafion 115 (Figure 16c).

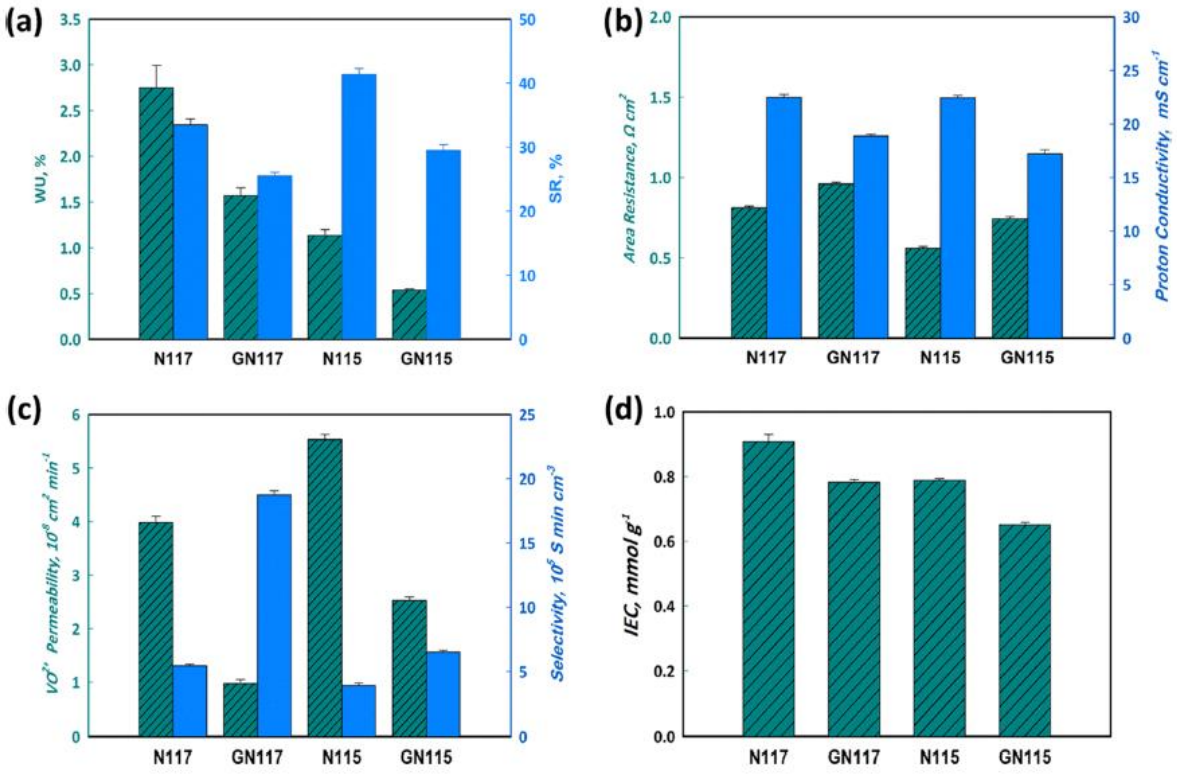

Figure 16. Comparison of the properties of Nafion and graphene-coated Nafion membranes: (a) water uptake and swelling ratio; (b) area resistance and proton conductivity; (c) VO^{2+} permeability and selectivity; and (d) IEC. N117 and N115 represent bare Nafion 117 and Nafion 115, respectively. GN117 and GN115 are the graphene-coated Nafion 117 and graphene-coated Nafion 115, respectively. Reproduced with permission from [1].

Figure 17 shows the contact angle of the uncoated and graphene-coated Nafion 117, which are approximately 45° and 41°, respectively. The contact angle of the membranes confirms that they are both hydrophilic. The functional groups present on the graphene provide hydrophilicity, and no significant change in the contact angle of the Nafion is

apparent after graphene coating. The IEC of the bare Nafion is found to be approximately 0.8−0.9 mmol/g (Figure 16d) similar to the theoretical value [40] of 0.91 mmol/g. The IECs of the graphene-coated Nafion 117 and Nafion 115 membranes are 13% and 16% lower than that of bare Nafion, respectively, likely due to the graphene layer which decreases the availability of ionic groups in the structure [30]. Ionic groups may be unavailable due to direct interactions with the graphene, or as a result of decreased water uptake because of steric confinement of the aligned graphene flakes, limiting the expansion of Nafion clusters. The results of flow cell testing for the determination of self-discharge time, CE, VE, and EE are summarized in Figure 18 and discussed in greater detail in the published work, a copy of which is included in the Appendix. [29]

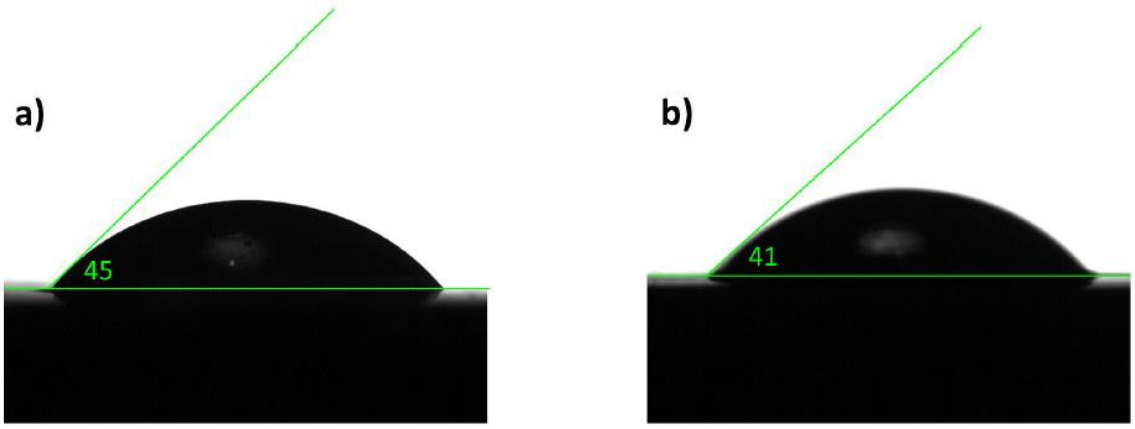

Figure 17. Static water contact angle on a) Nafion 117 and b) graphene-coated Nafion 117. Reproduced with permission from [1].

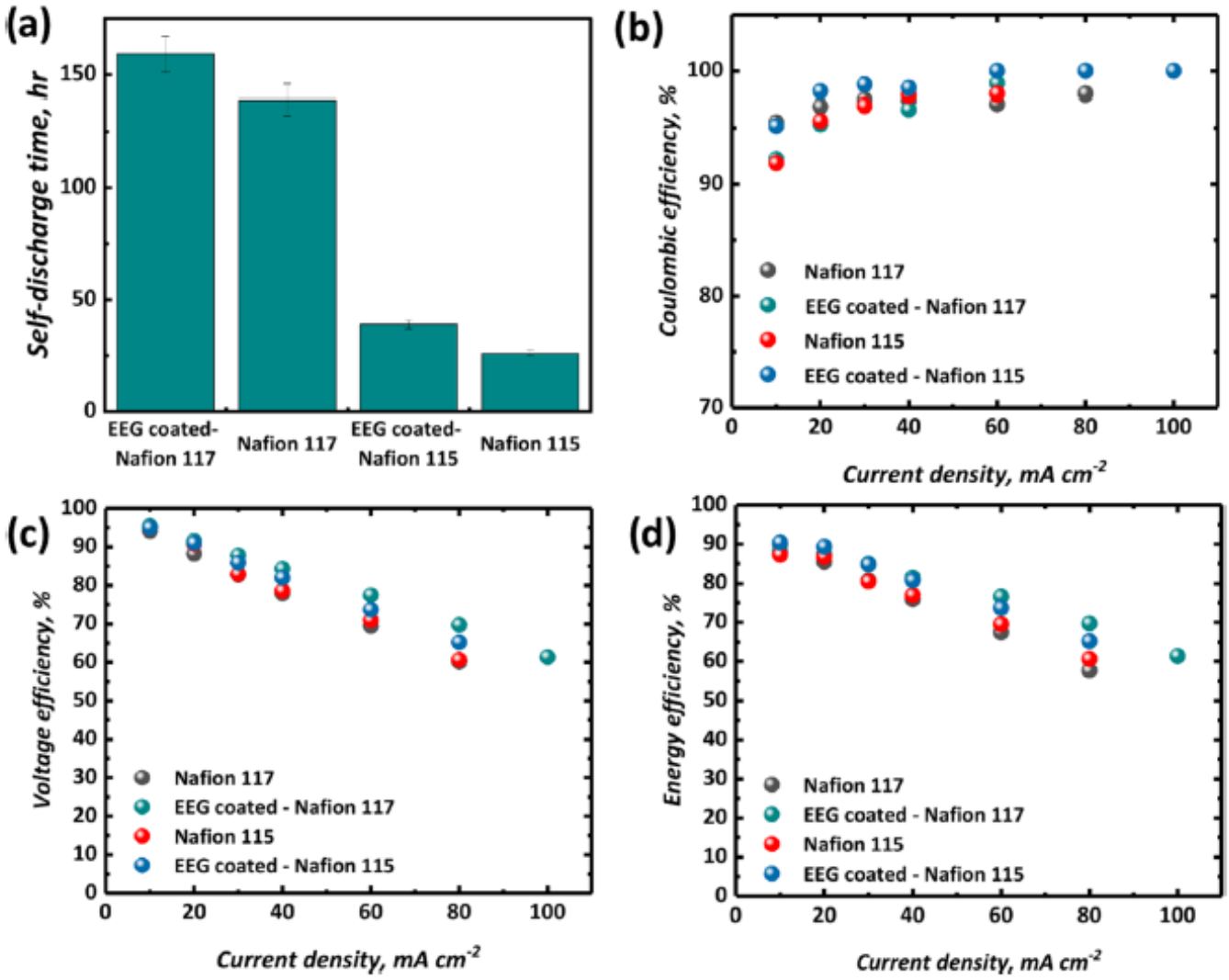

Figure 18. Comparison of VRFB performance using bare and graphene-coated Nafion 115 and 117 membranes: (a) self-discharge curves at 50% SOC and charge−discharge efficiencies at a range of current densities, including (b) CE, (c) VE, and (d) EE. Reproduced with permission from [1].

2.3 Conclusions and Future Work

When assessing the success of the work detailed in this chapter, several aspects may be considered individually. In the case of the coating itself, a simple and high-quality coating was achieved through the horizontal deposition of a Langmuir film directly onto the surface of a commercial Nafion membrane. The novel approach to deposition, originally developed within the Pope group by Dr. Luzhu Xu, which applied two different co-solvents in the deposition ink in order to spread and suspend the film was successfully adapted to this system in order to produce scalable and reproducible coatings. Subsequently, the coated membrane was tested within a VRFB setup and found to improve the vanadium permeability significantly while still maintaining a high enough proton permeability to exhibit higher overall selectivity. The strong adhesion of the graphene coatings to the membranes was confirmed through the analysis of the coating on the membrane before and after cycling.

Regarding future work, some related tests have been conducted and shown initial promise for further exploration. The most pressing of these projects, as mentioned in an earlier section, is that of scaleup through the optimization of a roll-to-roll deposition procedure. This is a critical step in ensuring the commercial viability of these composite membranes. Beyond this, some tests have been conducted (though not detailed in this chapter due to the remaining work still needing to be done) using graphene functionalized with nitrogen/phosphorus (NP-graphene). These are hypothesized to produce different effects to those observed from the NS-graphene employed in this project based on the different particle interactions which may occur based on this functionalization. Successful coatings have

already been achieved with this alternative doping scheme and initial flow-cell testing is promising. Additionally, work has been started on an examination of the effect of different Nafion thicknesses (also graphene-coated) on VRFB performance. This will allow for further system optimization as a reduced membrane thickness typically leads to a trade-off in proton permeability and vanadium crossover, which would ideally be mitigated substantially by the application of a graphene monolayer.

Chapter 3 Catalytic Behaviour of Nanomaterials within the Vanadium System

In this chapter, various nanomaterials are tested for their catalytic potential for the positive electrode reaction of a VRFB. The analysis methods chosen for this section were selected with the intention of finding intrinsic catalytic potential through non-iterative analysis.

3.1 Methodology

3.1.1 Materials

Materials with suppliers not indicated here are the same as in the previous chapter. In addition to these materials, RGO (Global Graphene Group Inc.), butanol ($CH_3(CH_2)_3OH$, Supelco), and GO produced through Tour's method [41] were used. For the electrochemical testing in this case, an aqueous solution containing 0.1 M vanadium(IV) sulfate oxide hydrate ($VOSO_4 \cdot xH_2O$, 99.9% purity, Alfa Aesar) dissolved in 3 M sulfuric acid (95-85%, Sigma Aldrich), prepared in MilliQ water was used. The working electrode used was glassy carbon (SPI Technologies), with a silver/silver chloride reference electrode (Ag/AgCl, CHInstruments) and a platinum wire counter electrode (CHInstruments).

3.1.2 Nanomaterial Preparation

The graphene dispersion used in this set of tests is the G-DMF prepared in the previous section. The RGO employed in these experiments was commercial-grade material

dispersed in DCE via probe ultra-sonication at 60% amplitude for 30 mins in order to obtain a final concentration of 0.5 mg/mL. The GO used in tests for this section was obtained directly from other lab members, having been initially produced through Tour's Method.

3.1.3 Electrode Preparation

Glassy carbon (GC) working electrodes were prepared for testing according to slightly varying methods for monolayer and non-monolayer samples. In all cases the GC substrates were polished using alumina polishing compound at three different levels (5, 0.3, and 0.05 μm) from coarsest to finest for 15 minutes at each level. Following the polishing, the GC was bath ultrasonicated (Model 15337409 Ultrasonic Bath, Model PS-60A, Digital Ultrasonic Cleaner, Jakansonic Cleaner Company Ltd.) in a vial with MilliQ water in order to remove any residual polishing compound.

For non-monolayer samples, the material of interest was drop-cast onto the surface of the electrode in several layers. For the RGO, each drop-cast layer consisted of two drops from a glass pipette. For the graphene samples, the G-DMF dispersion described in a previous section was used and each drop-cast layer consisted of 10 μL of this dispersion. Each layer was allowed to dry thoroughly at ambient temperature before the next was added. After the final layer was dry, 10 μL of a 0.1 vol.% Nafion 117 solution was added as a binder to the top to prevent the drop-cast material from detaching from the electrode during testing.

Monolayer samples were prepared according to the same procedure as the modified-LB membrane coatings described in a previous section, simply including the GC alongside

any additional substrates being coated in the trough. For the samples using RGO, the coating process was largely the same as for graphene, with the only notable difference being the composition of the deposition ink. In the case of RGO, the prepared 0.5 mg/mL stock dispersion was bath sonicated in an ice bath for 10 minutes, and 1 g of this dispersion was further diluted with 1 g of DCE. Following this, 123.4 μL of butanol was very slowly added to the side of the vial containing the dilution, with the DMF-butanol system acting to suspend and spread the film on the air-water interface similarly to the DMF-DCE system used for the graphene samples. The rest of the deposition process remained the same as with graphene.

Monolayer-coated samples were allowed to dry under nitrogen at room temperature overnight prior to use in electrochemical testing. For the RGO samples, the addition of a 0.1 vol% Nafion 117 layer was deemed to be a necessary precaution upon the visual inspection of the dried monolayer samples. This was not the case for the monolayer samples of the other nanomaterials. Through previous tests, it had been found that the addition of this protective layer does not significantly influence the current response of the system at this low concentration.

3.1.4 Electrolyte Preparation

The electrolyte used for testing was prepared using concentrated sulfuric acid and crystalized vanadyl sulfate in several steps out of an abundance of caution for the highly exothermic process. In an Erlenmeyer flask, 2.4 g of the $VOSO_4 \cdot xH_2O$ was added alongside 40.1 mL of MilliQ water and was stirred until dissolved. Subsequently, the flask was covered

with Parafilm and bath ultrasonicated in an ice bath for 50 minutes. While this solution was sonicating, the concentrated sulfuric acid was diluted by adding 16.7 mL of acid to a beaker with 25 mL of MilliQ water, also in an ice bath. Following the sonication of the vanadium solution, the diluted acid was carefully added to the Erlenmeyer flask and the final volume was adjusted to 100 mL by adding approximately 18.2 mL of MilliQ water. The flask was then covered once again and returned to the bath ultrasonicator to be sonicated in an ice bath for an additional 50 minutes. The final electrolyte was allowed to sit overnight before being used in any experiments, with a final composition of 0.1 M $VOSO_4 \cdot xH_2O$ and 3 M H_2SO_4. The 3 M H_2SO_4 solution which was used for background measurements was prepared in a similar fashion, simply excluding the steps in which the $VOSO_4 \cdot xH_2O$ is added.

3.1.5 Electrochemical Testing

The catalytic potential of each of the nanomaterials being investigated in this report was conducted through three-electrode testing using Ag/AgCl as a reference electrode, platinum wire as a counter electrode, and GC coated with the material of interest as the working electrode. CV scans were conducted from 0 to 1.6 V vs Ag/AgCl at 5, 10, 20, and 50 mV/s with electrochemical impedance spectroscopy (EIS) following each CV step and a two-minute pause between the application of each scan rate. The ZIR routine within the EC-Lab software for the potentiostat was used to compensate for 85% of the ohmic drop estimated by impedance spectroscopy from 1 MHz to 1 Hz with an amplitude of 10 mV. Background scans were conducted in 3 M H_2SO_4 with this data subsequently subtracted from

the curves of scans conducted in an electrolyte composed of 0.1 M $VOSO_4 \cdot xH_2O$ and 3 M H_2SO_4.

3.2 Results

3.2.1 Monolayer Deposition

AFM was used to evaluate the success of the monolayer deposition method, which varied for each nanomaterial. Images of the various materials on mica and silicon wafers can be seen in Figure 19 and Figure 20 below. While it is clear that the graphene depositions produce high-quality (if somewhat overly-compressed) sheets, the GO and RGO samples are not so clearly successful. Although good GO coverage was achieved, over-compression resulted in the stacking of some of the GO flakes. As for the RGO, examination of the SEM images reveals how much the morphology of this material differs from the other nanomaterials in this study (Figure 20e and f). The RGO is significantly rougher than either of the other materials. Also, despite this and the fact that large portions of the RGO surface remain uncoated, the film was otherwise quite uniform. Based on these images, the samples coated with this technique may continue to be treated as monolayers for the purposes of these tests. While some stacking is apparent in the GO, thus making the description of "few-layers" more technically apt, the overall film quality is thin enough that it remains a good comparison point for the experiments described in this report. Furthermore, pores within the

restacked sheets are likely inaccessible by electrolyte and redox probes.

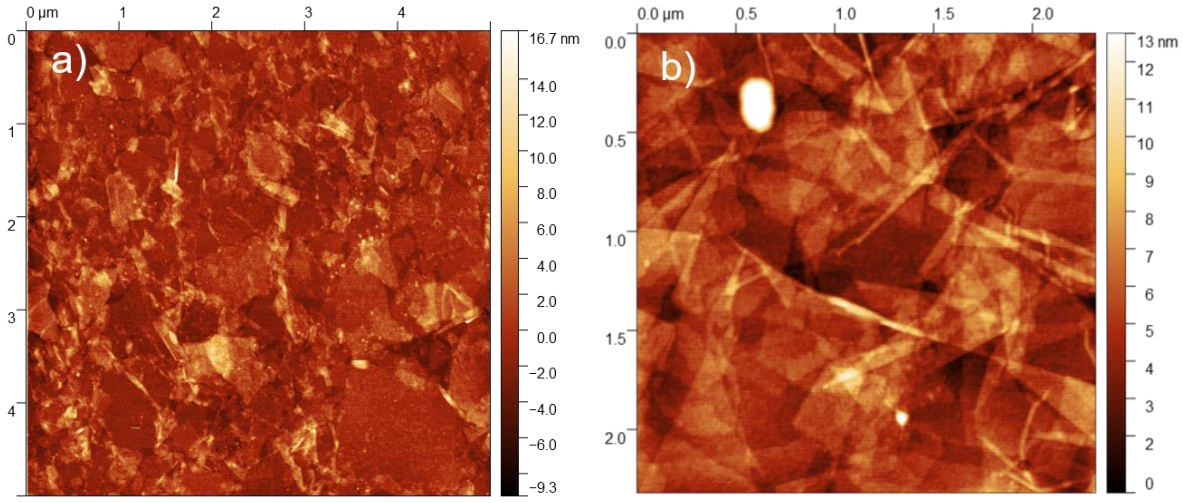

Figure 19. AFM images of (a) NS-graphene on mica and (b) GO on silicon. No AFM images could successfully be captured for the RGO.

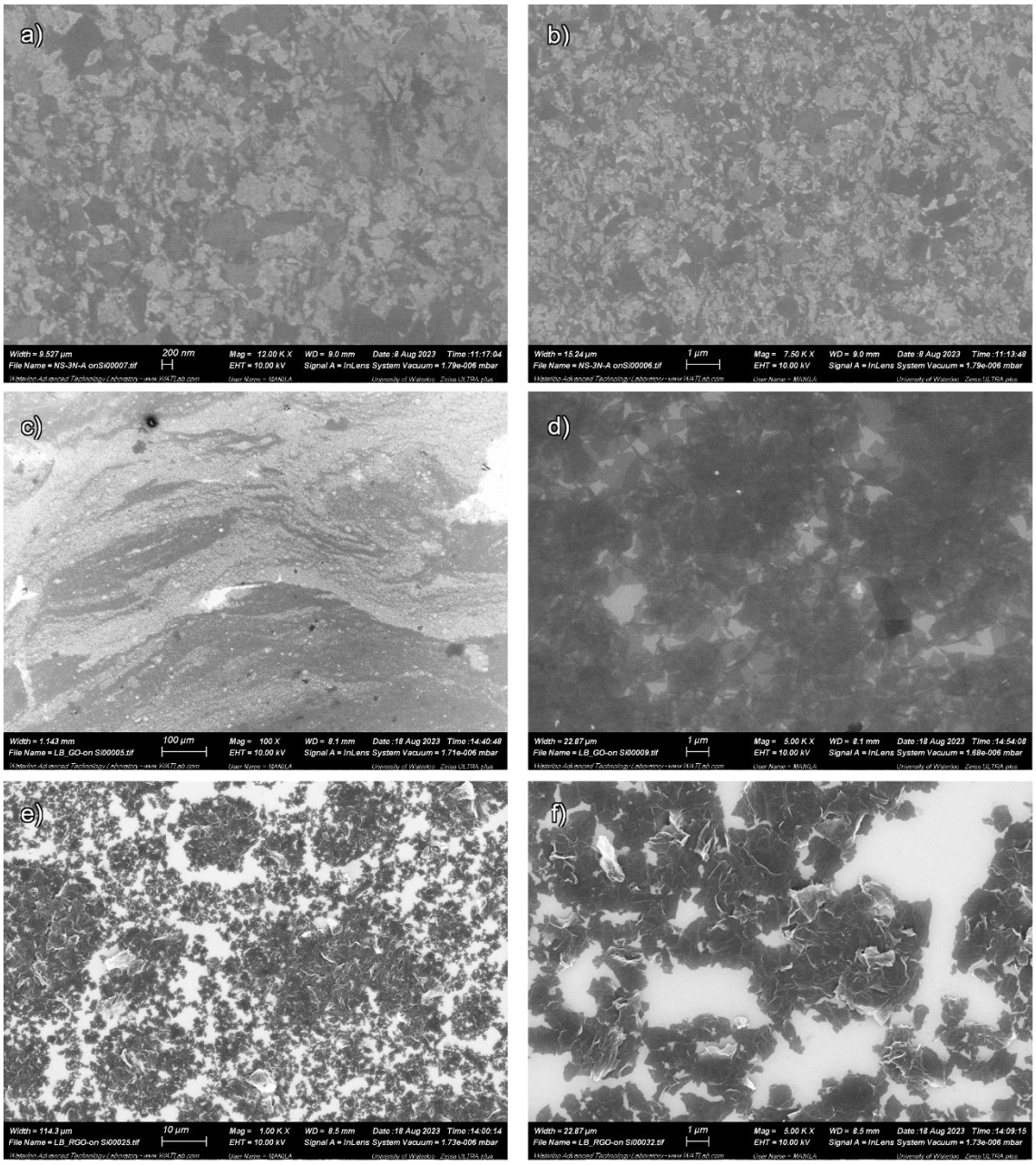

Figure 20. Secondary electron SEM images of modified-LB-deposited (a,b) NS-Graphene, (c,d) GO, and (e,f) RGO on silicon wafer substrates.

3.2.2 Porosity Analysis

3.2.2.1 Punckt Method

As part of the initial exploration of the Punckt analysis method described in Section 1.1.2, tests were done using the same buffered ferricyanide system and potentiostat settings as described in the original paper. Tests were conducted using RGO drop-cast onto GC with the aim of optimizing the experimental procedure to limit potential sources of error before applying it to a different electrolyte system. CV results for some of these ferricyanide tests can be seen in Figure 21. In this way, the difference in behaviour between samples with no RGO and a few layers of RGO could be seen. As expected, the addition of the nanomaterial resulted in a notable reduction in the peak-to-peak separation, as noted in Table 1, as well as a reduced activation overpotential as evidenced by the closer onset potentials for current flow in both the oxidation and reduction reactions. An examination of the change in peak current with the root of the scan rate also showed expected behaviour, with consistent linear relationships in each test, as shown in Figure 22.

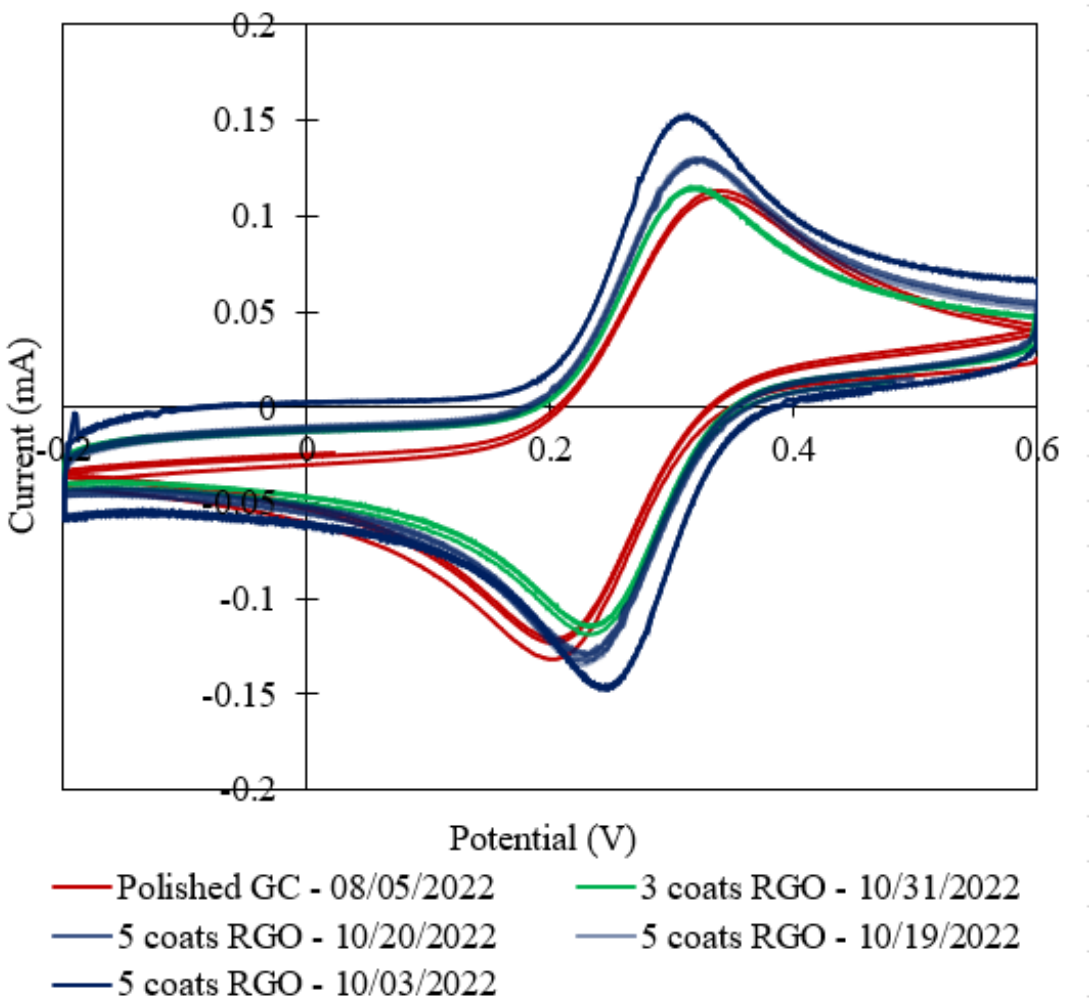

Figure 21. CV results at 200 mV/s for GC0 coated with RGO in a ferricyanide system.

Table 1. Summary of peak-to-peak separation at each scan rate for various RGO samples in the ferricyanide system using GC0 as a substrate. The colours in each column illustrate the relative peak separations, with red indicating the largest separation at a given scan rate and green indicating the smallest separation at a given scan rate.

Date	Working Electrode	Epp (50 mV/s)	Epp (100 mV/s)	Epp (200 mV/s)	Epp (1000 mV/s)	Epp (2000 mV/s)	Average Epp
08/05/2022	Polished GC	0.100	0.115	0.138	0.206	0.244	0.161
01/16/2023	Polished GC	0.153	0.192	0.237	0.343	0.394	0.264
01/20/2023	1 coat RGO	0.075	0.078	0.090	0.112	0.130	0.097
10/31/2022	3 coats RGO	0.069	0.078	0.085	0.123	0.150	0.101
10/03/2022	5 coats RGO	0.077	0.064	0.062	0.076	0.097	0.075
10/19/2022	5 coats RGO	0.071	0.085	0.094	0.137	0.165	0.110
10/20/2022	5 coats RGO	0.079	0.094	0.096	0.132	0.169	0.114

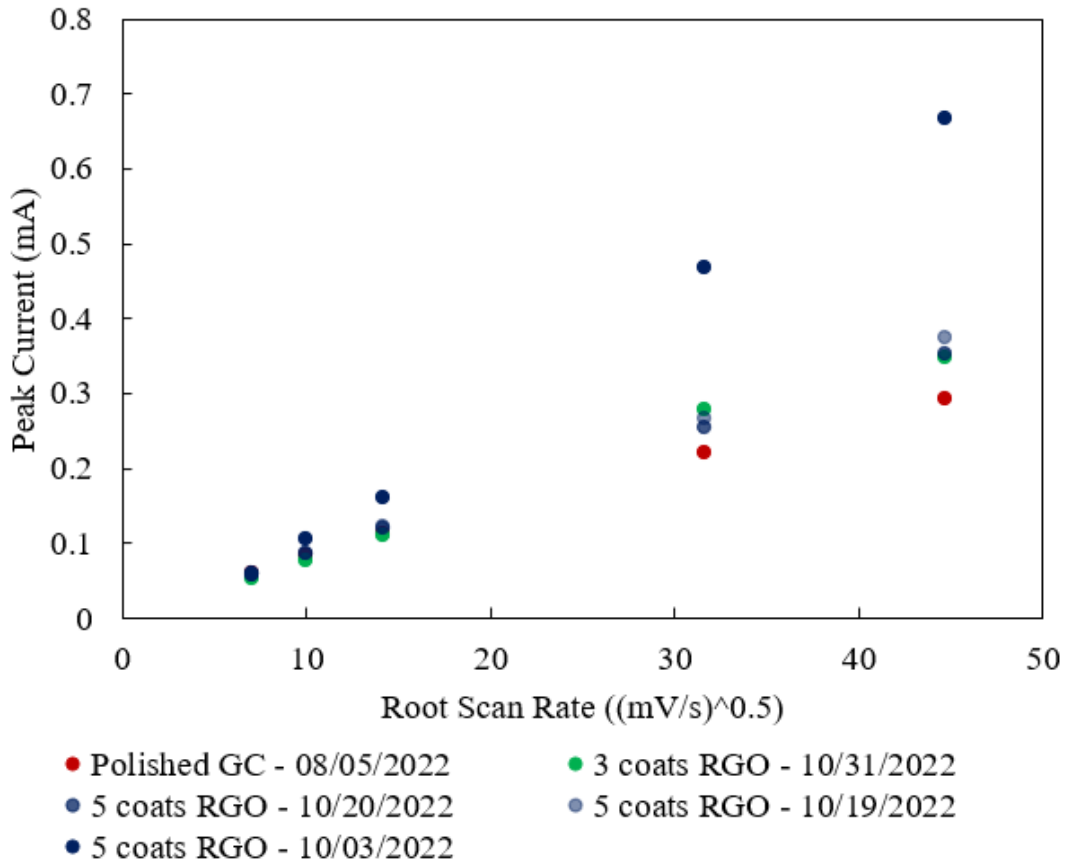

Figure 22. Peak current as a function of the root scan rate for RGO-coated GC0 in a ferricyanide system.

In the switch from the ferricyanide system to the vanadium system (0.1 M $VOSO_4 \cdot xH_2O$ in 3 M H_2SO_4), it was again clear from the CVs (some examples in Figure 23) that distinct differences occur depending on the presence or absence of the nanomaterials. It should be noted that the overlapping sections of some curves on the edges of the graphs are artifacts from the method used to subtract the background scan data from the tests conducted with the vanadium electrolyte. For both GCs used, it can be seen that the addition of RGO

resulted in significant changes to the overall shape of the resulting CV curves. Among these changes is the shift of both the reduction and oxidation peaks toward less overpotential, resulting in reduced peak-to-peak separations. The rise in anodic current is steeper for the coated samples, indicating faster kinetics, likewise for the reverse scans. Additionally, the curves are increasingly symmetrical with the addition of the drop-cast nanomaterial. The asymmetry present in the CV for the polished GC is one of the indicators that the system is not perfectly reversible, as is the shifting peak current at different scan rates, observed in Figure 24.

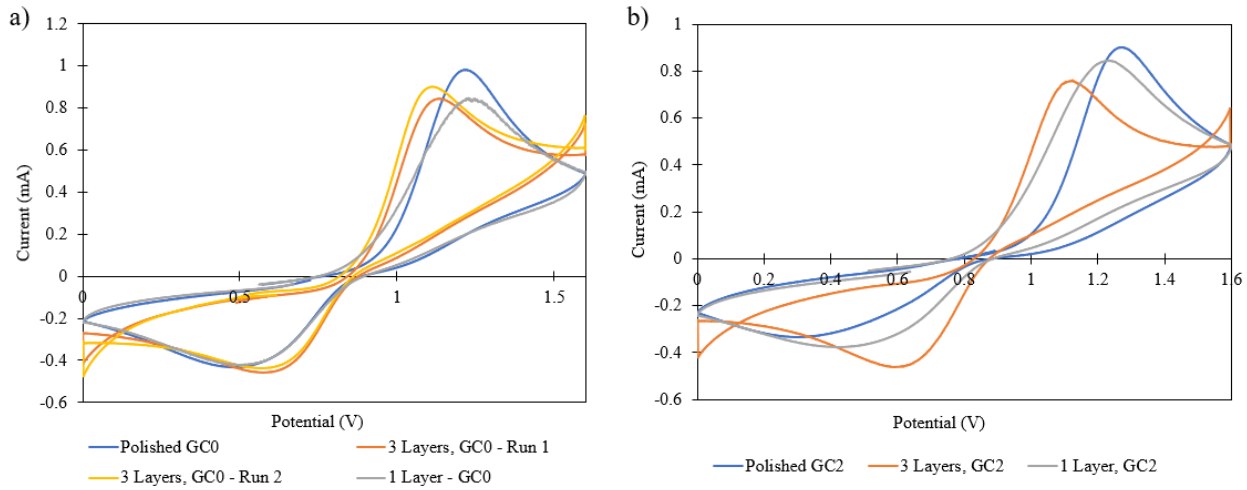

Figure 23. CV results at 20 mV/s for RGO coated on (a) GC0 and (b) GC2 in a vanadium system.

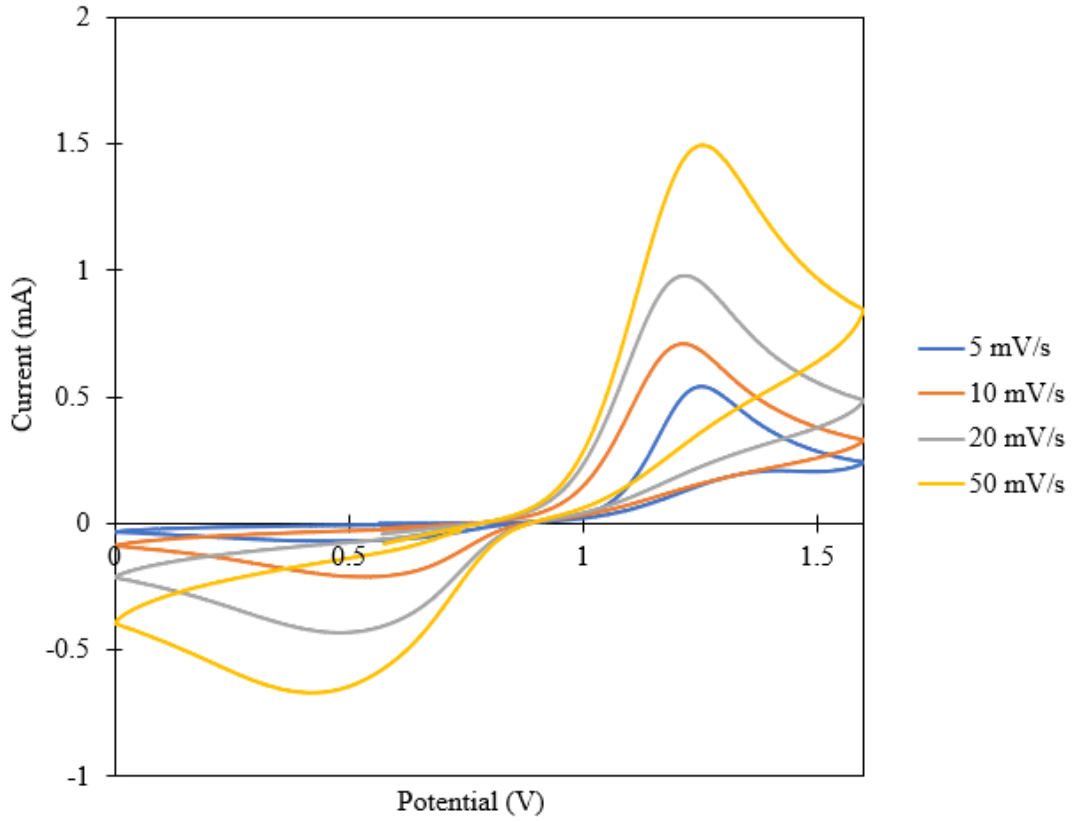

Figure 24. CV results for polished GC0 in a vanadium system.

The graphs resulting from the Punckt porosity factor analysis technique over a scan rate range of 5-50 mV/s can be seen in Figure 25. Note that all the results within this section are segregated based on the glassy carbon plate which was being employed as the substrate for the material deposition. This is because two different GCs were employed, GC0 and GC2, with the first being satisfactorily flat and the second experiencing a level of surface pitting which altered the overall surface area to a degree which rendered the two unacceptable to

compare directly. From these graphs, the proposed trend of decreasing E_{pp} with increasing P does not apply to this system, as the data appear scattered.

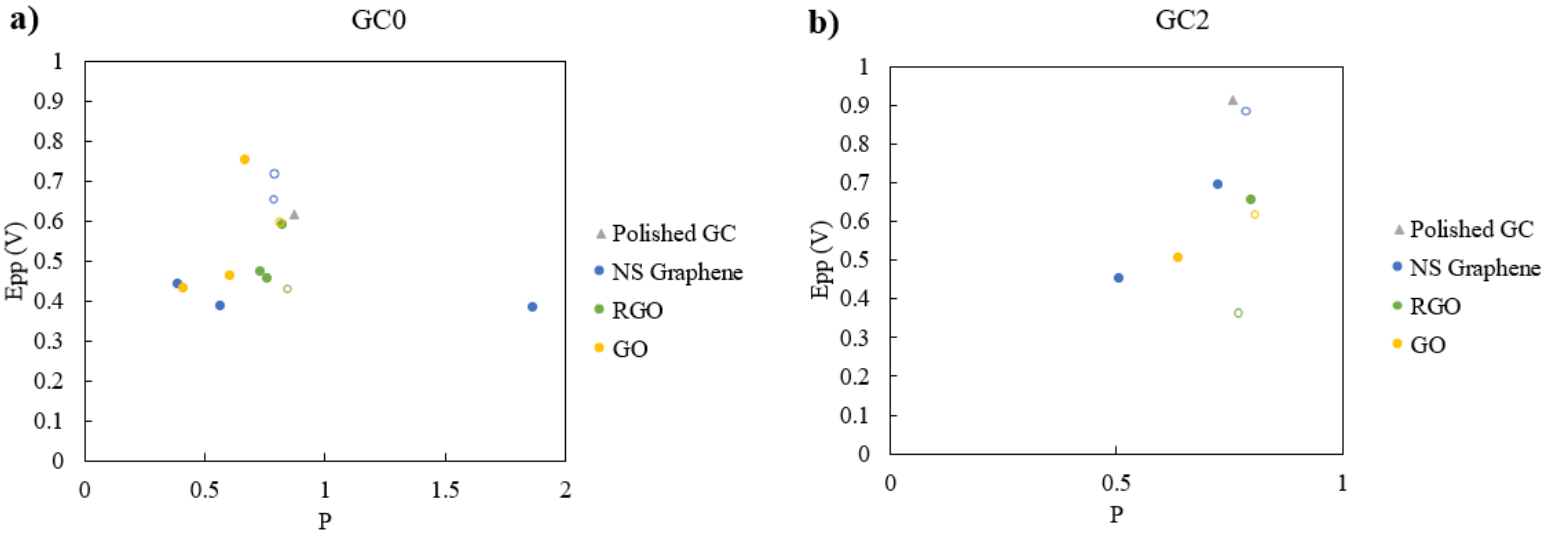

Figure 25. Graphs showing the peak-to-peak separation observed at a scan rate of 10 mV/s as a function of the porosity factor, P, defined by Punckt et.al. Two different GC working electrode substrates were used, (a) GC0 and (b) GC2. Data points which appear as outlines with no fill colour represent tests done with monolayer samples.

The most likely cause for this deviation from the proposed behaviour lies in the nature of the vanadium system which has been observed to perform quasi-reversibly, as opposed to the more reversible ferricyanide system studied in the referenced research. Additionally, it is notable that the feasible range of scan rates for the two systems differ greatly, with the vanadium system only going up to a scan rate of 50 mV/s, equal to the slowest scan rate used in the ferricyanide tests. While the possibility of testing the vanadium system at higher scan rates comparable to those of the ferricyanide system was considered,

this was not found to be possible, with significant errors arising at scan rates above 200 mV/s, causing the tests to stop automatically. This is likely a consequence of the sulfuric acid supporting electrolyte being used in the vanadium system, as no literature appears to apply faster scan rates to any system which includes sulfuric acid. While a clear explanation for this was not readily available, it is potentially a consequence of the high viscosity of the sulfuric acid, though this is simply a theory and has not been explored in detail. To verify that this would not be a feasible course of action for this electrolyte, a few tests were conducted to obtain useable data at higher scan rates. These tests included the removal of the ZIR to circumvent potential feedback issues and the replacement of the platinum wire electrode with a platinum mesh counter electrode to provide a greater surface area. Issues continued to arise beyond 200 mV/s in each case, primarily in the form of current spikes which overloaded the equipment and were clearly outside of the reasonable range. Some of the results from these tests can be seen in Figure 26, below. In these graphs, it can be seen that neither the removal of the ZIR step nor the use of the platinum mesh counter electrode was able to eliminate the prominent current spike at high scan rates. While it was possible to complete most of these runs in the 3 M H_2SO_4, the observed currents in the vanadium electrolyte were consistently much higher than those in the background scans, so these same current spikes, when scaled up for the higher response in the vanadium electrolyte, caused the failure of the system.

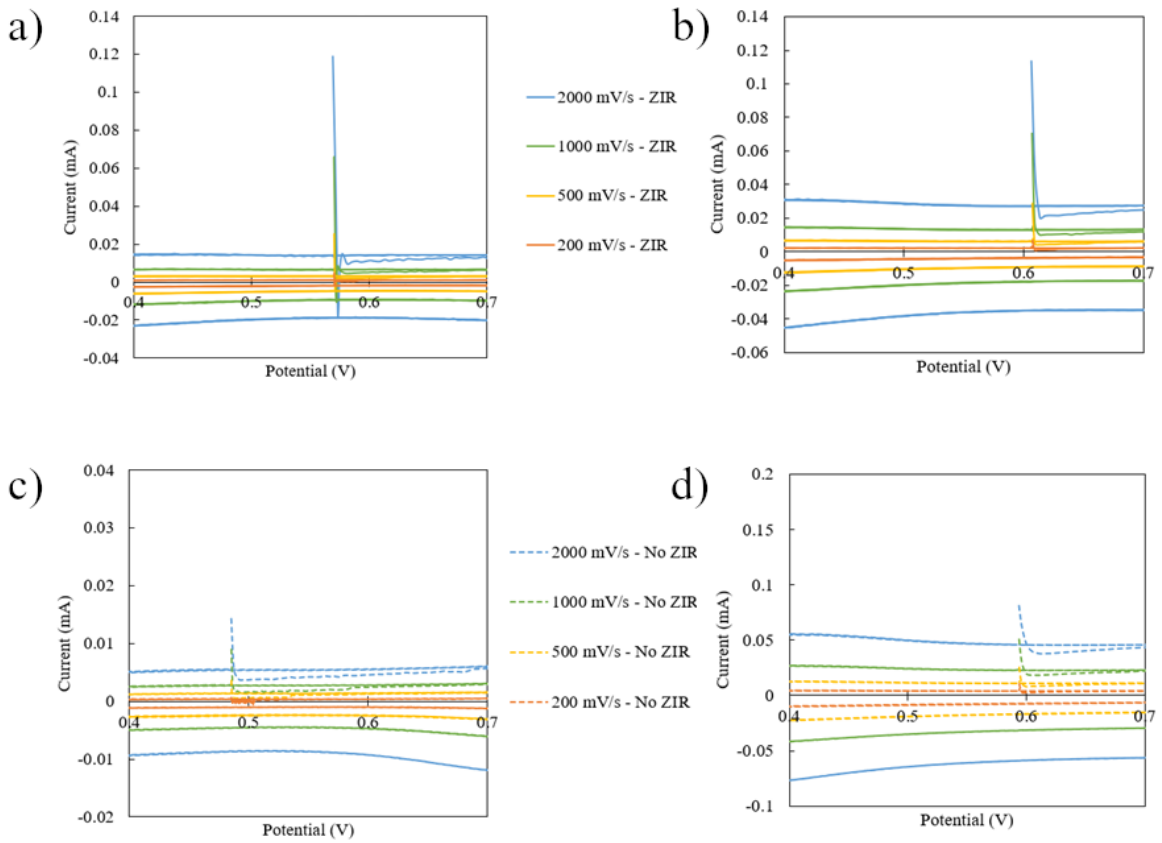

Figure 26. CV results for faster scan rates with modified conditions in sulfuric acid. Graphs (a) and (c) used a platinum mesh counter electrode, while graphs (b) and (d) used platinum wire. The top two graphs are for tests done with the typical ZIR step, while the bottom two graphs excluded this step.

For further comparison of the two systems, the diffusion lengths were calculated according to Equation 12:

$$l = \sqrt{D_p \tau} \tag{12}$$

where l represents the diffusion length, D_p is the diffusion coefficient, and τ is the transition time. The diffusion coefficients of the relevant species in the oxidation reactions for the ferricyanide and vanadium systems are taken as 7.6 x 10^{-5} cm^2/s [2] and 5.68 x 10^{-6} cm^2/s [42], respectively. Both of these values are based on systems in the same solvents as applied in this work. The τ values were calculated times at each different scan rate based on the position of the oxidation peaks in the CVs for polished GC0 samples in each electrolyte. The resulting diffusion lengths can be seen in Figure 27 and Table 2.

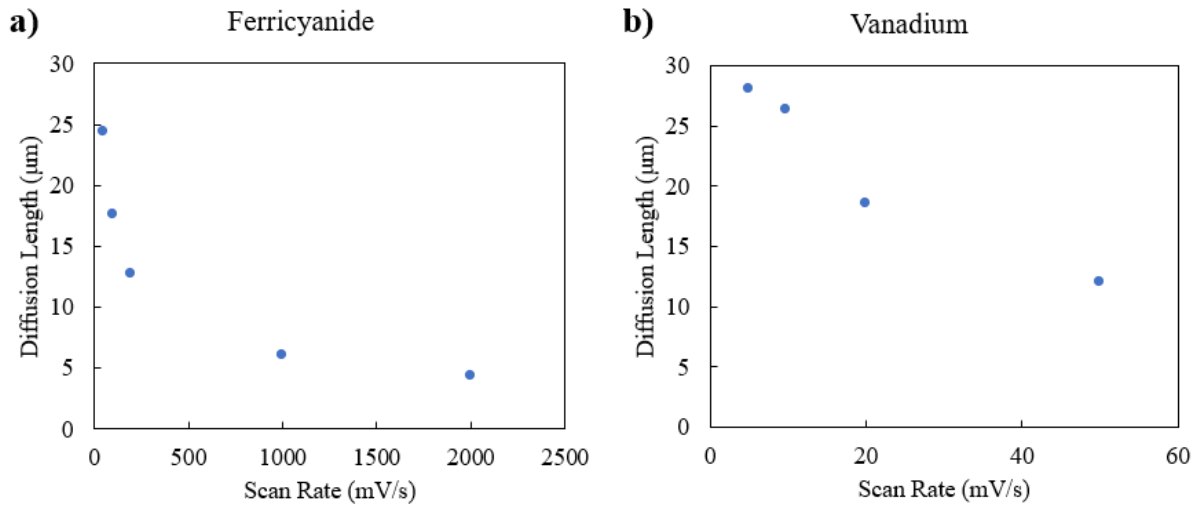

Figure 27. Diffusion length as a function of scan rate for (a) ferricyanide and (b) vanadium systems.

Table 2. Diffusion length as a function of scan rate for ferricyanide and vanadium systems.

Ferricyanide		**Vanadium**	
Scan rate (mV/s)	**Diffusion Length (µm)**	**Scan rate (mV/s)**	**Diffusion Length (µm)**
50	24.4	5	28.01
100	17.6	10	26.3
200	12.75	20	18.61
1000	6.09	50	12.01
2000	4.38		

From this it can be seen that the diffusion length in each case is higher than the expected pore size of the samples (based on the micron-scale thickness observed in AFM images). This shows that the diffusion length cannot be used as the definitive explanation for behavioural differences between the two systems.

3.2.2.2 Monolayer Comparison

Given the problems shown with the implementation of the analysis method described by Punckt et al. in the vanadium system, an alternative method of comparing intrinsic catalytic performance was attempted through the direct comparison of monolayer samples of the different materials, and a compilation of some of the CV data used for this comparison can be seen in Figure 28. Table 3 and Table 4 show the peak-to-peak separation values at each scan rate for the different samples.

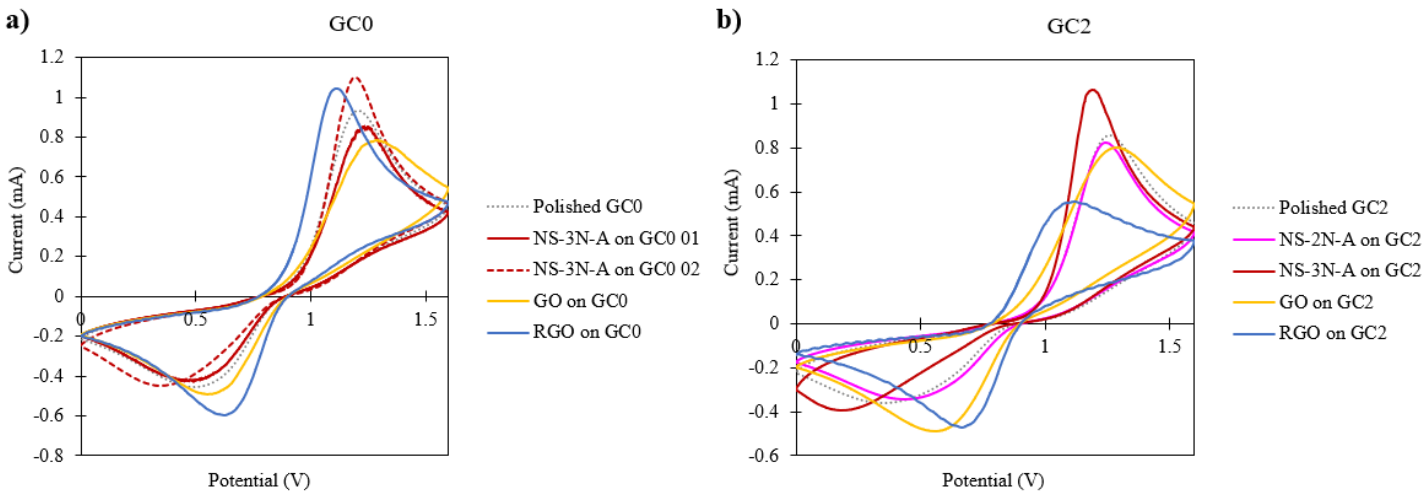

Figure 28. CV results at 20 mV/s for monolayer tests on (a) GC0 and (b) GC2, with NS-3N-A and NS-2N-A referring to NS-graphene from the same batch but different sub-batches.

Table 3. Summary of peak-to-peak separation at each scan rate for the different monolayer samples using GC0 as a substrate. The colours in each column illustrate the relative peak separations, with red indicating the largest separation at a given scan rate and green indicating the smallest separation at a given scan rate.

Working Electrode	**E_{pp} (5 mV/s)**	**E_{pp} (10 mV/s)**	**E_{pp} (20 mV/s)**	**E_{pp} (50 mV/s)**	**Average E_{pp}**
Polished GC0	0.699	0.628	0.723	0.822	0.718
NS-3N-A on GC0 01	0.580	0.617	0.771	0.885	0.713
NS-3N-A on GC0 02	0.516	0.693	0.842	0.977	0.757
GO on GC0	0.586	0.641	0.727	0.863	0.704
RGO onGC0	0.386	0.418	0.489	0.568	0.465

Table 4. Summary of peak-to-peak separation at each scan rate for the different monolayer samples using GC2 as a substrate. The colours in each column illustrate the relative peak separations, with red indicating the largest separation at a given scan rate and green indicating the smallest separation at a given scan rate.

Working Electrode	**E_{pp} (5 mV/s)**	**E_{pp} (10 mV/s)**	**E_{pp} (20 mV/s)**	**E_{pp} (50 mV/s)**	**Average E_{pp}**
Polished GC2	1.057	1.112	0.907	0.928	1.001
NS-3N-A on GC2	0.700	0.875	1.031	1.156	0.940
NS-2N-A on GC2	0.633	0.721	0.802	0.908	0.766
GO on GC2	0.608	0.638	0.728	0.864	0.710
RGO on GC2	0.289	0.362	0.427	0.547	0.406

In this direct comparison of the monolayer samples, a few things are of note. The first is that the RGO sample clearly showed the greatest performance, with the smallest peak-to-peak separation at each scan rate for both GC electrodes. This result could be for several reasons including a potentially higher surface area due to the rougher nature of this material when compared to graphene, as well as the presence of additional functional groups in the RGO which could facilitate the surface reactions. The second thing of note is that for the other materials being compared here, the trends between different substrates, samples, and even scan rates are inconsistent. It is possible that this result could be due to the general variability of the peak-to-peak separation at this level. The small differences observed would be almost negligible since such small changes in performance could render this factor insignificant given that other factors such as cost and ease-of-manufacturing remain quite

different for each of these materials. In the interest of examining the materials from every angle, an alternative approach was attempted following the analysis of these results.

3.2.2.3 Dunn's Method

Noting that the *P* value defined by Punckt et al. assumes a directly proportional relationship between the peak current and square root of the scan rate, it was surmised that a similar analysis may be carried out through the redefinition of the *P* value in such a way that would incorporate the behaviour of a less reversible system. To accomplish this, an analysis technique usually applied for supercapacitor systems, Dunn's Method, is applied. In Dunn's Method, the current response of a system is split into two parts: surface-adsorption (usually referred to as capacitive), and diffusion-limited. The current produced by each of these schemes maintains a relationship to the scan rate being applied; the current depends linearly on scan rate for the surface-adsorption component and linearly on the square root of the scan rate for the diffusion-controlled part. Through this method, the overall current response is defined according to Equation 8, shown in Section 1.1.2. As previously indicated, k_1 and k_2 represent constants which can be used to quantify the contribution of the surface-adsorption and diffusion-limited responses, respectively. These values are obtained for a given scan rate by plotting the linearized version of Equation 8 (both sides divided by the root scan rate) as $i/(v^{0.5})$ *vs* $v^{0.5}$ for each of the tested scan rates at a set potential and taking the slopes of the resulting lines as k_1 and the intercepts as k_2. Based on this equation, it was initially proposed

that a new *P* value may be defined by replacing the original α term with k_2, so the resulting formula (Equation 13) would be:

$$P = \frac{k_2(\nu_{max})}{k_2(\nu_{min})} \tag{13}$$

This could then be plotted in the same way as in the original paper, as shown in Figure 29.

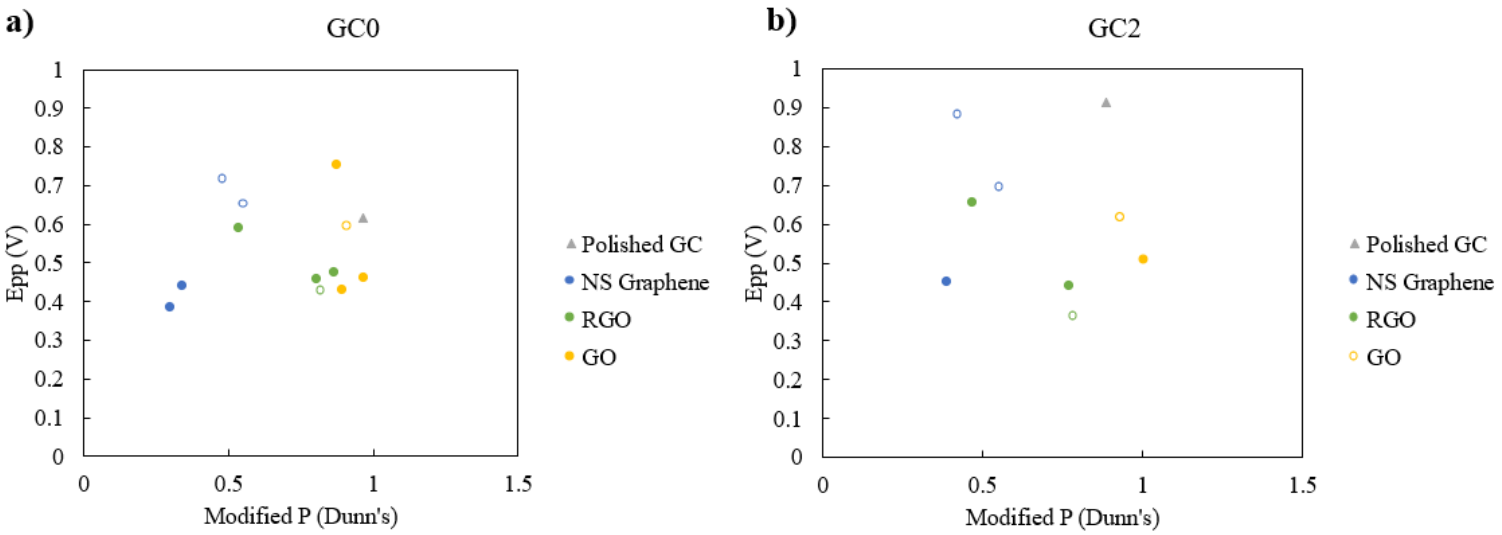

Figure 29. Graphs showing the peak-to-peak separation observed at 10 mV/s as a function of a modified form of the porosity factor, P, originally defined by Punckt et al. and now calculated based on principals described in Dunn's Method. Two different GC working electrode substrates were used, (a) GC0 and (b) GC2. Data points which appear as outlines with no fill colour represent tests done with monolayer samples.

It is evident from these graphs that the theorized trend does not appear here either.

This is explainable by the fact that the mere magnitude of the k_2 value is not indicative of the relative contribution of the diffusion-limited response to the current, as the sum of k_1 and k_2

is not a constant value across all tests. This can be seen more clearly in Figure 30 which shows no clear trend for the calculated k_2 values at each scan rate for all of the NS-graphene samples.

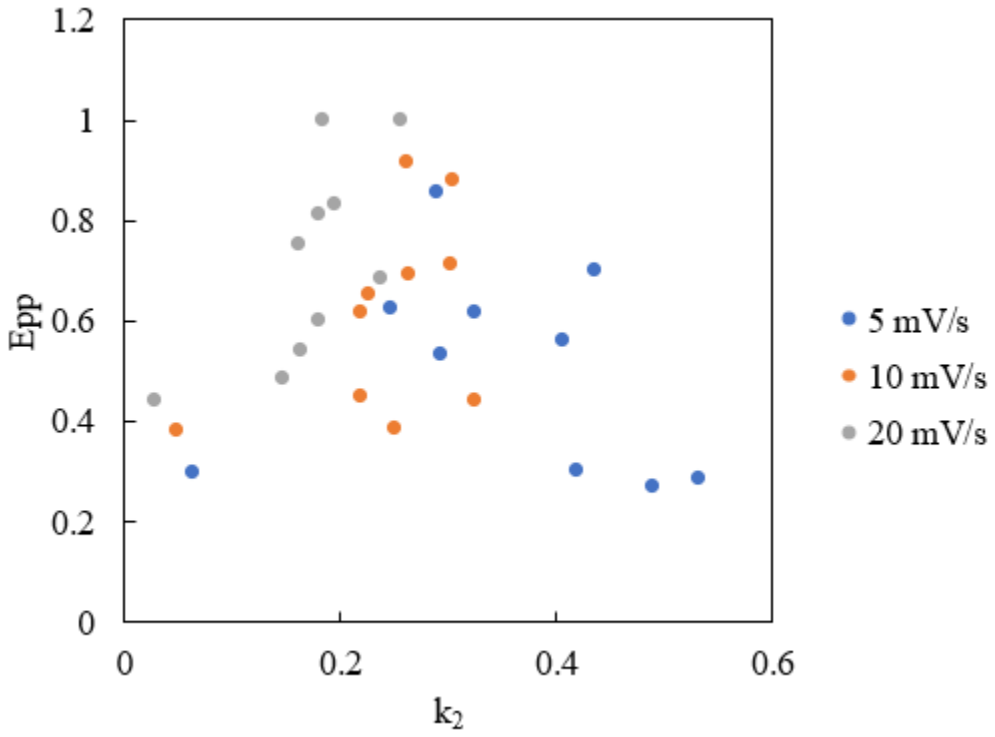

Figure 30. Graph of peak-to-peak separation as a function of the constant k_2 at different scan rates for the graphene-vanadium system.

Thus, the proper way to use the change in relative contributions would require the calculation of these contributions as a percentage of the whole. For this, the diffusion-limited contribution was calculated as follows (Equation 14):

$$diff.(\nu) = \frac{k_2(\nu)*\nu^{\frac{1}{2}}}{k_1(\nu)*\nu+k_2(\nu)*\nu^{\frac{1}{2}}} \quad (14)$$

Finally, this can be used to define a fully modified parameter according to Equation 15:

$$S_D = \frac{diff.(\nu_{max})}{diff.(\nu_{min})} \quad (15)$$

Here, S_D is used in place of *P* as this factor is theorized to depict more of a relative surface area than relative porosity. The subscript corresponds to the name of the analysis method which led to this final definition (Dunn's method). This newly defined term is expected to act similarly to the originally proposed *P*, with the change in the relative diffusion-limited contribution over different scan rates becoming more significant in materials with higher porosity (or effectively higher surface area), since the thickness of the diffusion layer will decrease at higher scan rates, so that for rates at which the diffusion layer thickness is less than the average pore radius, the additional surface area contributed by these pores will become apparent in the diffusion-limited response. When applying this new version of the analysis, however, a problem arises in the fact that the majority (though not all) of the k_1 values obtained are slightly negative, with all k_2 values being positive. This suggests that factors other than surface adsorption reactions exist for which this type of porosity analysis cannot be carried out. The resulting plots (Figure 31) show scattering just as severe as those obtained with the Punckt technique. It is noteworthy that the problem of negative k_1 values exists not just for the samples coated with nanomaterials, but also for the polished GC electrodes. Based on this, it can be seen that the reasons that the various

techniques explored in this chapter have not proven fruitful reside with the vanadium system itself, rather than the ways in which the nanomaterials were introduced into the system.

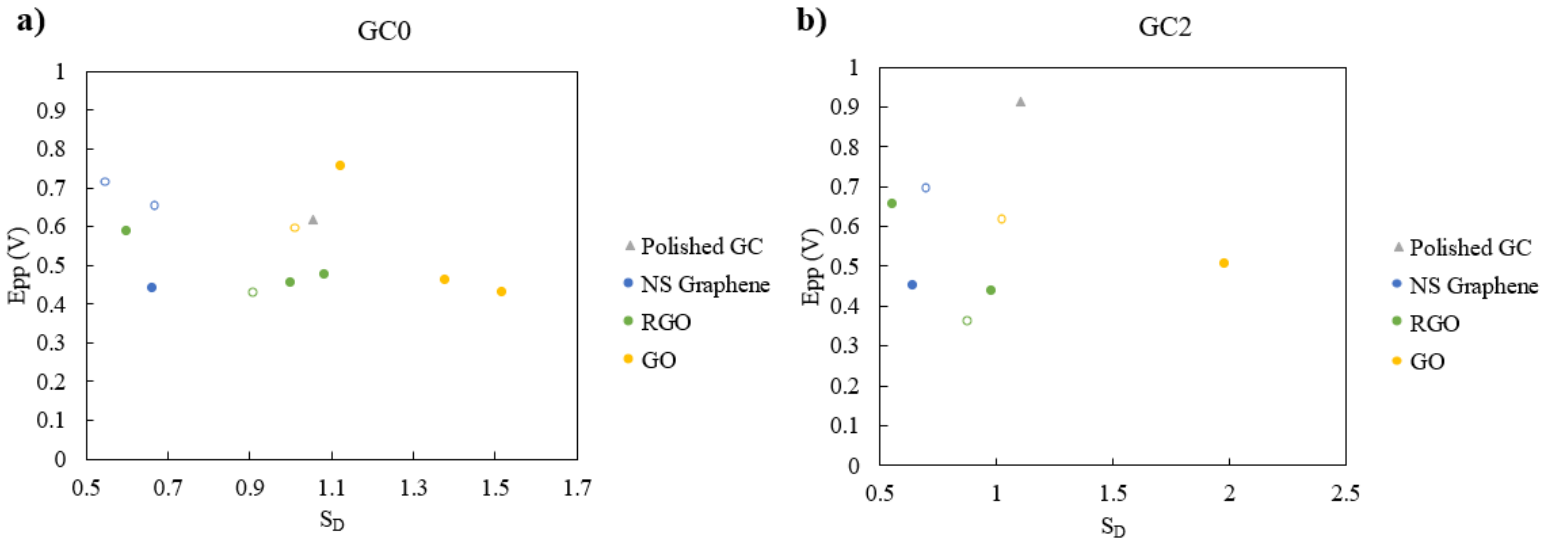

Figure 31. Graphs showing the peak-to-peak separation at 10 mV/s as a function of the newly-defined surface area factor, S_D. Two different GC working electrode substrates were used, (a) GC0 and (b) GC2. Data points which appear as outlines with no fill colour represent tests done with monolayer samples.

3.3 Conclusions and Future Work

Having applied a combination of established, proven, and novel analysis techniques to assess the behaviour of the VRFB system in the presence of different graphene-based nanomaterials, the most reliable result obtained has been the lack of definitive trends observed. In this way, it can be confirmed that the methods described by Punckt et al. cannot be extended simply to quasi-reversible systems. At the same time, a direct comparison of

"monolayer" samples of different materials cannot be used to confidently establish a comparison of each material since the effects of things such as film density and coating roughness continue to convolute the data, although the results are sufficient to conclude that RGO consistently improves cell performance. While the application of the principles described in Dunn's Method provides interesting insight into whether a similar porosity analysis is at all feasible for this system, it provides very little insight beyond what was observed with the Punckt analysis, clarifying only that the problems in the application of these methods remain with the vanadium system itself, rather than the nanomaterials being studied.

The most significant suggestion which must be made for any future work in this area is to develop a more streamlined testing regiment so that a more well-populated dataset may be achieved. It would also be of interest to test a broader range of material loadings in the event that the lack of obvious trends is due to an overly narrow sample window. As with the previous chapter, some initial tests have been started with NP-graphene (not included due to a lack of data at this point), and future work would benefit from the completion of this set of tests. The application of the newly proposed analysis technique could provide interesting results if done with a system which is known to produce normal results when examined using Dunn's Method (i.e. k_1 and k_2 having the same sign). Overall, while it is evident that the addition of nanomaterials such as graphene and RGO to the VRFB system has the potential of improving the overall cell kinetics, more work is required in order to extract intrinsic performance that would allow for the direct comparison of different materials.

References

[1] M. Pahlevaninezhad, E. E. Miller, L. Yang, L. S. Prophet, A. Singh, T. Storwick, M. Pahlevani, M. A. Pope and E. P. L. Roberts, "Exfoliated Graphene Composite Membrane for the All-Vanadium Redox Flow Battery," *ACS Applied Energy Materials,* vol. 6, no. 12, pp. 6505-6517, 06 06 2023.

[2] C. Punckt, M. A. Pope and I. A. Aksay, "On the Electrochemical Response of Porous Functionalized Graphene Electrodes," *The Journal of Physical Chemistry,* vol. 117, pp. 16076-16086, 09 07 2013.

[3] H. Ritchie, P. Rosado and M. Roser, "Fossil Fuels," Our World In Data, 2022. [Online]. Available: https://ourworldindata.org/fossil-fuels. [Accessed 20 07 2023].

[4] S. L. Burch and S. E. Harris, Understanding Climate Change - Science, Policy, and Practice, University of Toronto Press, 2014, pp. 1-307.

[5] K. J. Kim, M.-S. Park, Y.-J. Kim, J. H. Kim, S. X. Dou and M. Skyllas-Kazacos, "A technology review of electrodes and reaction mechanisms in vanadium redox flow batteries," *Journal of Materials Chemistry A,* vol. 3, pp. 16913-16933, 05 06 2015.

[6] Y. K. Zeng, T. S. Zhao, L. An, X. L. Zhou and L. Wei, "A comparative study of all-vanadium and iron-chromium redox flow batteries for large-scale energy storage," *Journal of Power Sources,* vol. 300, pp. 438-443, 30 12 2015.

[7] M. Pahlevaninezhad, M. Pahlevani and E. P. L. Roberts, "Effects of aluminum, iron, and manganese sulfate impurities on the vanadium redox flow battery," *Journal of Power Sources,* vol. 529, p. 231271, 01 05 2022.

[8] Y. Ahn and D. Kim, "Ultra-low vanadium ion permeable electrolyte membrane for vanadium redox flow battery by pore filling of PTFE substrate," *Energy Storage Materials,* vol. 31, pp. 105-114, 10 2020.

[9] E. M. Stuve, "Overpotentials in Electrochemical Cells," in *Encyclopedia of Applied Electrochemistry*, G. Kreysa, K. Ota and R. F. Savinell, Eds., Springer Reference, 2014, pp. 1445-1453.

[10] M. Vijayakumar, M. S. Bhuvaneswari, P. Nachimuthu, B. Schwenzer, S. Kim, Z. Yang, J. Liu, G. L. Graff, S. Thevuthasan and J. Hu, "Spectroscopic investigations of the fouling process on Nafion membranes in vanadium redox flow batteries," *Journal of Membrane Science,* vol. 366, no. 1-2, pp. 325-334, 01 2011.

[11] H. Yamada, K. Yoshii, M. Asahi, M. Chiku and Y. Kitazumi, "Cyclic Voltammetry Part 1: Fundamentals," *J-Stage,* vol. 90, no. 10, p. 102005, 2022.

[12] D. Yan, M. Z. Bazant, P. M. Biesheuvel, M. C. Pugh and F. P. Dawson, "Theory of linear sweep voltammetry with diffuse charge: Unsupported electrolytes, thin films, and leaky membranes," *Physical Review E,* vol. 95, no. 3, p. 033303, 08 03 2017.

[13] N. Elgrishi, K. J. Rountree, B. D. McCarthy, E. S. Rountree, T. T. Eisenhart and J. L. Dempsey, "A Practical Beginner's Guide to Cyclic Voltammetry," *Journal of Chemical Education,* vol. 95, no. 2, pp. 197-206, 3 11 2017.

[14] A. J. Bard and L. R. Faulkner, Electrochemical Methods - Fundamentals and Applications, 2 ed., New York: John Wiley & Sons Inc., 2001, pp. 1-833.

[15] M. Bodik, M. Jergel, E. Majkova and P. Siffalovic, "Langmuir films of low-dimensional nanomaterials," *Advances in Colloid and Interface Science,* vol. 283, p. 102239, 09 2020.

[16] Y. Zhang, L. Xu, W. R. Walker, C. M. Tittle, C. J. Backhouse and M. A. Pope, "Langmuir films and uniform, large area, transparent coatings of chemically exfoliated MoS2 single layers," *Journal of Materials Chemistry C,* vol. 5, no. 43, pp. 11275-11287, 17 07 2017.

[17] X. Lou, D. Yan, Y. Yu, Y. Lei, M. Ding, Q. Sun and C. Jia, "Cost-effective Nafion Composite Membrane as an Effective Vanadium-Ion Barrier for Vanadium Redox Flow Batteries," *Chemistry: An Asian Journal,* vol. 15, no. 15, pp. 2357-2363, 13 03 2020.

[18] F. Fang, L. Liu, L. Min, L. Xu, W. Zhang and Y. Wang, "Enhanced proton conductivity of Nafion membrane with electrically aligned sulfonated graphene nanoplates," *International Journal of Hydrogen Energy,* vol. 46, no. 34, pp. 17784-17792, 17 05 2021.

[19] J. Xi, Z. Wu, X. Qiu and L. Chen, "Nafion/SiO2 hybrid membrane for vanadium redox flow battery," *Journal of Power Sources,* vol. 166, no. 2, pp. 531-536, 15 04 2007.

[20] X. Teng, Y. Zhao, J. Xi, Z. Wu, X. Qiu and L. Chen, "Nafion/organic silica modified TiO2 composite membrane for vanadium redox flow battery via in situ sol–gel reactions," *Journal of Membrane Science,* vol. 341, no. 1-2, pp. 149-154, 30 09 2009.

[21] P. M. Nia, E. Abouzari-Lotf, P. M. Woi, Y. Alias, T. M. Ting, A. Ahmad and N. W. C. Jusoh, "Electrodeposited reduced graphene oxide as a highly efficient and low-cost electrocatalyst for vanadium redox flow batteries," *Electrochimica Acta,* vol. 297, pp. 31-39, 19 02 2019.

[22] M. Park, Y.-j. Jung, J. Kim, H. i. Lee and J. Cho, "Synergistic Effect of Carbon Nanofiber/Nanotube Composite Catalyst on Carbon Felt Electrode for High-Performance All-Vanadium Redox Flow Battery," *Nano Letters,* vol. 13, no. 10, pp. 4833-4839, 11 09 2013.

[23] M. Miao, M. B. Nardelli, Q. Wang and Y. Liu, "First principles study of the permeability of graphene to hydrogen atoms," *Physical Chemistry Chemical Physics*, vol. 15, no. 38, pp. 16132 - 16137, 14 10 2013.

[24] L. Xu, A. R. Tetreault, H. H. Khaligh, I. A. Goldthorpe, S. D. Wettig and M. A. Pope, "Continuous Langmuir−Blodgett Deposition and Transfer by Controlled Edge-to-Edge Assembly of Floating 2D Materials," *Langmuir*, vol. 35, no. 1, pp. 51-59, 12 12 2018.

[25] L. Yu, F. Lin, L. Xu and J. Xi, "A recast Nafion/graphene oxide composite membrane for advanced vanadium redox flow batteries," *RSC Advances*, no. 5, pp. 3756-3763, 23 12 2015.

[26] B. Jiang, L. Wu, L. Yu, X. Qiu and J. Xi, "A comparative study of Nafion series membranes for vanadium redox flow batteries," *Journal of Membrane Science*, vol. 510, pp. 18-26, 15 07 2016.

[27] G.-J. Hwang and H. Ohya, "Preparation of cation exchange membrane as a separator for the all-vanadium redox flow battery," *Journal of Membrane Science*, vol. 120, no. 1, pp. 55-67, 30 10 1996.

[28] S. Peng, X. Yan, X. Wu, D. Zhang, Y. Luo, L. Su and G. He, "Thin skinned asymmetric polybenzimidazole membranes with readily tunable morphologies for high-performance vanadium flow batteries," *RSC Advances*, no. 4, 12 01 2017.

[29] L. Su, D. Zhang, S. Peng, X. Wu, Y. Luo and G. He, "Orientated graphene oxide/Nafion ultra-thin layer coated composite membranes for vanadium redox flow battery," *International Journal of Hydrogen Energy,* vol. 42, no. 34, pp. 21806-21816, 24 08 2017.

[30] D. Zhang, Q. Wang, S. Peng, X. Yan, X. Wu and G. He, "An interface-strengthened cross-linked graphene oxide/Nafion212 composite membrane for vanadium flow batteries," *Journal of Membrane Science,* vol. 587, p. 117189, 01 10 2019.

[31] T. Wang, S. J. Moon, D.-S. Hwang, H. Park, J. Lee, S. Kim, Y. M. Lee and S. Kim, "Selective ion transport for a vanadium redox flow battery (VRFB) in nano-crack regulated proton exchange membranes," *Journal of Membrane Science,* vol. 583, pp. 16-22, 01 08 2019.

[32] Q. Dai, Z. Liu, L. Huang, C. Wang, Y. Zhao, Q. Fu, A. Zheng, H. Zhang and X. Li, "Thin-film composite membrane breaking the trade-off between conductivity and selectivity for a flow battery," *Nature Communications,* vol. 11, no. 13, 07 01 2020.

[33] T. Wang, J. Han, K. Kim, A. Münchinger, Y. Gao, A. Farchi, Y.-K. Choe, K.-D. Kreuer, C. Bae and S. Kim, "Suppressing vanadium crossover using sulfonated aromatic ion exchange membranes for high performance flow batteries," *Materials Advances,* vol. 1, no. 7, pp. 2206-2218, 01 09 2020.

[34] B. G. Thiam and S. Vaudreuil, "Review—Recent Membranes for Vanadium Redox Flow Batteries," *Journal of The Electrochemical Society*, vol. 168, no. 7, p. 070553, 28 07 2021.

[35] D. Reed, E. Thomsen, W. Wang, Z. Nie, B. Li, X. Wei, B. Koeppel and V. Sprenkle, "Performance of Nafion® N115, Nafion® NR-212, and Nafion® NR-211 in a 1 kW class all vanadium mixed acid redox flow battery," *Journal of Power Sources*, vol. 285, pp. 425-430, 01 07 2015.

[36] A. K. Singh, M. Pahlevaninezhad, N. Yasri and E. P. L. Roberts, "Degradation of Carbon Electrodes in the All-Vanadium Redox Flow Battery," *ChemSusChem*, vol. 14, no. 9, pp. 2100-2111, 19 03 2021.

[37] W. Dai, Y. Shen, Z. Li, L. Yu, J. Xi and X. Qiu, "SPEEK/Graphene oxide nanocomposite membranes with superior cyclability for highly efficient vanadium redox flow battery," *Journal of Materials Chemistry A*, vol. 2, no. 31, pp. 12423-12432, 06 06 2014.

[38] S. Hu, M. Lozoda-Hidalgo, F. C. Wang, A. Mishchenko, F. Schedin, R. R. Nair, E. W. Hill, D. W. Boukhvalov, M. I. Katsnelson, R. A. W. Dryfe, I. V. Grigorieva, H. A. Wu and A. K. Geim, "Proton transport through one-atom-thick crystals," *Nature*, vol. 516, pp. 227-230, 26 11 2014.

[39] K. J. Lee and Y. H. Chu, "Preparation of the graphene oxide (GO)/Nafion composite membrane for the vanadium redox flow battery (VRB) system," *Vacuum,* vol. 107, pp. 269-276, 09 2014.

[40] Z. Mai, H. Zhang, X. Li, S. Xiao and H. Zhang, "Nafion/polyvinylidene fluoride blend membranes with improved ion selectivity for vanadium redox flow battery application," *Journal of Power Sources,* vol. 196, no. 13, pp. 5737-5741, 1 07 2011.

[41] D. C. Marcano, D. V. Kosynkin, J. M. Berlin, A. Sinitskii, Z. Sun, A. Slesarev, L. B. Alemany, W. Lu and J. M. Tour, "Improved Synthesis of Graphene Oxide," *ACS Nano,* vol. 4, no. 8, pp. 4806-4814, 22 07 2010.

[42] W. Wang, X. Fan, J. Liu, C. Yan and C. Zeng, "Temperature-related reaction kinetics of the vanadium(iv)/(v) redox couple in acidic solutions," *RSC Advances,* vol. 4, no. 61, p. 32405, 2014.

Appendix

The following is the entirety of the published work co-authored by the author of this report, which was in some parts copied directly into the final thesis manuscript. This is acknowledged and cited at the beginning of the relevant chapters.

ACS APPLIED ENERGY MATERIALS

www.acsaem.org Article

Exfoliated Graphene Composite Membrane for the All-Vanadium Redox Flow Battery

Maedeh Pahlevaninezhad, Elizabeth Esther Miller, Lixin Yang, Lauren Sarah Prophet, Ashutosh Singh, Thomas Storwick, Majid Pahlevani, Michael A. Pope, and Edward P. L. Roberts*

Cite This: *ACS Appl. Energy Mater.* 2023, 6, 6505−6517 Read Online

ACCESS | Metrics & More | Article Recommendations | Supporting Information

ABSTRACT: Vanadium redox flow batteries are emerging as a promising grid storage solution. Unlike competing flow battery concepts, these utilize vanadium in both the catholyte and anolyte chambers which enables easy regeneration and balancing of the cell upon crossover of species through the membrane during long-term use. To increase the time between regeneration cycles and to improve the overall efficiency of vanadium flow batteries, we investigate the use of an ultrathin, graphene coating on the surface of various Nafion membranes. Electrochemically exfoliated graphene (EEG) was dispersed at the air−water interface of a Langmuir−Blodgett trough, compressed, and transferred to Nafion 117 (180 μm thickness) and Nafion 115 (127 μm) membranes. Single-cell vanadium redox flow batteries assembled with the coated membranes led to significantly higher energy efficiency (increased by 13%), power density (by 67%), and discharge capacity (by 17.5%) over 100 cycles compared to uncoated Nafion. The graphene layer was stable over cycling, and electrochemical impedance spectroscopy and self-discharge experiments indicated that the improved battery performance is due to a combination of reduced vanadium crossover and enhanced electrochemical activity provided by the graphene at the electrode surface.

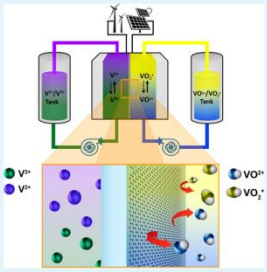

KEYWORDS: *energy storage, exfoliated graphene, graphene composite membrane, vanadium redox flow battery, Nafion membrane*

1. INTRODUCTION

Although fossil fuel energy is still the largest energy source utilized globally, renewable energy use is growing rapidly and is expected to reach the same level by 2050.[1] Energy storage systems (ESSs) for intermittent renewable energy are becoming more important and urgent to fulfill the future demand.[2−5] Redox flow batteries (RFBs) can store electrical energy at a large scale for these applications.[6,7] Due to their long lifetime, independent power and energy, high round trip efficiency, scalability, and design flexibility, RFBs are a good candidate for large-scale energy storage.[2,8] The vanadium redox flow battery (VRFB) is currently the state-of-the-art RFB technology due to its use of a single element (vanadium) with different oxidation states on both sides of the battery, avoiding problems with cross-contamination in the system.[5] The membrane is a crucial component of VRFBs that allows transport of ions during cycling while separating the two half-cell electrolytes. It can significantly affect the battery performance, lifetime, and cost. The ideal membrane for VRFBs should exhibit high mechanical and chemical stability, high proton conductivity, low vanadium permeability, and low cost.[4,5,9] The most widely used membranes in VRFBs are perfluorinated sulfonic acid membranes such as Nafion. These membranes have high proton conductivity while maintaining chemical and mechanical stability, but suffer from high cost and vanadium ion permeability because of the presence of large channels of ion clusters.[5,10−12] Vanadium transport through the membrane during cycling leads to self-discharge and capacity fade in the battery.[12] Alternative, nonperfluorinated sulfonic acid membranes[13−23] such as sulfonated poly(ether ether ketone) (SPEEK), sulfonated poly imide (SPI), sulfonated poly ether sulfone (SPES), and polybenzimidazole (PBI), have been investigated to reduce vanadium crossover. The nonperfluorinated membranes exhibit lower vanadium permeability and cost compared to Nafion. However, they are susceptible to degradation under strong acidic electrolyte conditions, resulting in a short cycle life.[14,17] An alternative approach is to modify Nafion to improve the ion selectivity and enable the use of thinner, lower-cost membranes. Approaches studied so far include doping Nafion with inorganic materials (e.g., TiO_2, SiO_2, WO_3),[24−26] surface modification,[27,28] applying polymer layers,[19,20,29] pretreatment of the membrane, and tuning the membrane thickness.[12,30] Among these methods, surface modification has the potential to preserve the same chemical

Received: February 15, 2023
Accepted: May 18, 2023
Published: June 6, 2023

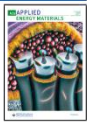

and mechanical stability of the membrane while reducing vanadium ion permeability.[31,32]

A wide variety of carbon materials have been used as VRFB electrode with porous structures.[33] However, these materials have rarely been used as a conformal film in VRFB membranes. Several studies have used graphene oxide (GO) in composite membranes including GO/Nafion,[10,11,34,35] GO/PVDF,[36] and GO/PES.[37] These composite membranes have been shown to decrease the vanadium permeation by blocking the ionic transport pathway while still facilitating proton conduction. Most GO/Nafion composite membranes were prepared by mixing the GO with a Nafion solution and casting the membrane.[10,11,34] These studies of GO/Nafion composite membranes demonstrated improved VRFB energy efficiency from 3 to 12%. The highest improvement in VRFB energy efficiency (9−12%) using recast GO/Nafion membranes was obtained by Su et al.,[34] who oriented the GO parallel to the membrane surface to maximize the effect of the two-dimensional (2D) nanofiller. They found that the vanadium permeability of the composite membrane was 2 orders of magnitude lower than the pristine membrane. Zhang et al.[35] showed that a layer of GO coated on Nafion 212 acts as a barrier for vanadium crossover and obtained increases in the energy efficiency of up to 22%.

In this study, instead of forming a composite, we deposit single to few-layer flakes of electrochemically exfoliated graphene (EEG) onto commercial ion exchange membranes. This enhances the VRFB performance without requiring modification of battery design or operating conditions and leverages existing, commercial membrane sheets. This is the first time that an electrically conducting film has been used to modify a membrane which has the potential to not only block vanadium crossover but also enhance the electrochemical activity close to the membrane surface where the overpotential is expected to be highest. Since VRFBs currently use these membrane materials along with carbon or graphite electrodes, the EEG-coated membrane is fully compatible with commercial VRFB technology.

Large-area (~7.6 × 7.6 cm^2) coatings of EEG were deposited on the Nafion membranes using a modified Langmuir−Blodgett (LB) technique where the EEG was dispersed onto the air−water interface, and the floating film was compressed and transferred to the Nafion by the horizontal precipitation method. We recently demonstrated that this method can be adapted to a continuous roll-to-roll transfer system which could be used to coat arbitrary lengths of Nafion in the future.[38] The EEG was prepared by a two-step method that provides mostly one- and two-layer graphene with a relatively low oxygen content, using a method recently reported by us.[39] The properties of the EEG-coated Nafion such as water uptake, swelling ratio, ion exchange capacity, area resistance, proton conductivity, and vanadium permeability were determined and compared with those of uncoated Nafion. VRFB performance and capacity retention were found to increase significantly due to the EEG coating.

2. EXPERIMENTAL SECTION

2.1. Materials. Graphite exfoliation was conducted in a two-electrode system using stainless steel as the counter electrode and a flexible graphite foil (GraphiteStore, INTRS-GSSM316) as the working electrode. Potassium hydroxide (KOH, MilliporeSigma) and ammonium sulfate ($(NH_4)_2SO_4$, MilliporeSigma) were used as the exfoliation electrolyte for each step. *N*,*N*-Dimethylformamide (DMF, MilliporeSigma), 1,2-dichloroethane (DCE, MilliporeSigma), and ethanol (reagent alcohol grade, MilliporeSigma) were used to disperse the EEG and spread the dispersion onto the air−water interface. An aqueous solution containing 1.6 M vanadium oxysulfate ($VOSO_4$, 99.5% purity, NOAH Technologies) dissolved in 3 M sulfuric acid (H_2SO_4 MilliporeSigma), prepared in deionized (DI) water (>18.2 MΩ cm), was used as the VRFB electrolyte in all experiments. Magnesium sulfate ($MgSO_4$, MilliporeSigma) was used for vanadium permeability experiments. Carbon paper (Sigracet 39AA, 280 μm thickness, pore size 43 μm, Ion Power) was used as an electrode material, and the bare membrane materials were Nafion 117 and 115 membranes (thickness of 180 and 127 μm, respectively, Ion Power).

2.2. Graphene Synthesis. A two-step electrochemical exfoliation process was used to prepare graphene nanoplatelets, following the procedure described by Roberts and Singh.[39] A two-electrode cell was used to synthesize hydroxide intercalated graphite (graphite intercalation compound, GIC) with a graphite foil anode and stainless-steel cathode in a potassium hydroxide electrolyte at a concentration of 16 M and a current density of 30 mA cm^{-2} for 18 min. The high concentration of hydroxide minimizes the size of the hydration sphere and enables effective intercalation of hydroxide ions. The increasing cell voltage was monitored until it reached 2.6 V, after which the applied voltage was held at 2.6 V for 10 min to allow the graphite electrode to be fully intercalated.[39] Following the intercalation process, the GIC obtained was immediately transferred to a second two-electrode cell for electrochemical exfoliation. The exfoliation was performed according to the procedures reported by Cao et al.[40] and Momodu et al.[41] using a 0.1 M $(NH_4)_2SO_4$ electrolyte, with the GIC anode, and a 316L stainless steel cathode. It was found that the hydroxide GIC was unstable and would de-intercalate very easily when exposed to the exfoliation solution. To avoid de-intercalation, the GIC was slowly taken out of 16 M KOH solution while the cell voltage was increased to 10 V, and the GIC was immediately transferred into the 0.1 M $(NH_4)_2SO_4$ exfoliation solution.

A constant cell voltage of 10 V was applied until complete GIC electrode exfoliation was achieved. The exfoliated product was filtered and washed thoroughly using deionized water to remove any residual ionic species from the exfoliation process. To redisperse graphene flakes, the exfoliated product was added to deionized (DI) water, sonicated for 5 to 6 min using a bath sonicator, and then centrifuged (Sorvall Legend X1R, Thermo Scientific, Germany) at 2000 RPM for 10 min. The suspended graphene flakes were decanted, while the separated solids were redispersed for 5−6 min in DI water by sonication to recover further graphene and centrifuged again. To ensure maximum recovery of graphene flakes from un-exfoliated graphitic particles, centrifugation was repeated up to five times. The final graphene−water suspension obtained after centrifugation was combined and vacuum-filtered to obtain a film of EEG.

2.3. Graphene Composite Membrane Preparation. Following the graphene synthesis process, approximately 20 mg of the obtained graphene film was dispersed in 15 mL of DMF in a 20 mL capacity scintillation vial.[38] The mixture was probe-ultrasonicated (60% amplitude, Model 150VT Ultrasonic Homogenizer, BioLogics, Inc.; Sonics Vibra-Cell VCX-500 Ultrasonic Processor, Sonics & Materials, Inc.) for 2 h under stirring and in an ice bath to prevent overheating. The mixture was then transferred into a centrifuge tube and centrifuged (AccuSpinTM 3, Fisher Scientific, Waltham, MA) at 3600 RPM for 30 min. Prior to film deposition, the concentrations of the graphene dispersion were estimated by ultraviolet/visible (UV−vis) spectroscopy (UV-Vis, Thermo Scientific Evolution 300). UV−vis spectra from 300 to 800 nm were obtained for graphene-DMF dispersions, diluted with DMF as necessary. The stock concentrations were calculated according to Beer−Lambert's law using an absorptivity of α = 44.44 mL mg^{-1} cm^{-1} for absorbances at 660 nm, as determined by Ojrzynska et al.[42] This absorption coefficient is suitable for graphene dispersions with an approximate flake size of 2 μm. Immediately prior to deposition onto the air−water interface, an appropriate volume of this dispersion (from 250 to 500 μL depending

https://doi.org/10.1021/acsaem.3c00428
ACS Appl. Energy Mater. 2023, 6, 6505−6517

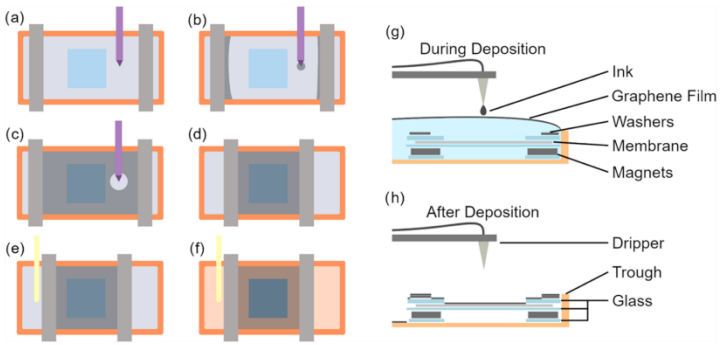

Figure 1. Schematic illustration of the deposition process from the top (a–f) and side (g, h). (a) The glass-supported Nafion membrane is placed in the center of the trough with barriers on opposite ends and water is added (the membrane is represented by the small blue square in the center). (b) The graphene ink is dripped onto the surface such that a film begins to form at either end of the trough. (c) Ink drops are added until the solvent from the previous droplet does not have enough time to fully dissipate before the next droplet falls. (d) The film is compressed by moving the Teflon barriers toward the center of the trough. (e) Vacuum (pictured to the left of the leftmost barrier) is used to remove the water from the outside of one of the barriers where there is no graphene film. (f) Water level drops below the level of the membrane and the graphene film is lowered onto its surface, completing the coating process. (g) Side view of the setup during deposition. (h) Side view of the setup after deposition.

on the spreading behavior of the graphene sample) was added to DCE corresponding to a 3:1 DCE/DMF volumetric ratio. The DCE assists in effectively spreading the dispersion on the air–water interface.[38]

The Nafion membranes were coated according to a modified LB deposition process.[38] At least 24 h prior to coating, the membranes were soaked in DI water to ensure they were fully swollen with water. The membranes were then secured to a glass substrate, which had been cleaned with DCE and rinsed with DI water, by placing the membrane corners between the glass plate and 2 cm squares of glass with N52 neodymium magnets (McMaster-Carr) below the glass plate and metal washers on top of the glass squares (see Figure S1). The magnets and washers were cleaned with ethanol prior to use. The secured membrane was placed face up in an 8 cm wide Teflon deposition trough, the design of which was based on a commercial trough (Langmuir Trough G1, Kibron). Sections of the trough were divided using Teflon barriers, as depicted in Figure S2, with the membrane setup in the center of the trough. DI water was added until just before the point of spillover such that the membrane setup was completely covered, and a significant meniscus was observed. For characterization purposes, additional substrates such as mica and silicon wafers (SPI Supplies; University Wafer, Inc.) were often included in the trough as well. The surface of the water was cleaned using a vacuum aspirator until the compressed surface pressure change was found to be negligible to ensure that there was no remaining surface debris.

The coating process is illustrated in Figure 1. The graphene/DMF/DCE ink was transferred into a glass syringe with an inner diameter of 14.6 mm connected to poly(tetrafluoroethylene) (PTFE) tube attachment with an inner diameter of 0.33 mm. The end of the PTFE tube was lowered toward the surface of the water to a height at which the ink droplets would hit the surface immediately after falling from the tube, and the ink was deposited onto the surface of the water at a rate of 0.1 mL min^{-1}. The dripping was continued until enough surface area was covered with a semitransparent film of graphene such that the solvent from the previous droplet did not have enough time to fully dissipate before the next droplet falls (usually this corresponds to an uncoated circular area with a diameter of approximately 3 cm). The film was subsequently compressed to a surface pressure of approximately 20 mN m^{-1} at a rate of 5 mm min^{-1}, as measured with a paper Wilhelmy plate setup. Following compression, the coated area of the trough was reduced from approximately 144 cm^2 to around 104 cm^2, and the excess water was carefully removed from the trough using a vacuum aspirator which was placed to the left of the leftmost Teflon barrier so that the layer of graphene was lowered onto the surface of the substrate(s).

The coated materials were allowed to dry under nitrogen overnight before being transferred into an oven to be further dried overnight at a temperature of 75 °C. The dried membranes could then be removed from the glass substrate. Images of the deposition ink, as well as an example of a coated membrane, are shown in Figure S3. Video S1 shows the in situ coating process on the membrane surface.

2.4. Membrane Characterization. *2.4.1. Water Uptake and Swelling Ratio.* The membrane samples (7.6 cm by 7.6 cm as required for the battery) were soaked in DI water at room temperature for 24 h. Residual water on the membrane surface was removed using adsorbent paper, and the mass and dimensions (length, width, and thickness) of the hydrated membrane samples were measured. The membrane samples were then dried in a vacuum oven at 100 °C for 24 h, and the mass and dimensions of the dry membrane were determined. The water uptake and swelling ratio of the membranes were determined from the percentage difference in mass and volume, respectively, of the hydrated and dry membranes.[10,12,43] The measurements were repeated for three membrane samples in each case.

2.4.2. Ion Exchange Capacity. The ion exchange capacity (IEC) of the membrane was obtained by titration.[10,12,43] Dry membrane samples were immersed in 50 mL of 3.0 M NaCl solution for 24 h at room temperature to exchange protons with sodium ions. The solution was then titrated with 0.1 M NaOH to determine the proton concentration. The IEC was calculated by dividing the amount of NaOH required to neutralize the solution by the dry mass of the membrane. The IEC of three samples was determined in each case.

2.4.3. Area Specific Resistance and Proton Conductivity. To evaluate the area specific resistance of the membrane (r), the membrane samples were soaked in a solution of 1.6 M $VOSO_4$ and 3.0 M H_2SO_4 for 24 h. The membrane was placed in a 5 cm^2 RFB cell filled with 3.0 M H_2SO_4 electrolyte. The cell resistance was determined in the presence (r_1) and absence (r_2) of the membrane by electrochemical impedance spectroscopy (EIS). The effective membrane area (S) of the cell was 5 cm^2. The area specific resistance of the membrane (Ω cm^2) was calculated using eq 1:[44]

$$r = (r_1 - r_2) \times S \quad (1)$$

The proton conductivity of the membrane samples was determined by EIS in the RFB setup. Impedance was measured in the range of 1 Hz to 100 kHz. The membrane samples were soaked in DI water for 24 h

https://doi.org/10.1021/acsaem.3c00428
ACS Appl. Energy Mater. 2023, 6, 6505–6517

at room temperature before the experiment to ensure the samples were fully hydrated. The proton conductivity (σ) was calculated according to eq 2:[12,34]

$$\sigma = \frac{L}{R \times A} \tag{2}$$

where L, R, and A are the thickness, resistance, and cross-sectional area of the membrane, respectively.

2.4.4. Vanadium Permeability. Although all vanadium species present in the VRFB (V^{2+}, V^{3+}, VO^{2+}, and VO_2^+) may pass through the membrane, most studies of membrane crossover have only measured the membrane permeability for VO^{2+} ions.[12,34,35,45−47] We follow a similar approach since the effect of the modification of the membrane on the permeability of other vanadium species is expected to be similar to that for VO^{2+}. The VO^{2+} permeability through the membranes was evaluated using the cell used for VRFB charge−discharge testing (as described below). Membrane samples (effective area of 5 cm^2) were sandwiched in the cell between the carbon paper electrodes in the cell. One tank was filled with 50 mL of 1.6 M $VOSO_4$ in 3 M H_2SO_4 solution (the source reservoir), and the other was filled with 50 mL of 1.6 M $MgSO_4$ in 3 M H_2SO_4 solution (the receiving reservoir) to balance ionic strength and reduce osmotic pressure effect. These solutions were circulated through the cell one each side of the membrane using a dual-head peristaltic pump. Samples on the $MgSO_4$ side were periodically withdrawn at timed intervals and the vanadium ion concentration was determined using inductively coupled plasma optical emission spectroscopy (ICP-OES, Varian 725). The VO^{2+} permeability (P) of the membrane was calculated from the rate increase in concentration in the $MgSO_4$ solution (eq 3)

$$P = \frac{V_B\, L}{S(C_A - C_B(t))} \frac{dC_B(t)}{dt} \tag{3}$$

where V_B is the volume of the $MgSO_4$ solution, C_A is the VO^{2+} concentration in the source reservoir, t is the duration of the experiment, and $C_B(t)$ is the measured VO^{2+} concentration of the receiving reservoir at time t.[10]

2.4.6. Materials Characterization. Scanning electron microscopy (SEM, Quanta FEG-250, Thermo Fisher Scientific) studies of the membrane before and after coating were used to evaluate the morphology and composition of the top surface and cross section of the membrane. Atomic force microscopy (AFM, Nanoscope Multi-Mode AFM, Veeco, Digital Instruments MMAFM-2) of the EEG coating was performed to evaluate the coverage and morphology of the coated surface. AFM was performed after EEG coating using the method described in Section 2.3 on substrates including 1 cm × 1 cm squares of freshly cleaved mica, p-doped silicon cleaned with ethanol, and samples of the swollen Nafion 117. The silicon and mica samples were dried overnight under nitrogen at room temperature, and the Nafion samples were dried overnight in an oven at 75 °C. Samples were imaged using AFM under ambient temperature and humidity. The silicon and mica samples were imaged using contact mode with a silicon nitride tip (Bruker, nonconducting silicon nitride, cantilever 600 nm), and a scan rate of 1 Hz was used with 512 samples/line. The Nafion samples were imaged using tapping mode to minimize potential damage from lateral forces on the softer polymeric substrates, using an antimony doped Si tip (Bruker, 0.01−0.025 Ω-cm, 127 μm length, 35 μm width, k: 42 N/m). These images were also taken at a scan rate of 1 Hz and 512 samples/line. A constant drive frequency of 359.13 kHz was used.

High-resolution transmission electron microscopy (TEM) images of the EEG were collected using an FEI Tecnai G220 equipped with an X-Max energy-dispersive X-ray spectroscopy (EDX) detector with an acceleration voltage of 200 keV. In addition, Raman spectroscopy (α 300R WITec GmbH, Germany) was conducted on samples of the EEG-coated membrane and bare membrane to confirm the presence of graphene coated on the membrane surface.

2.5. VRFB Charge−Discharge. To study the VRFB charge−discharge, a single flow cell (5 cm^2 effective area, supplied by Fuel Cell Technology, Inc.) with a serpentine flow field was used. Graphite plate current feeders with bare, thermally treated (1 h at 500 °C in air) carbon paper (Sigracet 39AA) electrodes, and bare or EEG-coated Nafion membranes were used in the cell. The membrane was soaked in DI water for 24 h before use.[2,48,49] Figure 2 shows a schematic of the VRFB flow cell testing system used in this study. In all experiments, the negative and positive electrolyte tanks each contained 20 mL of 1.6 M vanadium electrolyte in 3 M H_2SO_4. The electrolytes were prepared using vanadium oxysulfate ($VOSO_4$), and an initial charging procedure described in previous studies was followed.[2,8] The electrolyte solutions were circulated through the cell at a flow rate of 20 ml min^{-1} using a dual-head peristaltic pump (Masterflex, Cole Parmer). Humidified nitrogen was continuously bubbled through the electrolyte solution 30 min before and during the charge−discharge experiment to remove dissolved oxygen.

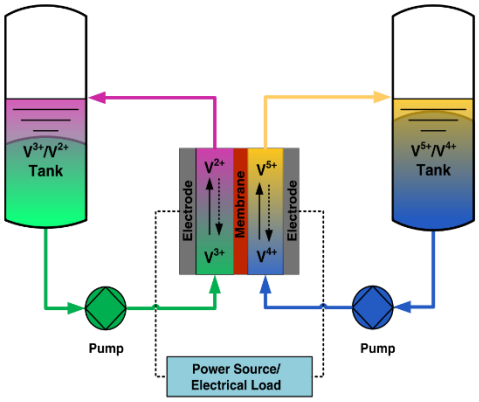

Figure 2. Schematic design of the VRFB charge−discharge cell.

Charge−discharge experiments were performed at constant current densities ranging from 10 to 100 mA cm^{-2}, using cutoff voltages of 1.65 V for charging, and 0.8 V for discharging. A potentiostat (BioLogic VSP/VMP3B-20) operating in galvanostatic mode was used for the charge−discharge experiments. The VRFB efficiencies including voltage (VE), coulombic (CE), and energy efficiency (EE) were determined based on eqs 4−6:[2,50]

$$CE = \frac{Q_d}{Q_c} \times 100\% \tag{4}$$

$$VE = \frac{V_{d,avg}}{V_{c,avg}} \times 100\% \tag{5}$$

$$EE = CE \times VE \tag{6}$$

where Q_c and Q_d are the charge and discharge capacities (in mAh), respectively, and $V_{c,avg}$ and $V_{d,avg}$ are the average cell voltage during charge and discharge, respectively.

3. RESULTS AND DISCUSSION

3.1. Graphene Characterization. High-resolution TEM images of EEG are shown in Figure 3. The EEG sheets had a relatively smooth surface with wrinkles that were more than a few hundred nanometers wide. Raman spectroscopy was performed to study the structural characteristics of graphene and graphite materials. The Raman D band (1350 cm^{-1}) is due to the breathing mode vibrations of the sp^2 carbon atoms and is activated by the presence of defects in the structure, such as

https://doi.org/10.1021/acsaem.3c00428
ACS Appl. Energy Mater. 2023, 6, 6505−6517

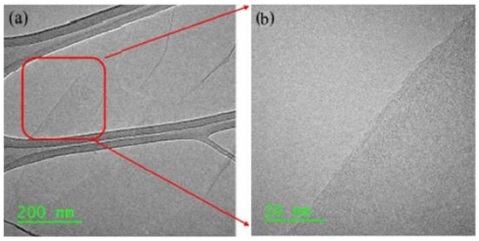

Figure 3. TEM images of EEG flakes at a range of magnification: (a) 200 nm, (b) 20 nm.

functional groups, edge sites, and structural disorder.[8,51] The Raman spectra obtained for EEG samples deposited on Si/SiO_2 wafers (Figure S4) show the typical spectra for exfoliated graphene, including the D, G, and 2D bands of the graphitic carbon structure. The observed spectrum is consistent with a reduced graphene oxide material and is similar to the Raman spectra obtained in previous studies of EEG prepared using similar methods.[40,41] The low-intensity ratio of the D and G peaks suggests that the EEG has a relatively low defect density.

3.2. Membrane Properties. Figures 4 and S5 show AFM and SEM images of the bare Nafion 117 and EEG-coated Nafion 117 membrane. From the SEM images (Figure S5a and d), the change in the morphology of the top surface of the Nafion due to the graphene coating is clearly evident. The SEM and AFM images confirm that the graphene nanoflakes (GNFs) are well distributed over the Nafion surface. It is difficult to determine the thickness of the EEG coating from the AFM data; however, there appears to be little overlapping of the GNFs, as expected for this LB coating method.[38] The thickness of the coating is thus expected to be the same as that of the EEG particles, comprising single to few-layer graphene, with a thickness of order 1−5 nm.[39]

The AFM surface micrographs show a clear difference between bare Nafion 117 (Figure 4a) and EEG-coated Nafion 117 (Figure 4b). Additionally, the graphene flakes appear wrinkled on the EEG-coated membrane compared to a coating of the same graphene dispersion on a flat mica substrate (Figure 4c). The estimated surface area of the GNFs on the Nafion membrane in Figure 4b is 38.18 μm^2 for the 2D field of view of 36 μm^2 as shown in the micrograph. On the mica, the surface area of GNFs for the same field of view is 36.13 μm^2. The Nafion membranes were coated when they were fully swollen with water, and they were dried prior to AFM imaging.

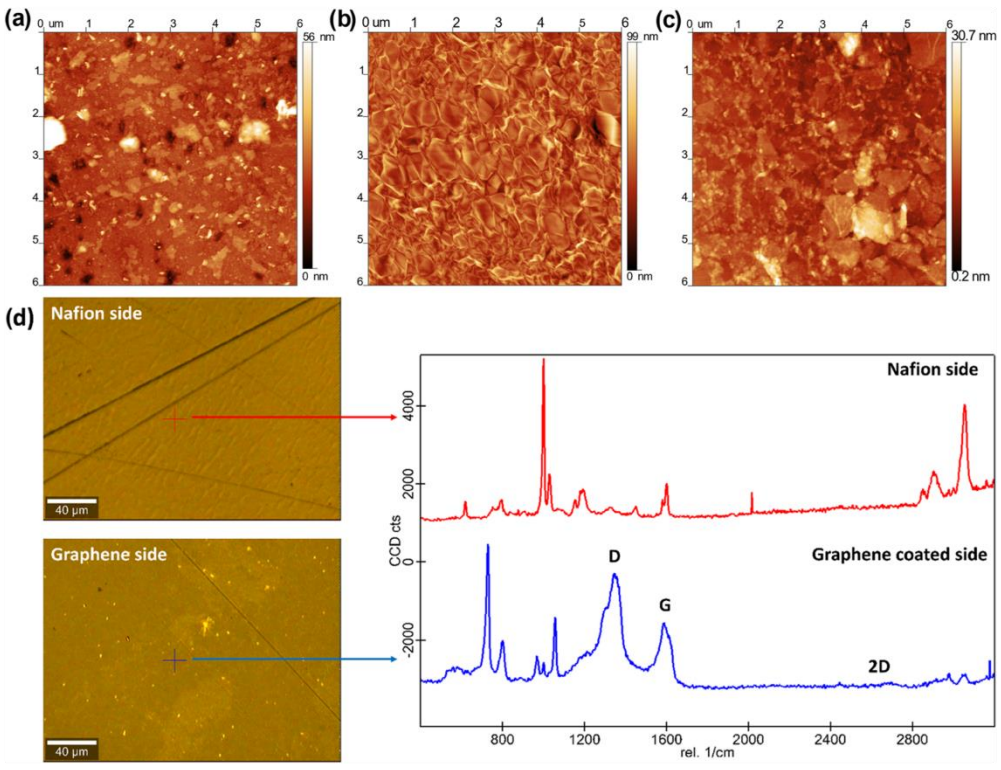

Figure 4. AFM images of (a) top surface of uncoated Nafion 117, (b) top surface of EEG-coated Nafion 117, and (c) top surface of mica coated with EEG. (d) Raman spectra from the bare Nafion 117 and EEG-coated Nafion 117 membrane.

https://doi.org/10.1021/acsaem.3c00428
ACS Appl. Energy Mater. 2023, 6, 6505−6517

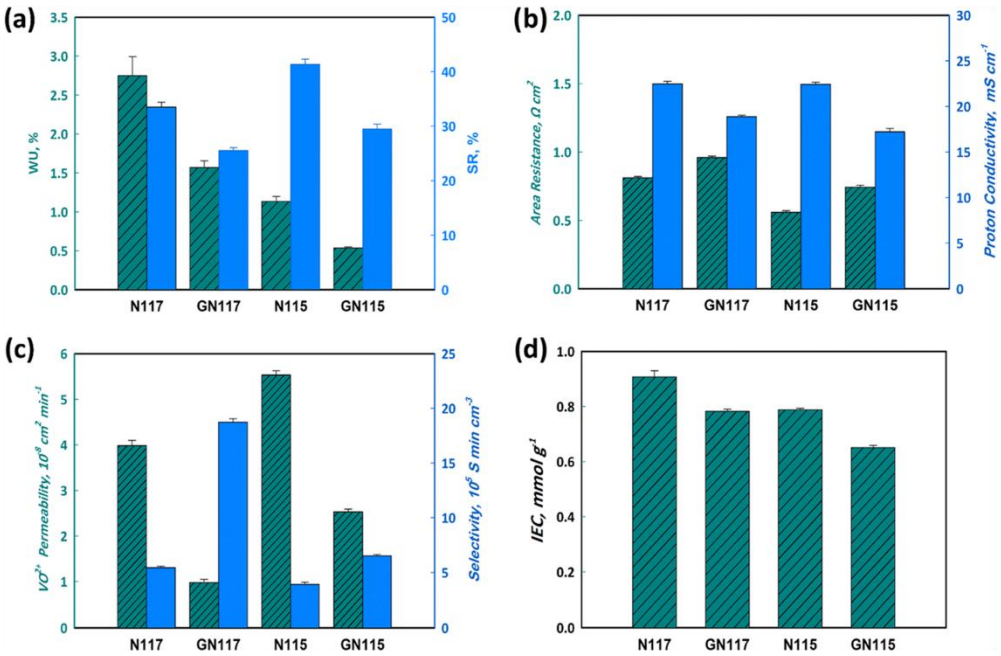

Figure 5. Comparison of the properties of Nafion and EEG-coated Nafion membranes: (a) water uptake and swelling ratio; (b) area resistance and proton conductivity; (c) VO^{2+} permeability and selectivity; and (d) IEC. N117 and N115 represent bare Nafion 117 and Nafion 115, respectively. GN117 and GN115 are the EEG-coated Nafion 117 and EEG-coated Nafion 115, respectively.

The GNFs wrinkle as the membrane shrinks rather than detaching from the membrane or sliding. The wrinkling is evidence that the strength of the interaction between the Nafion 117 and GNFs is enough to overcome the stiffness of the flakes.

The AFM images are consistent with SEM results for EEG-coated membrane in Figure S5d and f. To confirm the presence of graphene on the membrane surface, Raman spectroscopy was used. Figure 4d shows Raman spectra captured on the EEG-coated side and the uncoated side of the Nafion 117 membrane. Well-defined peaks were observed at Raman shifts of 1350 cm^{-1} (D-band) and 1580 cm^{-1} (G-band), as well as a small peak at 2700 cm^{-1} (2D band) confirming the presence of graphene on the membrane surface. The Raman peak observed at around 700 cm^{-1} is due to the CF_2 bond stretching in the Nafion 117 membrane.[52]

The physicochemical properties of the bare and EEG-coated Nafion membranes including the water uptake, swelling ratio, IEC, area specific resistance, proton conductivity, and permeability were determined. The swelling ratio and water uptake (Figure 5a) were lower for the EEG-coated membrane due to the steric confinement of the graphene, which limits the expansion of Nafion clusters.[34] The area specific resistance (Figure 5b) of the EEG-coated membranes was higher than bare Nafion membranes, consistent with the lower proton conductivity observed. Although protons are known to be able to pass through single-layer graphene with low resistance,[53,54] two-layer graphene will have a blocking effect on the proton transfer. Previous studies have shown that graphene oxide can impact the water uptake and hence the conductivity of the Nafion.[10] With lower water uptake, the membrane channel dimensions for the proton migration are narrower.[11] Area specific resistance is an important parameter that affects the voltage efficiency of VRFBs.[12] Although the area specific resistance is increased due to the graphene coating, the effect is relatively small and a graphene coating on a thinner membrane, Nafion 115, can deliver a similar resistance to that of uncoated Nafion 117 (Figure 5b). Optical images of the membranes before and after immersion in the acid solution for 24 h are shown in Figure S6. These images confirm that the EEG coated on the membrane surface is present after immersion in the 3 M sulfuric acid solution.

The VO^{2+} permeability and ion selectivity of EEG-coated and bare Nafion membranes are compared in Figure 5c. The selectivity is the ratio of proton conductivity to VO^{2+} permeability, with a higher selectivity a qualitative indicator of a better membrane for VRFB application.[31] The VO^{2+} permeability of the EEG-coated Nafion 117 and Nafion 115 membranes are 75 and 53%, respectively, lower than those for the bare Nafion. Studies of pristine single-layer graphene coated onto Nafion have demonstrated that graphene is only permeable to H^+ ions, and no other species will pass through the graphene structure.[55] As the graphene basal planes block the transport of VO^{2+}, these ions are forced to pass through the gaps between the graphene platelets. The lower water uptake and blocking effect of GNF slightly decrease the proton conductivity of the EEG-coated membranes. However, as the reduction in the VO^{2+} permeability is much greater than the

https://doi.org/10.1021/acsaem.3c00428
ACS Appl. Energy Mater. 2023, 6, 6505−6517

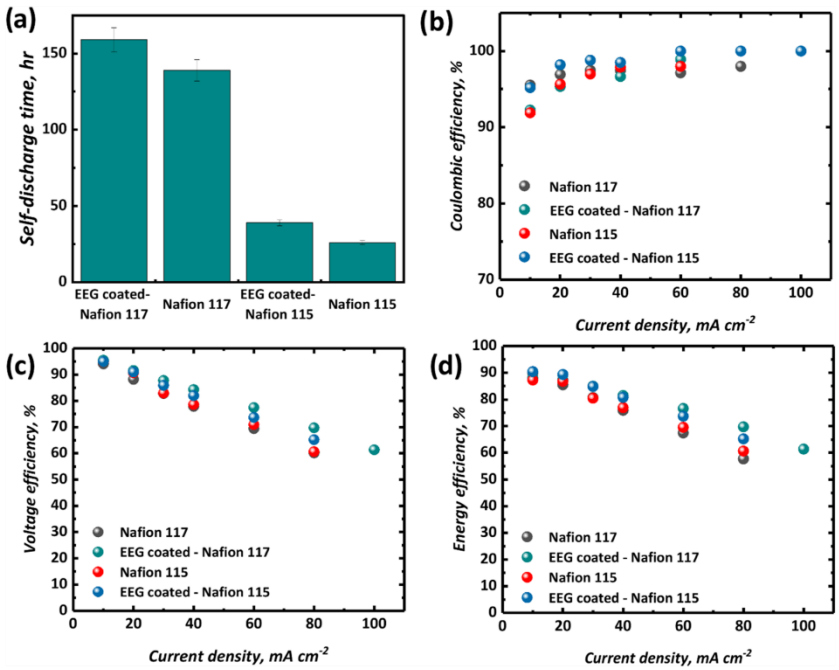

Figure 6. Comparison of VRFB performance using bare and EEG-coated Nafion 115 and 117 membranes: (a) self-discharge curves at 50% SOC and charge−discharge efficiencies at a range of current densities, including (b) CE, (c) VE, and (d) EE.

reduction in proton conductivity,[10,31] the EEG-coated membranes show higher selectivity than the bare Nafion membranes: 243% higher in the case of EEG-coated Nafion 117 and 65% higher in the case of EEG-coated Nafion 115. The higher selectivity indicates that the EEG coating improves the membrane properties for VRFB, and a higher battery performance may be expected.

The microstructure of the EEG has fewer channels for VO^{2+} transport than the bare Nafion membrane due to the graphene flakes covering the membrane surface. The two-dimensional graphene flakes serve as barriers to prevent VO^{2+} migrating through the membrane structure. To be transported through the Nafion matrix, VO^{2+} ions are constrained to the gaps between flakes, increasing the transport resistance. The VO^{2+} permeability also decreases with membrane thickness due to the longer transport pathway;[10−12,34,35,46] hence, the VO^{2+} permeability of Nafion 117 is lower than that of Nafion 115 (Figure 5c). Figure S7 shows the contact angle of the uncoated and EEG-coated Nafion 117, which were around 45 and 41°, respectively. The contact angle of the membranes confirms that they are both hydrophilic. The functional groups present on the EEG provide hydrophilicity, and there is no significant change in the contact angle of the Nafion after EEG coating.

The IEC of the bare Nafion was found to be around 0.8−0.9 mmol g^{-1} (Figure 5d) similar to the theoretical value[56] of 0.91 mmol g^{-1}. The IECs of the EEG-coated Nafion 117 and Nafion 115 membranes were found to be 13 and 16%, respectively, lower than the bare Nafion, due to the graphene layer which decreased the availability of ionic groups in the structure.[35] Ionic groups may be unavailable due to direct interactions with the graphene, or as a result of decreased water uptake because of steric confinement of the aligned graphene flakes, limiting the expansion of Nafion clusters.[34]

3.3. VRFB Performance. The membrane coating and orientation were optimized in the battery by comparing a single layer of EEG on one side, a single layer of EEG on both sides, and a double layer of EEG on one side. The optimization of the number of layers and coating side was achieved by comparing the battery performance, and the highest improvement was obtained in the case of a single layer of EEG coated on the surface of the membrane facing the positive electrode (Figure S8). This arrangement was used for the detailed investigation of the impact of the graphene coating on VRFB performance.

To evaluate the effect of the EEG coating on the VRFB performance, self-discharge, charge−discharge, and polarization experiments were conducted using the flow cell. In self-discharge experiments, the battery was held at open circuit while electrolyte at 50% state of charge (SOC) was circulated through the cell, and the cell voltage was monitored. Decrease in the open-circuit voltage (OCV) indicates loss in the SOC due to the crossover of charged vanadium ions. In each case, the OCV gradually decreased and then sharply dropped to 0.8 V (indicating a low SOC) as a result of vanadium crossover.[12] The self-discharge rate of Nafion 115 was observed to be higher than Nafion 117, indicated by the more rapid drop in the OCV (see Figures 6a and S9), consistent with the lower thickness and higher VO^{2+} permeability (Figure 5c). The self-

https://doi.org/10.1021/acsaem.3c00428
ACS Appl. Energy Mater. 2023, 6, 6505−6517

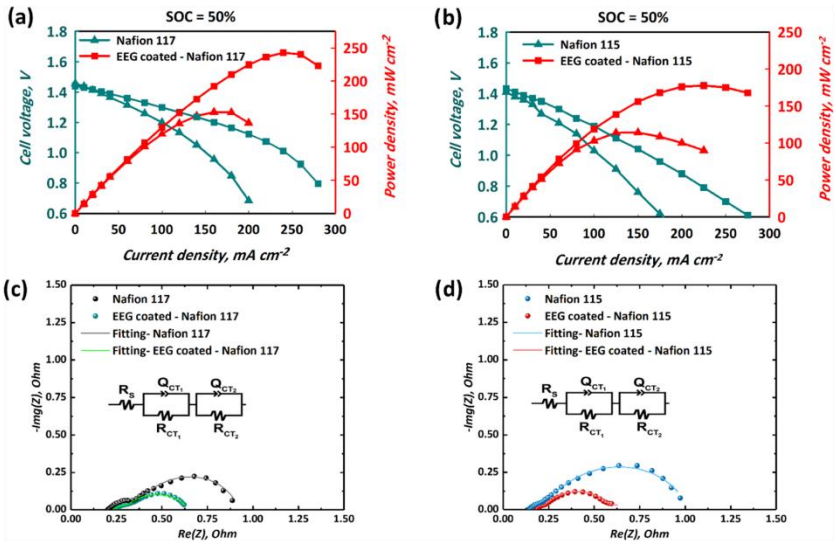

Figure 7. Polarization curves (a, b) and the EIS at open circuit (c, d) for VRFB using uncoated and EEG-coated Nafion membranes. Data is shown for Nafion 117 (a, c) and Nafion 115 (b, d).

discharge time (taken when the OCV reached 0.8 V) was 139, 159, 26, and 39 h for Nafion 117, EEG-coated Nafion 117, Nafion 115, and EEG-coated Nafion 115, respectively. Based on these results, the presence of the graphene has increased the self-discharge time, although the effect is relatively small. The self-discharge times for the bare Nafion membranes are consistent with values from the literature,[12,57] although there is significant variation in the values reported.

Figures 6b,c and 7d show the efficiencies (CE, VE, and EE) of the battery during charge−discharge cycling of the VRFB at different current densities with EEG-coated and uncoated Nafion 117 and 115. The battery performance results for the bare membranes are comparable with previous studies using the same electrode materials.[58,59] The CE (Figure 6b) increased as the current density increased from 10 to 100 mA cm^{-2}. With a higher current density, the charge−discharge duration decreased; this leads to a decrease in the amount of crossover of vanadium species, and hence a higher CE.[11] This trend confirms that vanadium species crossover is the main reason for CE losses.[2] In addition, the use of a thinner membrane (Nafion 115) led to a lower CE than the thicker Nafion 117, confirming the vanadium permeability and self-discharge results.[12] A higher CE was observed in the case of EEG-coated membranes since the graphene reduces the vanadium permeability without increasing the membrane thickness.

As the current density increases, the VE of the VRFB was observed to decrease (Figure 6c) due to increasing overpotential (including kinetic, Ohmic, and mass transport overpotential).[2,12] Due to the lower area specific resistance of the thinner Nafion 115 membrane, around 2% higher VE was observed for this membrane than for Nafion 117.[12] Although the area specific resistance of the EEG-coated membranes was higher than their bare Nafion counterparts (Figure 5b), the presence of the graphene coating led to a 10 and 5% higher VE for EEG coating on Nafion 117 and Nafion 115, respectively (Figure 6c), indicating that the total overpotential was reduced. The EE is the product of the CE and VE and was significantly higher for the EEG-coated membranes than the bare membrane at all current densities (Figure 6d). For example, the VRFB EE increased from 57 to 70% due to the EEG coating on Nafion 117 at a current density of 80 mA cm^{-2}.

Figure S10 shows VRFB charge−discharge curves for cells using EEG-coated and bare Nafion membranes at current densities from 10 to 80 mA cm^{-2}. The charge passed (capacity) for both charging and discharging reduced with increasing current density, as the higher overpotential led to the cutoff potentials being reached at lower (during charging) and higher (during discharge) SOC, respectively. In all cases, the cell voltage was higher during charge and lower during discharge when using the EEG-coated membranes (relative to the uncoated Nafion), leading to the higher VE observed in Figure 6c. The difference between the cell voltage for EEG-coated and uncoated membranes increased with current density, consistent with the expected behavior of the kinetic, Ohmic, and mass transport overpotentials. In all cases, the discharge capacities of EEG-coated membranes were higher than those for the bare Nafion at all current densities. SEM and AFM images of the top surface of the EEG-coated Nafion 117 before and after cycling (Figure S11) confirm the stability of the graphene layer on the membrane surface after cycling.

The VRFB charge−discharge curves and the VEs obtained indicate that the EEG coating leads to a reduction in the total overpotential, which is not expected based on the higher area specific resistance of the membranes. There are a few possible explanations for the observed improvement in cell voltages:

I. The graphene is electrochemically active, and in contact with the carbon paper electrode, enhancing the electrode

https://doi.org/10.1021/acsaem.3c00428
ACS Appl. Energy Mater. 2023, 6, 6505−6517

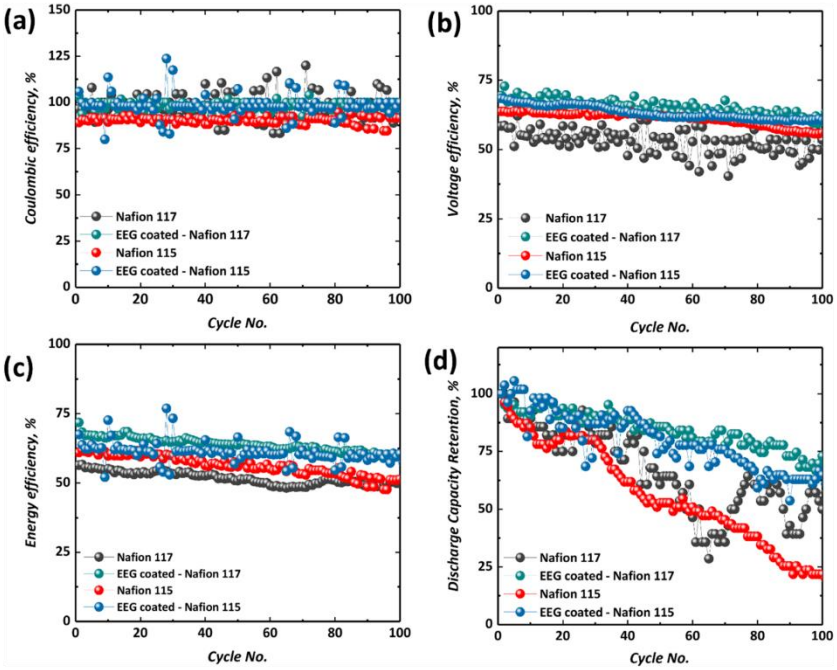

Figure 8. VRFB cycling stability, including: (a) CE, (b) VE, (c) EE, and (d) discharge capacity retention, during 100 cycles of VRFB charge–discharge at a current density of 80 mA cm^{-2}, using EEG-coated and uncoated Nafion membranes.

area and reducing kinetic and mass transfer overpotentials.

II. The presence of relatively large, low-mobility VO^{2+} ions in the ion conduction channels may reduce the proton conductivity of the membrane. It has been found that vanadium ions adsorb on Nafion reducing its ion exchange capacity by up to 30%.[60] The same study found that a VO^{2+} exchanged Nafion membrane had a conductivity around 8 times lower than pristine Nafion at 100% relative humidity. The addition of a layer of EEG on the Nafion surface, located on the positive side of the VRFB, can be expected to reduce the VO^{2+} content in the ion channels. Although the area specific resistance of the membrane was measured in a vanadium electrolyte solution, this was under open-circuit conditions when the vanadium ions equilibrate with the Nafion. Under operating conditions in the battery, the vanadium content of the membrane is likely to be reduced due to the current flow.

III. VO^{2+} ions transported through the membrane to the negative side of the cell may react with V^{2+}, reducing its concentration, or depolarize the V^{3+}/V^{2+} reaction. Thus, a lower VO^{2+} permeability could decrease the kinetic overpotential. However, the magnitude of this effect is expected to be small, and further work is needed to determine whether this effect plays any role in performance enhancement.

Of these possible explanations, (I) seems the most likely candidate since exfoliated graphene is known to be active for vanadium redox reactions, and it is located close to the membrane where the overpotential driving force for reactions is expected to be highest. However, it is unclear why having the EEG coating on the positive side would have the greater impact on the performance since the negative reaction is normally considered to be more sluggish. Most likely there is a combination of enhanced electrochemical kinetics (I), along with improvement in the membrane conductivity (II).

The polarization curve and power density at 50% SOC for EEG-coated and bare Nafion 117 and 115 membranes are shown in Figure 7a,b, respectively. The maximum power density delivered by the VRFB increased by 67% (from 150 to 250 mW cm^{-2}) and 55% (from 114 to 177 mW cm^{-2}) due to the EEG coating on Nafion 117 and Nafion 115, respectively. The polarization curve and power density at 100% SOC for EEG-coated and bare membranes are shown in Figure S12. The polarization curves demonstrate that the EEG coating can significantly enhance the power density by reducing the voltage loss and enabling operation at higher current density.

In order to determine the mechanism of the increased power density and reduced overpotential, EIS was performed on the VRFB, as shown in Figure 7c,d. The EIS was conducted at open-circuit potential, in the frequency range of 100 kHz to 1 mHz. The Ohmic resistance (R_s) and charge transfer resistance (R_{CT}) were determined by fitting the data to the equivalent circuit shown in the Nyquist plot, and the values obtained are shown in Table S1. The use of an equivalent circuit model is

https://doi.org/10.1021/acsaem.3c00428
ACS Appl. Energy Mater. 2023, 6, 6505−6517

considered a useful method for characterizing the electrode processes. However, it does not have a physical basis and different equivalent circuits could be used to fit the same data. The Ohmic resistance of the cell (R_s) is indicated by the intercept of Nyquist plot with the horizontal axis at high frequency, and a charge transfer resistance (R_{CT}) is indicated by the diameter of the flattened semicircles.[61,62] As shown in Figure 7c,d, compared to the uncoated Nafion, the EEG coating led to slightly higher Ohmic resistance (a slightly higher high-frequency intercept), and a significantly lower charge transfer resistance, indicated by the reduced diameter of the flattened semicircles.

The Ohmic resistance R_s increased slightly due to the EEG coating from 0.2 to 0.23 Ω for Nafion 117, and from 0.14 to 0.17 Ω for Nafion 115, consistent with the increased area specific resistance measurements (Figure 5b). The shape of the Nyquist plot indicates two overlapping flattened semicircles associated with the positive and negative electrode reactions.[62,63] Previous studies have larger semicircle observed at a higher frequency can be attributed to charge transfer at the negative electrode. Interestingly, the EIS data suggests that the EEG coating on the positive side of the membrane led to a reduction in the charge transfer resistance for the negative redox reactions for both Nafion 117 and 115 (see Table S1). For the positive redox reaction, the charge transfer resistance is relatively small compared to the negative reaction, and the effect of the EEG coating is inconclusive. However, the reduction in the charge transfer resistance due to the EEG coating appears to be large for the negative reaction R_{CT-}: 54% for Nafion 117 and 58% for Nafion 115. Further work is needed using a reference electrode to determine whether the change in charge transfer resistance can be ascribed to the negative or positive electrode charge transfer.

Since the EEG was applied to a commercial Nafion membrane, the chemical and mechanical stability of the membrane during cycling was expected to be unaffected. However, the stability of the EEG coating was investigated, by evaluating whether the enhancement in VRFB performance observed was retained during long-duration cycling. In addition, vanadium crossover along with water transport through the membrane is known to lead to capacity decay during VRFB cycling, and these effects may be mitigated by the EEG coating. To examine the stability of the EEG-coated membranes, the VRFB was cycled at a constant current density of 80 mA cm^{-2} at room temperature (25 °C) using charge and discharge cutoff voltages of 1.65 and 0.8 V, respectively. Figure 8 shows a comparison of the VRFB performance with EEG-coated and uncoated Nafion membranes over 100 cycles of charge and discharge. In all cases, the CEs of the VRFB remained almost constant throughout the cycling (Figure 8a). Note that due to the use of cutoff voltages, occasionally adjacent cycles showed lower and higher CEs, in some cases >100%. As discussed above, the CE of Nafion 115 was less than Nafion 117, due to the thinner membrane enabling higher vanadium crossover. The CE of the EEG-coated membranes was close to 100% throughout the 100 cycles, due to the lower vanadium permeability of these membranes.

The VEs and EEs of the VRFB show a slight decrease during cycling in all cases (Figure 8b,c). This is consistent with previous studies and is due to decreasing electrochemical activity of the electrodes, most likely due to changes in the functional groups on the surface of the carbon paper.[8] The enhancement in the VE and EE of the VRFB due to the EEG coating remains present after the 100th cycle, demonstrating the stability of the membrane coating.

The VRFB capacity showed significant fluctuation during cycling. Similar fluctuations in charge−discharge capacity have been reported in the literature.[8,34,68] This fluctuation was likely caused by the charge−discharge protocol, using cutoff voltages for charge and discharge, so the electrolyte state of charge was not the same for all cycles. As a small volume of electrolyte was used in each electrolyte tank, the capacity was very sensitive to changes in the state of charge and electrolyte crossover.

As expected, the capacity fading rate decreased with the membrane thickness, with the discharge capacity falling more rapidly with a Nafion 115 membrane compared to Nafion 117 (Figures 8d and S13). The VRFB discharge capacity retention after 100 cycles with uncoated Nafion 117, and Nafion 115 membranes was 50 and 22% of the initial capacity, respectively, corresponding to a loss of discharge capacity at a rate of around 0.50 and 0.78% per cycle. The value for the capacity retention over cycling for the bare membranes is comparable with the literature.[64] For example, VRFB capacity retention of 48 and 35% after 100 cycles at 80 mA cm^{-2} has been reported with Nafion 117 and Nafion 115 membranes, respectively.[31,65] The capacity retention was significantly higher for the EEG-coated membranes, with discharge capacity retention of 73 and 65% of the initial capacity after 100 cycles (i.e., a discharge capacity loss of 0.27 and 0.35% per cycle) in the case of EEG-coated Nafion 117 and Nafion 115, respectively. These rates of capacity fade are lower than the recently reported benchmark of 0.442% per cycle, and at the low end of the range of capacity fade rates in the literature.[64] The results demonstrate that the presence of the EEG coating on the membrane enhances the stability of the battery operation and reduces the capacity fading due to vanadium crossover during cycling.

Previous studies have demonstrated the use of graphene oxide (GO)/Nafion composites to reduce crossover and increase CE.[10,11,34,35,37] The performance of VRFB reported for GO/Nafion composite membranes is compared with this work in Table 1. Note that previous studies used different cell designs, electrode, and membrane materials (recast Nafion or Nafion 112), and generally showed higher voltage efficiencies than those achieved in this study. However, the GO composite membranes used in these previous studies led to very little change or a decrease in the VE compared to the unmodified membrane, due to a reduction in the membrane conductivity. The EEG-coated−Nafion 117 reported here shows a significant improvement in battery performance, with a 10% VE and 13% EE enhancement at a current density of 80 mA cm^{-2}. The capacity retention achieved is comparable with other membrane materials. It can be concluded that GO composite membranes decrease voltage efficiency, which will lead to a decrease in power density. In contrast, the EEG-coated membranes used in this work enable an *increase* in the maximum power density of the battery of 67 and 55% for Nafion 117 and Nafion 115, respectively (Figure 7).

4. CONCLUSIONS

The membrane plays an important role in RFB technology as it separates the active species on each side of the battery, and the transport of active species through the membrane leads to instability and capacity decay. Nafion, widely used in VRFB, is known to be permeable to vanadium ions. While alternative membrane materials and Nafion composites have been able to reduce vanadium permeability, in most if not all cases the VE

https://doi.org/10.1021/acsaem.3c00428
ACS Appl. Energy Mater. 2023, 6, 6505−6517

Table 1. Comparison of the Capacity Retention and VRFB Efficiencies Reported Using Graphene Oxide/Nafion Composite Membranes and the EEG-Coated Nafion Used in This Study[a]

base membrane composite membrane	no. of cycles	capacity retention (%)	CE (%)	VE (%)	change in VE (%)	ref
Recast Nafion	200	62	91	88	no change	10
Recast Nafion/GO		76	96	88		
Recast Nafion	-	-	88	85	+1	11
Recast Nafion/GO			89	86		
Nafion 212	50	80	92.5	88	−2.5	34
Recast Nafion/GO		88	98	85.5		
Nafion 212	50	61	89	82	−4	37
PES/GO		65	97	78		
Nafion 212	60	80	90	91	−4	35
Nafion 212/CLGO	180	55	97	87		
Nafion 117	100	50	95	60	+10	this work
Nafion 117/EEG		73	100	70		
Nafion 115	100	25	100	60	+7	this work
Nafion 115/EEG		65	100	67		

[a]All data are for charge−discharge at a current density of 80 mA cm^{-2}.

and maximum power density are lower than with unmodified Nafion, due to the higher area specific resistance of these alternative membrane materials.[34,35,65] In this work, by using a single layer of exfoliated graphene, evenly covered over the surface of the Nafion, we are able to significantly reduce the vanadium permeability with only a very slight increase in area specific resistance. This membrane demonstrated significant enhancement in the VRFB charge−discharge efficiency and power density, as well as increased capacity retention, without requiring any modification to the battery design, electrode materials, or operating conditions. The maximum power density was increased by as much as 67% (at 50% SOC), while the rate of loss of discharge capacity was more than halved.

These improvements are very significant, enabling a reduction in the size of the VRFB stack for a given power output, and stabilizing and simplifying battery operation. By using this single-layer approach, the amount of graphene required is very small (ca. 3 mg EEG per m^2 of membrane), and the coating can be applied to any commercial membrane material, without requiring complex manufacturing processes such as blending and casting. It is also important to note that the EEG coating on the membrane appears to be very stable, with the enhancement in efficiency retained during 100 cycles of charge−discharge. The EEG appears to be strongly bound to the Nafion membrane, likely due to interactions between functional groups on the graphene and the sulfonate groups in the Nafion structure.

The increase in EE and power density of the VRFB with the EEG coating were unexpected, given the increase in the areal resistance of the membrane. EIS analysis demonstrates that the reduced crossover of VO^{2+} ions from the positive side of the battery leads to depolarization of the negative electrode so that by reducing the crossover the battery performance is enhanced. To our knowledge, this is the first time that this mechanism has been proposed. Previous studies of GO composite membranes did not observe an improvement in VE associated with improved kinetics, perhaps because any depolarization was outweighed by an increase in the membrane resistance. If this mechanism is confirmed, it suggests that membrane improvements can not only reduce capacity fading but also increase battery power density through reduced vanadium ion crossover. Further work is needed to investigate the mechanism of enhancement of power density, the effect of EEG coating on other materials such as anion exchange membranes, and to evaluate the performance of the EEG-coated membrane in a commercial VRFB.

■ ASSOCIATED CONTENT

Supporting Information

The Supporting Information is available free of charge at https://pubs.acs.org/doi/10.1021/acsaem.3c00428.

Experimental methodology—coating process; graphene characterization—Raman spectroscopy; membrane characterization—SEM & AFM; VRFB flow cell performance—optimization of coating layer; self-discharge test, charge−discharge voltage curves, and SEM and AFM images before and after cycling; polarization curve; charge−discharge capacity over the cycling; and EIS fitting parameters (PDF)

Compression of the graphene film during the coating process (MP4)

■ AUTHOR INFORMATION

Corresponding Author

Edward P. L. Roberts − *Department of Chemical and Petroleum Engineering, University of Calgary, Calgary, AB T2N 1N4, Canada;* orcid.org/0000-0003-2634-0647; Email: edward.roberts@ucalgary.ca

Authors

Maedeh Pahlevaninezhad − *Department of Chemical and Petroleum Engineering, University of Calgary, Calgary, AB T2N 1N4, Canada;* orcid.org/0000-0001-9200-5607

Elizabeth Esther Miller − *Department of Chemical Engineering, University of Waterloo, Waterloo, ON N2L 3G1, Canada*

Lixin Yang − *Department of Chemical and Petroleum Engineering, University of Calgary, Calgary, AB T2N 1N4, Canada*

Lauren Sarah Prophet − *Department of Chemical Engineering, University of Waterloo, Waterloo, ON N2L 3G1, Canada*

Ashutosh Singh − *Department of Chemical and Petroleum Engineering, University of Calgary, Calgary, AB T2N 1N4, Canada;* orcid.org/0000-0002-0464-6672

Thomas Storwick − *Department of Chemical Engineering, University of Waterloo, Waterloo, ON N2L 3G1, Canada*

Majid Pahlevani − *Department of Electrical and Computer Engineering, Queen's University, Kingston, Ontario K7L 3N6, Canada*

Michael A. Pope − *Department of Chemical Engineering, University of Waterloo, Waterloo, ON N2L 3G1, Canada*

Complete contact information is available at: https://pubs.acs.org/10.1021/acsaem.3c00428

Notes

The authors declare no competing financial interest.

https://doi.org/10.1021/acsaem.3c00428
ACS Appl. Energy Mater. 2023, 6, 6505−6517

■ ACKNOWLEDGMENTS

The authors are grateful for the funding received from Alberta Innovates (Project #202101720), and the Natural Sciences and Engineering Research Council of Canada (NSERC CREATE 495455−2017 and RGPIN-2018−03725).

■ REFERENCES

(1) Nalley, S.; Larose, A. International Energy Outlook 2021 (IEO2021) 2021., October 6. https://www.eia.gov/outlooks/ieo/pdf/IEO2021_ReleasePresentation.pdf.
(2) Pahlevaninezhad, M.; Pahlevani, M.; Roberts, E. P. L. Effects of Aluminum, Iron, and Manganese Sulfate Impurities on the Vanadium Redox Flow Battery. *J. Power Sources* **2022**, *529*, No. 231271.
(3) Pahlevaninezhad, M.; Leung, P.; Velasco, P. Q.; Pahlevani, M.; Walsh, F. C.; Roberts, E. P. L.; Ponce de León, C. A Nonaqueous Organic Redox Flow Battery Using Multi-Electron Quinone Molecules. *J. Power Sources* **2021**, *500*, No. 229942.
(4) Zhang, C.; Zhang, L.; Ding, Y.; Peng, S.; Guo, X.; Zhao, Y.; He, G.; Yu, G. Progress and Prospects of Next-Generation Redox Flow Batteries. *Energy Storage Mater.* **2018**, *15*, 324−350.
(5) Huang, Z.; Mu, A.; Wu, L.; Yang, B.; Qian, Y.; Wang, J. Comprehensive Analysis of Critical Issues in All-Vanadium Redox Flow Battery. *ACS Sustainable Chem. Eng.* **2022**, *10*, 7786−7810.
(6) MacHado, C. A.; Brown, G. O.; Yang, R.; Hopkins, T. E.; Pribyl, J. G.; Epps, T. H. Redox Flow Battery Membranes: Improving Battery Performance by Leveraging Structure-Property Relationships. *ACS Energy Lett.* **2021**, *6*, 158−176.
(7) Alotto, P.; Guarnieri, M.; Moro, F. Redox Flow Batteries for the Storage of Renewable Energy: A Review. *Renewable Sustainable Energy Rev.* **2014**, *29*, 325−335.
(8) Singh, A. K.; Pahlevaninezhad, M.; Yasri, N.; Roberts, E. Degradation of Carbon Electrodes in the All-Vanadium Redox Flow Battery. *ChemSusChem* **2021**, *14*, 2100−2111.
(9) Gubler, L. Membranes and Separators for Redox Flow Batteries. *Curr. Opin. Electrochem.* **2019**, *18*, 31−36.
(10) Yu, L.; Lin, F.; Xu, L.; Xi, J. A Recast Nafion/Graphene Oxide Composite Membrane for Advanced Vanadium Redox Flow Batteries. *RSC Adv.* **2016**, *6*, 3756−3763.
(11) Lee, K. J.; Chu, Y. H. Preparation of the Graphene Oxide (GO)/Nafion Composite Membrane for the Vanadium Redox Flow Battery (VRB) System. *Vacuum* **2014**, *107*, 269−276.
(12) Jiang, B.; Wu, L.; Yu, L.; Qiu, X.; Xi, J. A Comparative Study of Nafion Series Membranes for Vanadium Redox Flow Batteries. *J. Membr. Sci.* **2016**, *510*, 18−26.
(13) Lu, W.; Yuan, Z.; Zhao, Y.; Li, X.; Zhang, H.; Vankelecom, I. F. J. High-Performance Porous Uncharged Membranes for Vanadium Flow Battery Applications Created by Tuning Cohesive and Swelling Forces. *Energy Environ. Sci.* **2016**, *9*, 2319−2325.
(14) Doan, T. N. L.; Hoang, T. K. A.; Chen, P. Recent Development of Polymer Membranes as Separators for All-Vanadium Redox Flow Batteries. *RSC Adv.* **2015**, *5*, 72805−72815.
(15) Zhang, D.; Xu, Z.; Zhang, X.; Zhao, L.; Zhao, Y.; Wang, S.; Liu, W.; Che, X.; Yang, J.; Liu, J.; Yan, C. Oriented Proton-Conductive Nanochannels Boosting a Highly Conductive Proton-Exchange Membrane for a Vanadium Redox Flow Battery. *ACS Appl. Mater. Interfaces* **2021**, *13*, 4051−4061.
(16) Li, X.; Zhang, H.; Mai, Z.; Zhang, H.; Vankelecom, I. Ion Exchange Membranes for Vanadium Redox Flow Battery (VRB) Applications. *Energy Environ. Sci.* **2011**, *4*, 1147−1160.
(17) Huang, X.; Pu, Y.; Zhou, Y.; Zhang, Y.; Zhang, H. In-Situ and Ex-Situ Degradation of Sulfonated Polyimide Membrane for Vanadium Redox Flow Battery Application. *J. Membr. Sci.* **2017**, *526*, 281−292.
(18) Schwenzer, B.; Zhang, J.; Kim, S.; Li, L.; Liu, J.; Yang, Z. Membrane Development for Vanadium Redox Flow Batteries. *ChemSusChem* **2011**, *4*, 1388−1406.
(19) Liu, S.; Wang, L.; Ding, Y.; Liu, B.; Han, X.; Song, Y. Novel Sulfonated Poly (Ether Ether Keton)/Polyetherimide Acid-Base Blend Membranes for Vanadium Redox Flow Battery Applications. *Electrochim. Acta* **2014**, *130*, 90−96.
(20) Gao, N.; Zhang, F.; Zhang, S.; Liu, J. Novel Cardo Poly(Arylene Ether Sulfone)s with Pendant Sulfonated Aliphatic Side Chains for Proton Exchange Membranes. *J. Membr. Sci.* **2011**, *372*, 49−56.
(21) Zhang, Y.; Li, J.; Zhang, H.; Zhang, S.; Huang, X. Sulfonated Polyimide Membranes with Different Non-Sulfonated Diamines for Vanadium Redox Battery Applications. *Electrochim. Acta* **2014**, *150*, 114−122.
(22) Mai, Z.; Zhang, H.; Li, X.; Bi, C.; Dai, H. Sulfonated Poly(Tetramethydiphenyl Ether Ether Ketone) Membranes for Vanadium Redox Flow Battery Application. *J. Power Sources* **2011**, *196*, 482−487.
(23) Li, Z.; Dai, W.; Yu, L.; Liu, L.; Xi, J.; Qiu, X.; Chen, L. Properties Investigation of Sulfonated Poly(Ether Ether Ketone)/Polyacrylonitrile Acid-Base Blend Membrane for Vanadium Redox Flow Battery Application. *ACS Appl. Mater. Interfaces* **2014**, *6*, 18885−18893.
(24) Xi, J.; Wu, Z.; Qiu, X.; Chen, L. Nafion/SiO2 Hybrid Membrane for Vanadium Redox Flow Battery. *J. Power Sources* **2007**, *166*, 531−536.
(25) Teng, X.; Zhao, Y.; Xi, J.; Wu, Z.; Qiu, X.; Chen, L. Nafion/Organic Silica Modified TiO2 Composite Membrane for Vanadium Redox Flow Battery via in Situ Sol-Gel Reactions. *J. Membr. Sci.* **2009**, *341*, 149−154.
(26) Wang, N.; Peng, S.; Wang, H.; Li, Y.; Liu, S.; Liu, Y. SPPEK/WO 3 Hybrid Membrane Fabricated via Hydrothermal Method for Vanadium Redox Fl Ow Battery. *Electrochem. Commun.* **2012**, *17*, 30−33.
(27) Tian, B.; Yan, C. W.; Wang, F. H. Proton Conducting Composite Membrane from Daramic/Nafion for Vanadium Redox Flow Battery. *J. Membr. Sci.* **2004**, *234*, 51−54.
(28) Zeng, J.; Jiang, C.; Wang, Y.; Chen, J.; Zhu, S.; Zhao, B.; Wang, R. Studies on Polypyrrole Modified Nafion Membrane for Vanadium Redox Flow Battery. *Electrochem. Commun.* **2008**, *10*, 372−375.
(29) Teng, X.; Dai, J.; Su, J.; Zhu, Y.; Liu, H.; Song, Z. A High Performance Polytetrafluoroethene/Nafion Composite Membrane for Vanadium Redox Flow Battery Application. *J. Power Sources* **2013**, *240*, 131−139.
(30) Jiang, B.; Yu, L.; Wu, L.; Mu, D.; Liu, L.; Xi, J.; Qiu, X. Insights into the Impact of the Nafion Membrane Pretreatment Process on Vanadium Flow Battery Performance. *ACS Appl. Mater. Interfaces* **2016**, *8*, 12228−12238.
(31) Dai, W.; Shen, Y.; Li, Z.; Yu, L.; Xi, J.; Qiu, X. SPEEK/Graphene Oxide Nanocomposite Membranes with Superior Cyclability for Highly Efficient Vanadium Redox Flow Battery. *J. Mater. Chem. A* **2014**, *2*, 12423−12432.
(32) Park, S.; Kim, H. Preparation of a Sulfonated Poly(Ether Ether Ketone)-Based Composite Membrane with Phenyl Isocyanate Treated Sulfonated Graphene Oxide for a Vanadium Redox Flow Battery. *J. Electrochem. Soc.* **2016**, *163*, A2293−A2298.
(33) Kim, K. J.; Park, M. S.; Kim, Y. J.; Kim, J. H.; Dou, S. X.; Skyllas-Kazacos, M. A Technology Review of Electrodes and Reaction Mechanisms in Vanadium Redox Flow Batteries. *J. Mater. Chem. A* **2015**, *3*, 16913−16933.
(34) Su, L.; Zhang, D.; Peng, S.; Wu, X.; Luo, Y.; He, G. Orientated Graphene Oxide/Nafion Ultra-Thin Layer Coated Composite Membranes for Vanadium Redox Flow Battery. *Int. J. Hydrogen Energy* **2017**, *42*, 21806−21816.
(35) Zhang, D.; Wang, Q.; Peng, S.; Yan, X.; Wu, X.; He, G. An Interface-Strengthened Cross-Linked Graphene Oxide/Nafion212 Composite Membrane for Vanadium Flow Batteries. *J. Membr. Sci.* **2019**, *587*, No. 117189.
(36) Lai, Y.; Wan, L.; Wang, B. PVDF/Graphene Composite Nanoporous Membranes for Vanadium Flow Batteries. *Membranes* **2019**, *9*, 89.
(37) Park, S. C.; Lee, T. H.; Moon, G. H.; Kim, B. S.; Roh, J. M.; Cho, Y. H.; Kim, H. W.; Jang, J.; Park, H. B.; Kang, Y. S. Sub-5 Nm

Graphene Oxide Nanofilm with Exceptionally High H+/V Selectivity for Vanadium Redox Flow Battery. *ACS Appl. Energy Mater* **2019**, *2*, 4590−4596.
(38) Zhang, Y.; Xu, L.; Walker, W. R.; Tittle, C. M.; Backhouse, C. J.; Pope, M. A. Langmuir Films and Uniform, Large Area, Transparent Coatings of Chemically Exfoliated MoS2 Single Layers. *J. Mater. Chem. C* **2017**, *5*, 11275−11287.
(39) Roberts, E.; Singh, A. ELECTROCHEMICAL GRAPHENE EXFOLIATION WITH HYDROXIDE INTERCALATION. US2021/0253432A1, 2021. https://patents.google.com/patent/US20210253432A1/en.
(40) Cao, J.; He, P.; Mohammed, M. A.; Zhao, X.; Young, R. J.; Derby, B.; Kinloch, I. A.; Dryfe, R. A. W. Two-Step Electrochemical Intercalation and Oxidation of Graphite for the Mass Production of Graphene Oxide. *J. Am. Chem. Soc.* **2017**, *139*, 17446−17456.
(41) Momodu, D.; Madito, M. J.; Singh, A.; Sharif, F.; Karan, K.; Trifkovic, M.; Bryant, S.; Roberts, E. P. L. Mixed-Acid Intercalation for Synthesis of a High Conductivity Electrochemically Exfoliated Graphene. *Carbon* **2021**, *171*, 130−141.
(42) Ojrzynska, M.; Wroblewska, A.; Judek, J.; Malolepszy, A.; Duzynska, A.; Zdrojek, M. Study of Optical Properties of Graphene Flakes and Its Derivatives in Aqueous Solutions. *Opt. Express.* **2020**, *28*, 7274−7281.
(43) Hwang, G.; Ohya, H. Preparation of Cation Exchange Membrane as a Separator for the All-Vanadium Redox Flow Battery. *J. Membr. Sci.* **1996**, *120*, 55−67.
(44) Peng, S.; Yan, X.; Wu, X.; Zhang, D.; Luo, Y.; Su, L.; He, G. Thin Skinned Asymmetric Polybenzimidazole Membranes with Readily Tunable Morphologies for High-Performance Vanadium Flow Batteries. *RSC Adv.* **2017**, *7*, 1852−1862.
(45) Wang, T.; Moon, S. J.; Hwang, D. S.; Park, H.; Lee, J.; Kim, S.; Lee, Y. M.; Kim, S. Selective Ion Transport for a Vanadium Redox Flow Battery (VRFB) in Nano-Crack Regulated Proton Exchange Membranes. *J. Membr. Sci.* **2019**, *583*, 16−22.
(46) Dai, Q.; Liu, Z.; Huang, L.; Wang, C.; Zhao, Y.; Fu, Q.; Zheng, A.; Zhang, H.; Li, X. Thin-Film Composite Membrane Breaking the Trade-off between Conductivity and Selectivity for a Flow Battery. *Nat. Commun.* **2020**, *11*, No. 13.
(47) Wang, T.; Han, J.; Kim, K.; Münchinger, A.; Gao, Y.; Farchi, A.; Choe, Y. K.; Kreuer, K. D.; Bae, C.; Kim, S. Suppressing Vanadium Crossover Using Sulfonated Aromatic Ion Exchange Membranes for High Performance Flow Batteries. *Mater. Adv.* **2020**, *1*, 2206−2218.
(48) Thiam, B. G.; Vaudreuil, S. Review—Recent Membranes for Vanadium Redox Flow Batteries. *J. Electrochem. Soc.* **2021**, *168*, No. 070553.
(49) Reed, D.; Thomsen, E.; Wang, W.; Nie, Z.; Li, B.; Wei, X.; Koeppel, B.; Sprenkle, V. Performance of Nafion N115, Nafion NR-212, and Nafion NR-211 in a 1 KW Class All Vanadium Mixed Acid Redox Flow Battery. *J. Power Sources* **2015**, *285*, 425−430.
(50) Ahn, Y.; Kim, D. Ultra-Low Vanadium Ion Permeable Electrolyte Membrane for Vanadium Redox Flow Battery by Pore Filling of PTFE Substrate. *Energy Storage Mater.* **2020**, *31*, 105−114.
(51) Ferrari, A. C.; Meyer, J. C.; Scardaci, V.; Casiraghi, C.; Lazzeri, M.; Mauri, F.; Piscanec, S.; Jiang, D.; Novoselov, K. S.; Roth, S.; Geim, A. K. Raman Spectrum of Graphene and Graphene Layers. *Phys. Rev. Lett.* **2006**, *197*, No. 187401.
(52) El Boukari, M.; Bribes, J. -L.; Maillols, J. Application of Raman Spectroscopy to Industrial Membranes. Part 1—Polyacrylic Membranes. *J. Raman Spectrosc.* **1990**, *21*, 755−759.
(53) Chien, H. C.; Tsai, L. D.; Huang, C. P.; Kang, C. Y.; Lin, J. N.; Chang, F. C. Sulfonated Graphene Oxide/Nafion Composite Membranes for High-Performance Direct Methanol Fuel Cells. *Int. J. Hydrogen Energy* **2013**, *38*, 13792−13801.
(54) Parthiban, V.; Akula, S.; Peera, S. G.; Islam, N.; Sahu, A. K. Proton Conducting Nafion-Sulfonated Graphene Hybrid Membranes for Direct Methanol Fuel Cells with Reduced Methanol Crossover. *Energy Fuels* **2016**, *30*, 725−734.
(55) Hu, S.; Lozada-Hidalgo, M.; Wang, F. C.; Mishchenko, A.; Schedin, F.; Nair, R. R.; Hill, E. W.; Boukhvalov, D. W.; Katsnelson, M. I.; Dryfe, R. A. W.; Grigorieva, I. V.; Wu, H. A.; Geim, A. K. Proton Transport through One-Atom-Thick Crystals. *Nature* **2014**, *516*, 227−230.
(56) Mai, Z.; Zhang, H.; Li, X.; Xiao, S.; Zhang, H. Nafion/Polyvinylidene Fluoride Blend Membranes with Improved Ion Selectivity for Vanadium Redox Flow Battery Application. *J. Power Sources* **2011**, *196*, 5737−5741.
(57) Jiang, B.; Yu, L.; Wu, L.; Mu, D.; Liu, L.; Xi, J.; Qiu, X. Insights into the Impact of the Na Fi on Membrane Pretreatment Process on Vanadium Flow Battery Performance. *ACS Appl. Mater. Interfaces* **2016**, *8*, 12228−12238.
(58) Nibel, O.; Taylor, S. M.; Pătru, A.; Fabbri, E.; Gubler, L.; Schmidt, T. J. Performance of Different Carbon Electrode Materials: Insights into Stability and Degradation under Real Vanadium Redox Flow Battery Operating Conditions. *J. Electrochem. Soc.* **2017**, *164*, A1608−A1615.
(59) He, Z.; Su, A.; Gao, C.; Zhou, Z.; Pan, C.; Liu, S. Carbon Paper Modified by Hydrothermal Ammoniated Treatment for Vanadium Redox Battery. *Ionics* **2013**, *19*, 1021−1026.
(60) Cho, H. S.; Ohashi, M.; Van Zee, J. W. Absorption Behavior of Vanadium in Nafion. *J. Power Sources* **2014**, *267*, 547−552.
(61) Wu, L.; Wang, J.; Shen, Y.; Liu, L.; Xi, J. Electrochemical Evaluation Methods of Vanadium Flow Battery Electrodes. *Phys. Chem. Chem. Phys.* **2017**, *19*, 14708−14717.
(62) Mazur, P.; Mrlik, J.; Charvat, J.; Pocedic, J.; Vrana, J.; Dundalek, J.; Kosek, J. A Complex Four-Point Method for the Evaluation of Ohmic and Faradaic Losses within a Redox Flow Battery Single-Cell. *MethodsX* **2019**, *6*, 534−539.
(63) Yang, Q.; Xu, J.; Cao, B.; Li, X. A Simplified Fractional Order Impedance Model and Parameter Identification Method for Lithium-Ion Batteries. *PLoS One* **2017**, *12*, No. e0172424.
(64) Rodby, K. E.; Carney, T. J.; Ashraf Gandomi, Y.; Barton, J. L.; Darling, R. M.; Brushett, F. R. Assessing the Levelized Cost of Vanadium Redox Flow Batteries with Capacity Fade and Rebalancing. *J. Power Sources* **2020**, *460*, No. 227958.
(65) Kim, S.; Choi, J.; Choi, C.; Heo, J.; Kim, D. W.; Lee, J. Y.; Hong, Y. T.; Jung, H. T.; Kim, H. T. Pore-Size-Tuned Graphene Oxide Frameworks as Ion-Selective and Protective Layers on Hydrocarbon Membranes for Vanadium Redox-Flow Batteries. *Nano Lett.* **2018**, *18*, 3962−3968.
(66) Jiang, Y.; Cheng, G.; Li, Y.; He, Z.; Zhu, J.; Meng, W.; Dai, L.; Wang, L. Promoting Vanadium Redox Flow Battery Performance by Ultra-Uniform ZrO2@C from Metal-Organic Framework. *Chem. Eng. J.* **2021**, *415*, No. 129014.

https://doi.org/10.1021/acsaem.3c00428
ACS Appl. Energy Mater. 2023, 6, 6505−6517